2023

MEASUREMENTS OF THE BINDING ENERGIES OF IONS ON PLASTIC SURFACES IN LIQUID NITROGEN

Ashok Timsina
University of Kentucky, atimsina131@gmail.com
Author ORCID Identifier:
🆔 https://orcid.org/0009-0006-9922-6940
Digital Object Identifier: https://doi.org/10.13023/etd.2023.154

Right click to open a feedback form in a new tab to let us know how this document benefits you.

MEASUREMENTS OF THE BINDING ENERGIES OF IONS ON PLASTIC
SURFACES IN LIQUID NITROGEN

DISSERTATION

A dissertation submitted in partial
fulfillment of the requirements for
the degree of Doctor of Philosophy
in the College of Arts and Sciences
at the University of Kentucky

By
Ashok Timsina
Lexington, Kentucky

Director: Dr.Wolfgang Korsch, Professor of Physics
Lexington, Kentucky
2023

ABSTRACT OF DISSERTATION

MEASUREMENTS OF THE BINDING ENERGIES OF IONS ON PLASTIC
SURFACES IN LIQUID NITROGEN

To improve the present limit of the neutron electric dipole moment (nEDM) from 1.8×10^{-26} e. cm to $\sim 3 \times 10^{-28}$ e. cm, the nEDM@SNS experiment plans to increase neutron density by storing ultracold neutrons in superfluid helium-4. In this experiment, the central part of the apparatus consists of two deuterated tetraphenyl butadiene (dTPB) coated poly(methyl methacrylate) (PMMA) cells, which are sandwiched between grounded and high-voltage electrodes. To achieve such precision, the externally applied electric field has to be stable at the 1% level over a time period of about 1000 s. Several sources of ambient ionizing radiation generate charged particles in the cryogenic liquid. These ions and the associated electrons are adsorbed on the cell walls. Consequently, an opposing static electric field is generated, which will impact the stability of the electric field. At the University of Kentucky, we have devised a compact test setup to study the behavior of ions inside cryogenic liquids using a scaled-down version of the nEDM cell and the electrodes. In our setup, ion-electron pairs are generated by irradiating liquid nitrogen (helium) with a ^{137}Cs γ-source, and the electro-optic Kerr effect is utilized to understand the cell charging effects in the dummy measurement cell. We developed a new method to measure the binding energy of the ions or electrons bonded on insulating surfaces. Determining the binding energy can potentially reduce the data-taking time of the nEDM@SNS experiment if partial field reversal is sufficient. This dissertation presents studies of the binding energies of ions and/or electrons on dTPB-coated and uncoated PMMA surfaces in cryogenic liquid nitrogen.

KEYWORDS: nEDM@SNS, cryogenic liquid, binding energy, Kerr effect, neutron, cell charging

Ashok Timsina

May 5, 2023

MEASUREMENTS OF THE BINDING ENERGIES OF IONS ON PLASTIC
SURFACES IN LIQUID NITROGEN

By
Ashok Timsina

_____
Dr.Wolfgang Korsch
Director of Dissertation

_____
Dr. Christopher Crawford
Director of Graduate Studies

_____
May 5, 2023
Date

It is with great appreciation and gratitude that I dedicate this thesis to my parents, Damodar Timsina and Tara Devi Timsina. They have always been my closest allies and have consistently provided me with love, blessings, inspiration, encouragement, and support throughout my education.

Additionally, I want to dedicate this work to Dr. Binil Aryal, a Professor at Tribhuvan University, who has encouraged and motivated me to pursue a career in the field of physics. Their guidance and support have been invaluable to me and I am forever grateful.

ACKNOWLEDGMENTS

I would like to express my sincere appreciation and gratitude to my thesis supervisor, Dr. Wolfgang Korsch, for his unwavering support, invaluable guidance, and inspirational mentorship throughout my research journey. His constructive feedback and keen observations have been instrumental in shaping my work into its current form. I would also like to extend my thanks to the members of my thesis committee, Dr. Christopher Crawford, Dr. Susan Gardner, and Dr. Ellis L. Johnson, for their valuable insights and assistance throughout my Ph.D. experience. I am grateful to the external reviewer, Dr. Peter Hardy, for his time and valuable feedback. Lastly, I am thankful to the collaborators from nEDM@SNS for providing me with the opportunity to work on this challenging project.

I would also like to acknowledge the significant contributions of Jiachen He, Mark Broering, Suman Kandu, Girish Muralidhara, and Murchhana Roy, who supported me in various ways along the way. Additionally, I would like to thank Jim Morris and Steve Maynard for their assistance in machining various components and imparting their knowledge to me. Harvey Baber has been crucial in my understanding of vacuum systems, and Greg Porter provided valuable assistance with the planning and implementation of electronic components.

Lastly, I wish to express my deep appreciation for my wife, Sara Gautam Timsina, who has been an unwavering source of support and encouragement throughout this journey. I am also grateful to my children, Florisha and Subha Timsina, as well as my brother, Kamal Timsina, for their love and motivation.

TABLE OF CONTENTS

LIST OF TABLES

Chapter 1 Introduction

It is an established fact that the universe as we know it today is largely composed of matter, rather than having an equal balance of matter and antimatter. This raises questions about the fundamental nature of the universe and our current understanding of it. The matter-antimatter asymmetry, also known as the baryon asymmetry of the universe (BAU), is widely regarded as one of the most profound mysteries in contemporary particle physics. It is difficult to account for the baryon asymmetry as an initial condition (i.e., at the beginning of time), because we think the very early universe undergoes inflation (an effect proposed as a solution to understand the extreme temperature uniformity of the cosmic microwave background radiation (CMB)). Many believe that if the baryon asymmetry originates from the initial conditions, then inflation would cause it to be diluted. In other words, the baryon asymmetry would be eliminated during the period of inflation. However, the Krnjaic paper [10] puts forward a basic model that illustrates how the baryon asymmetry can emerge from the initial state of a universe that experiences inflation. An alternative is to introduce new particle physics to create the baryon asymmetry dynamically as the universe cools. The conditions to realize that are called the Sakharov conditions, and one of its ingredients, CP violation, may have contributions from physics beyond the Standard Model. This possibility is probed through increasingly precise experimental investigations of the permanent electric dipole moment of the neutron, a prospect that motivates the work of this thesis.

Theoretical predictions of the Big Bang [[11], [12]] and observational evidence of the cosmic expansion [13] and CMB [14, 15] have established the presence of antimatter during the early universe. As the universe cooled down, the mutual annihilation of particles and anti-particles resulted in a universe composed mainly of radiation, with a slight excess of matter over antimatter, known as the BAU. This observation implies the existence of a physical process beyond the established principles of physics that could have caused this asymmetry. The BAU is given by the ratio of the difference between the number densities of baryons minus anti-baryons to the number density of photons, given by Equation 1.1.

$$\eta = \frac{n_b - n_{\bar{b}}}{n_\gamma} \tag{1.1}$$

The value of η can be independently determined in two ways:

1) From the abundances of light elements (^{2}H, ^{3}He, ^{4}He, ^{7}Li) in the intergalactic medium. The value of η from astrophysical observations gives $(4.7 - 6.5) \times 10^{-10}$ [[16],[17]].

2) From the power spectrum of temperature fluctuations in the cosmic background radiation. Based on recent measurements of the temperature anisotropy of the cosmic Microwave Background (CMB) radiation by the WMAP probe [18] and the analysis of large scale structure [17], a dependable estimation of the present baryon-to-photon ratio has been obtained to $\eta = (6.1 \pm 0.2) \times 10^{-10}$.

The two perspectives agree on the same value of η which is $\sim 10^{-10}$ [[18],[19]]. The possibility that the asymmetry may have developed dynamically by baryogenesis from the initial balanced matter-antimatter symmetry is made possible by the discovery of minor breaches of P and CP invariance.

C and CP symmetry violation is directly related to discrete symmetries and their violation, which describe the conditions necessary for baryogenesis, the generation of the baryon asymmetry in the universe.

The Sakharov conditions are a set of three requirements put forward by Andrei Sakharov in the 1960s that aim to explain the universe's preponderance of matter over antimatter [20]. These conditions are necessary for baryogenesis, the process of generating a surplus of baryons such as protons and neutrons, over antibaryons in the early universe. Research on the Sakharov conditions is ongoing in the fields of particle physics and cosmology, as scientists continue to seek a better understanding of how they may have been satisfied in the early universe.

1) Baryon number (B) violation: is a required and necessary condition to produce more baryons over antibaryons because, without B violation, it is impossible for any system to evolve from a state with $B = 0$ to a state $B \neq 0$.

2) Charge (C) and Charge-Parity (CP) violation: is also a required condition because it allows for a difference in the behavior of matter and antimatter, which can lead to a net production of baryons. Specifically, the violation of CP symmetry means that the weak force can preferentially produce baryons over antibaryons, leading to a net baryon excess.

3) Deviation from thermal equilibrium: is a time-translational invariant state in which the expectation values of all observables are constant; therefore, to evolve from $B = 0$ to $B \neq 0$, deviation from thermal equilibrium is required.

The third assumption of the Sakharov conditions requires a departure from thermal equilibrium in order to create a situation where the baryon number violation and CP violation can generate a net baryon asymmetry. In the case of electroweak baryogenesis, this departure from thermal equilibrium is achieved through the process of a first-order electroweak phase transition [[21], [22]].

During the early universe, the electroweak force was unified with the electromagnetic force, and the Higgs field was in a high-temperature, symmetric phase where the particles were massless. As the universe cooled, the Higgs field underwent a phase transition, becoming a low-temperature, broken phase where the particles acquired mass.

The mass of the Higgs boson (125.10 ± 0.14 GeV) [22] is too heavy for a first-order phase transition, which means that it cannot generate the correct baryon asymmetry in the universe [23]. It's worth noting that the investigations that demonstrate the necessity for extra sources of CP violation were performed within the context of models that involve a first-order electroweak phase transition, which is not present in the Standard Model. However, alternative scenarios that allow for such sources of CP violation still remain a possibility. Even if the transition could be of the first order, the amount of CP violation in the CKM matrix would not be sufficient to explain the baryon asymmetry.

The Standard Model has done a fantastic job of defining every known particle

and its interactions, but it falls short of explaining the asymmetry between matter and antimatter. As stated earlier, the observed value of η is $\sim 10^{-10}$, which is 10 to 12 orders of magnitude bigger than the amount anticipated by the Standard Model [24], assuming that the Cabibbo-Kobayashi-Masuyama (CKM) matrix is the only source of CP violation. This result implies that there must exist additional sources of CP violation that are currently unknown, in order to explain the observed baryon asymmetry of the universe. As a result, research into novel physics that goes beyond the Standard Model has started.

One of the key components in developing theories of contemporary particle physics to comprehend the universe's creation and evolution is CP violation. Thus, one probe to solve this puzzle may be the neutron electric dipole moment. Numerous studies are being conducted globally to increase the sensitivity of neutron electric dipole moment measurements (nEDM). Among them, nEDM@SNS is one of the experiments that will take place at the Spallation Neutron Source (SNS) at the Oak Ridge National Laboratory (ORNL). It is one of the most ambitious initiatives, with the goal of increasing the sensitivity by a factor of 100, i.e $\approx 10^{-28}$ e-cm compared to the current upper limit of $d_n = 1.8 \times 10^{-26}$ e-cm (90% C.L.) [25]. Figure 1.1 displays the evolution of the measured upper limit on the neutron EDM as a function of time [26], comparing it to different theoretical predictions on the right [27].
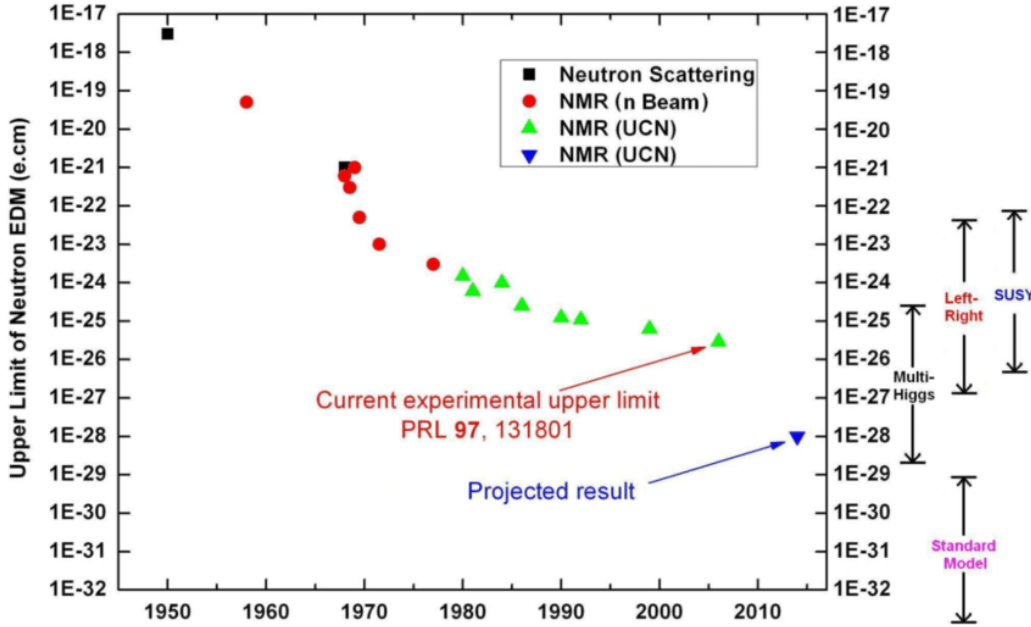
Figure 1.1: The upper limit of the nEDM experiment as a function of time. The legend highlights the experimental methods. To the right of the picture are predicted ranges for the nEDM values from various theoretical models [2].

The nEDM@SNS experiment (explained in Chapter 3), along with its experimental difficulties, will be the main motivation of this thesis. This experiment plans to use superfluid liquid helium (SFHe4) as a medium to produce ultracold neutrons and explore the neutron's electric dipole moment. Under strong electric fields, ul-

tracold neutrons (UCNs) will be collected and kept for several hundred seconds in deuterated-polymer-coated polymethyl methacrylate (PMMA) cells. To achieve the required sensitivity, the electric field inside measurement cells needs to be uniform and stable. A number of ambient ionizing radiation sources may generate free charges inside these cells throughout the data-taking periods of the experiment. The positive ions and the electrons are separated and drift to the dielectric side walls of the storage cells. This causes the generation of an opposite static electric field to the applied electric field, which reduces the stability of the electric field. During a typical 1000-second measuring cycle, the electric field's stability must be maintained at 1% [[28], [29]]. This constraint puts a limit on the amount of allowed ionization and charge collection on the cell walls. The behavior of ions in cryogenic liquids must therefore be thoroughly studied. The positive ions and electrons adsorbed on the measuring cell are extremely detrimental to our experiment. Therefore, it is necessary to eliminate these charges in order to create a stable and uniform electric field. To eliminate these charges from the surface, it is necessary to reverse the external electric field [7]; however, it is uncertain how much of a minimum electric field is necessary to achieve this result. Therefore, the voltage generated by the E field must exceed the binding potential in order to neutralize the charges. If the minimum reversing voltage (E-field) is known, removing ions from the surface would be straightforward, reducing the data collection time for the nEDM@SNS experiment.

At the University of Kentucky (UK), a small test setup was created to examine the behavior of ions in cryogenic liquids using electrodes and a scaled-down nEDM cell. The minimal reverse electric field required to remove ions from deuterated tetraphenyl butadiene (dTPB)-coated and uncoated polymethyl methacrylate (PMMA) cells are measured using cryogenic liquid nitrogen. However, in the nEDM@SNS experiment, helium will be used as the cryogenic liquid. Instead of using liquid helium, liquid nitrogen is used at UK because the electro-optics Kerr effect method will be used for the measurement of binding energies. The Kerr signal that can be acquired using this method in liquid helium is about 100 times weaker than the signal obtained in liquid nitrogen. Chapter 2 will focus on the discrete symmetries and their violations and try to explain how such violations led to the search for the nEDM. A detailed description of nEDM measurements and the experimental component of nEDM@SNS will be presented in Chapter 3. The theoretical underpinnings of how we estimate the binding energy of ions on plastic surfaces in liquid nitrogen via the electro-optical Kerr effect will be covered in Chapter 4. The measurement of the Kerr rotation using the triple modulation will be covered in Chapter 5. Chapter 6 will give a thorough experimental set-up of the cryostat, optical set-up, and high voltage. The results and a detailed data analysis of the cell charging impact and ion binding energy measurements on plastic surfaces are presented in Chapter 7. A summary and future outlook are provided in Chapter 8.

Chapter 2 Discrete Symmetries and their Violation

We introduce discrete symmetries and their violation in this chapter and attempt to briefly explain how such violations result in the search for nEDM experiments.

2.1   Discrete Symmetries

Symmetries are a crucial component in revealing how fundamental particles interact in order to comprehend particle physics. Parity transformation (P), charge conjugation (C), and time reversal symmetry (T) are discrete symmetries. The experimental search for a neutron electric dipole moment may disclose novel sources of time-reversal (T) and charge-conjugation-and-parity (CP) violation and test calculations that propose extensions to the Standard Model. Discrete symmetries and their violation will be discussed in detail in this section.

2.1.1   Parity Transformation

P-symmetry is a fundamental symmetry of the physical laws that changes the sign of the spatial coordinates while leaving time coordinates unchanged. The parity operator P represents a reflection of a quantum state in space, where all spatial coordinates (x, y, z) are changed to their opposite sign. It transforms a system's handedness, making a right-handed system left-handed under this discrete transformation. When the parity operator P operates on the system's state $\psi(x, y, z)$, it produces,

$$P\psi(x, y, z) = \psi(-x, -y, -z) \tag{2.1}$$

In quantum mechanics and particle physics, a parity transformation is used to examine the symmetry of physical systems. It is especially valuable for evaluating the behavior of subatomic particles and their interactions, since it may help us understand how the orientation of a system affects certain physical laws and principles.

2.1.2   Charge Conjugation Symmetry

Charge conjugation (C) symmetry is a fundamental symmetry of the physical laws of nature that relates particles to their corresponding antiparticles. The C-symmetry transformation involves replacing particles with their antiparticles, which reverses the sign of the electric charge of all particles and antiparticles. This transformation preserves the symmetry of physical processes involving the exchange or creation of particles. The charge conjugation operator is denoted by the symbol C and is defined as follows,

$$C|p\rangle = |\bar{p}\rangle \tag{2.2}$$

where $|p\rangle$ represents a particle state, $|\bar{p}\rangle$ represents its corresponding antiparticle state. C-symmetry also plays a crucial role in our understanding of the conservation of electric charge and the conservation of the total number of particles and antiparticles in the universe.

2.1.3 Time Reversal Symmetry

T-symmetry is a fundamental property of the physical law that states that a system's behavior at a particular time should be the same as its behavior at an earlier, or later, time if the direction of time is reversed. In quantum mechanics, this symmetry is related to the idea that the probability of a physical process occurring is unchanged when the process is run in either the forward or backward direction in time. This principle is known as time reversal invariance or time-reversal symmetry. The time flow is reversed through the time reversal transformation. The initial and final states' 'time components' signs are switched. Mathematically, the time reversal operator T is defined such that

$$T|\psi(t)\rangle = \langle\psi(-t)| \tag{2.3}$$

where $|\psi(t)\rangle$ represents the quantum state of the system at time t, and $\langle\psi(-t)|$ represents the conjugate of the quantum state of the system at the time $-t$, obtained by reversing the direction of time.
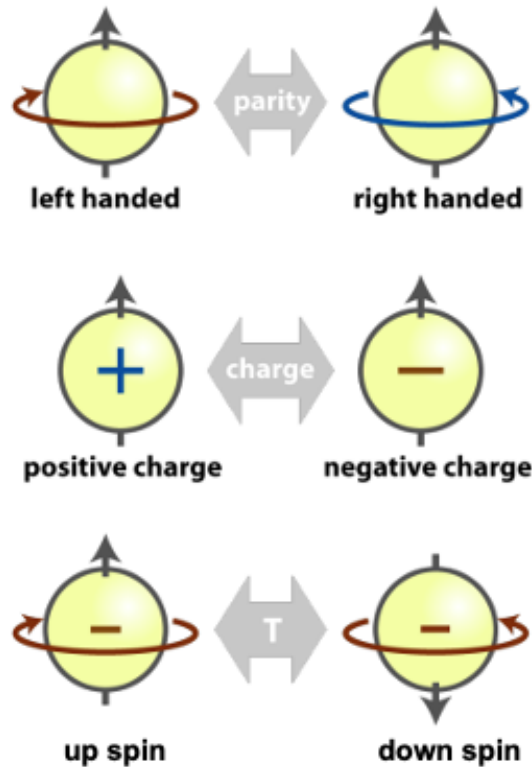
Figure 2.1: The action of the parity (P), charge conjugation (C), and time reversal (T) operators on a fundamental fermion. Picture credit [3].

Figure 2.1 displays the action of the parity, charge conjugation, and time reversal operators acting on a fundamental fermion.

The well-known CPT theorem connects charge conjugation C, parity inversion P, and time reversal T. A fundamental tenet of quantum field theory is the CPT theorem. It claims that, when C, P, and T operations are applied sequentially, regardless of order, all interactions remain invariant. Any Hermitian Hamiltonian-based local quantum field theory that is Lorentz invariant must possess CPT symmetry. Based on this theorem, breaking the time-reversal symmetry T also breaks the CP invariance.

Under the C, P, and T transformations, every physical system with strong and electromagnetic interactions is symmetric. In 1950, Purcell and Ramsey [30] argued that a precise measurement of the electric dipole moment of a fundamental particle would be a good test of the belief that charge conjugation, parity, and time reversal were all good symmetries of nature. They suggested that violations of these symmetries could lead to a nonzero electric dipole moment. Parity invariance in the weak interaction had never been tested before 1956. In 1956, Lee and Yang proposed one of the hypotheses stating the violation of parity conservation in weak interactions [31]. They suggested that certain subatomic particles could violate the symmetry between left- and right-handedness in the physical universe, thus breaking the conservation of parity. This hypothesis was confirmed by experiments conducted by Chien-Shiung Wu and her team in 1957, which demonstrated that some subatomic particles did not exhibit parity symmetry [4].

The confirmation of Lee and Yang's hypothesis led to a significant shift in the understanding of particle physics, and opened up new avenues of research into the nature of subatomic particles and the fundamental laws of the universe. The Wu et al. experiment [4] observed the parity violation in weak interactions, which is covered in Section 2.2.

2.2   Parity Violation in Weak Interactions

The natural explanation for symmetric transformations with regard to C, P, and T has long been taken for granted. Additionally, there was no proof that parity had been violated in electromagnetic and strong interactions. Up until 1957, there was no proof of parity violations in weak interactions. The weak interaction is governed by the Z boson, with $M_Z = 91.2\,\mathrm{GeV}$[32]. Chien-Shiung Wu and collaborators conducted the first experiment [4] testing for parity violation by observing the electrons emitted during the beta decay of ^{60}Co nuclei in 1957 in order to test one of Lee and Yang's hypotheses [31].

$$^{60}Co \rightarrow^{60} Ni + e^- + \bar{\nu}_e + 2\gamma \tag{2.4}$$
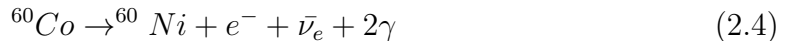
Wu polarized the ^{60}Co nuclei by cooling them in a cryostat with an applied magnetic field produced by a solenoid, as seen in Figure 2.2. The nuclear spins were polarized as a result of aligning with the applied magnetic field. NaI scintillation counters were positioned in the equatorial plane and the polar direction to determine the degree of polarization of the ^{60}Co source. An observed anisotropy of the released gamma rays can be utilized to gauge the degree of polarization of the nuclei since the direction

of the emitted gamma rays is connected with the direction of the magnetic moment of the ^{60}Ni nucleus. A tiny crystal of anthracene was positioned above the source to detect the beta particles. A photomultiplier on top of the cryostat was illuminated by scintillations created when beta particles generated from the source struck the anthracene.
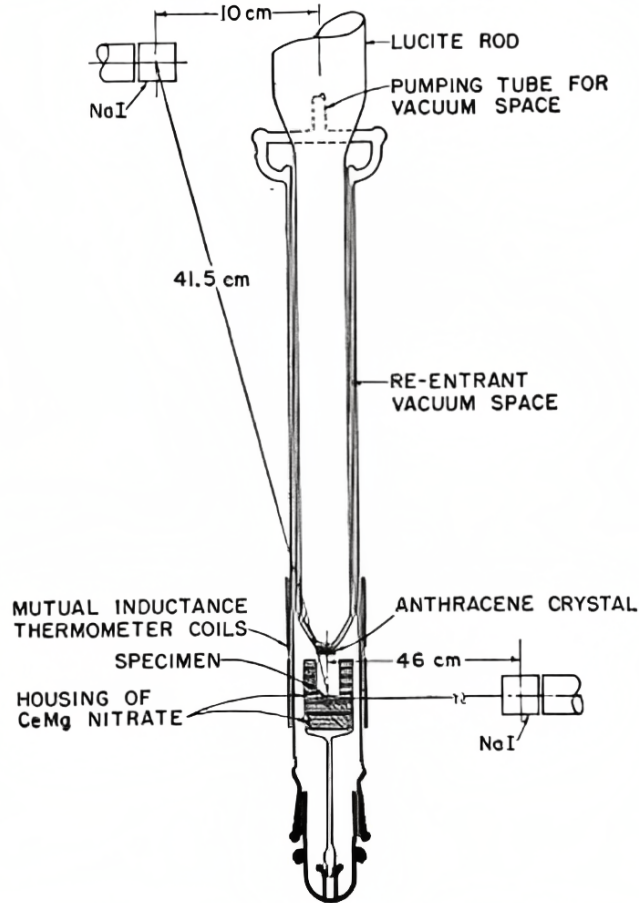
Figure 2.2: The schematic experimental setup used in Wu's experiment [4].

Wu et al. measured the beta and gamma counts in the two different magnetic field directions (upward and downward). By doing so, they effectively performed a parity transformation on the system. It would be evident that the system violates parity if the beta particles were emitting preferentially in a specific direction with respect to the nuclear spin. Figure 2.3 displays the outcomes of Wu et al. experiment. The gamma anisotropy, as measured by the NaI gamma detectors, is shown in the top plot as it varies over time. The nuclei are undoubtedly polarized, as evidenced by the difference in count rate between the equatorial and polar counters. The polarization goes to zero, as expected, as time goes on and the temperature rises.

The observed beta asymmetry is seen in the bottom plot when the external magnetic field is reversed in opposite directions. They unexpectedly found that more electrons are emitted opposite to that of the nuclear spin than they did in the same
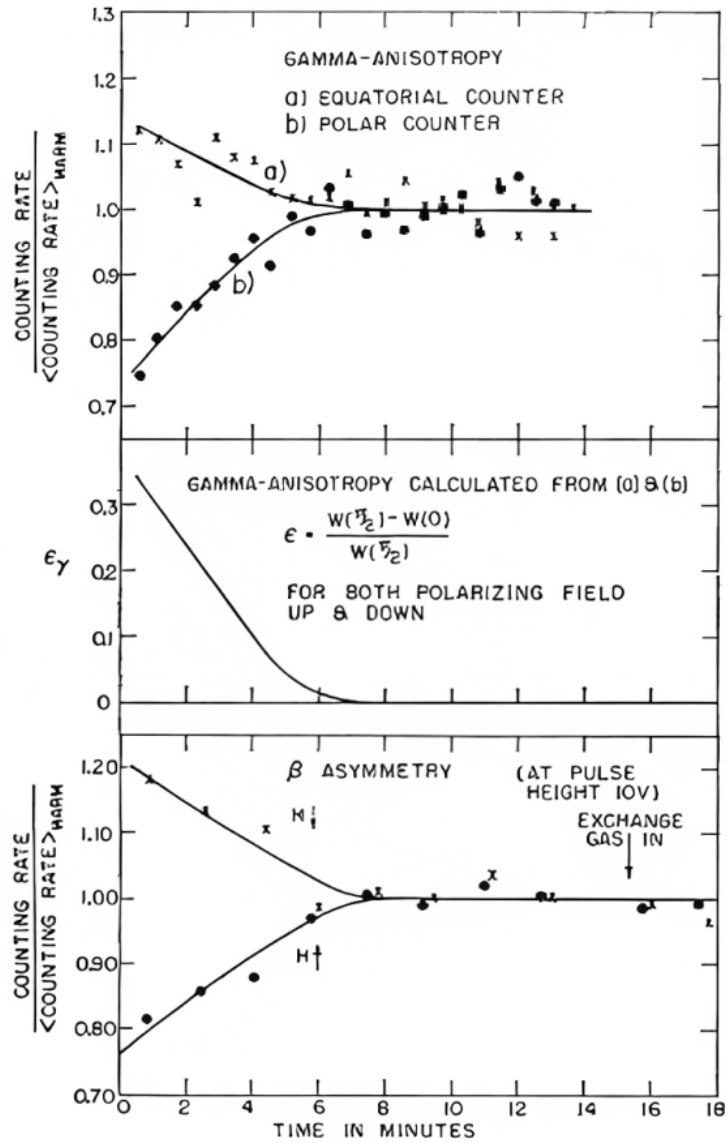
Figure 2.3: Wu et al.'s observations exhibiting gamma asymmetry and beta anisotropy in her research. Measurement of the gamma anisotropy (top) was employed to determine degree of nuclear polarization. The beta asymmetry (bottom) was measured when the magnetic field was reversed [4].

direction. This experiment revealed that the electrons were emitting preferentially in one direction, demonstrating that the weak interaction causing the decay did not follow parity symmetry.

2.3 CP Violation

The phenomenon known as CP violation occurs when the combined symmetry of charge conjugation (C) and parity (P) is broken. Careful observations of particle

decays and interactions may reveal the hallmark of CP violations. The asymmetry in particle-antiparticle decay rates is one such indicator. Asymmetry in the overall decay rates of a particle and its antiparticle may occur from CP violation. The mixing of various particle states, which may lead to asymmetries in the decay products, is another indicator. The physics of a process may not be the same when time is reversed, which is another way in which CP violation may result in a violation of time-reversal symmetry. Last but not least, CP violation may lead to asymmetries in the angular distributions of a particle's decay products. Understanding the basic properties of matter and the cosmos requires a thorough comprehension of CP violation. The identification and measurement of these signals may help us better understand the underlying causes of CP violation and the physical principles that control the behavior of matter at the subatomic scale. There have been reports of CP invariance violations in kaon [33], B meson [19], and D meson [34] decays. The quantity of CP violations that have been discovered thus far pales in comparison to what is required to account for the universe's baryon imbalance. Additional CP violation sources are required, and the neutron electric dipole moment (nEDM) could be one of them.

2.3.1 CP Violation in the Neutral Kaon Decays

Christenson et al. found in 1964 that neutral Kaon decays exhibit CP violation [35]. The neutral Kaon has two CP eigenstates, K_1 and K_2, with corresponding CP values of 1 and -1. K_1 only decays into two pions ($\pi^0\pi^0$ and $\pi^+\pi^-$), while K_2 only decays into three pions ($\pi^0\pi^0\pi^0$ and $\pi^+\pi^-\pi^0$). Neutral Kaons decay via weak interaction. The lifetime of the neutral Kaons are $\tau_L = 5.17 \times 10^{-8}$ s and $\tau_S = 8.93 \times 10^{-11}$ s [36]. Before this experiment, it was thought that $K_L = K_2$ and $K_S = K_1$. However, the Christenson et al. experiment shows that K_L may sometimes decay into two pions with a branching ratio of $\epsilon = 2 \times 10^{-3}$, which violates CP owing to the various CP values before and after the decay. This suggests that K_L and K$_S$ are a combination of the two CP eigenstates K_2 and K_1 along with the mixing parameter ϵ.

$$K_L = \frac{1}{\sqrt{1+\epsilon^2}}(K_2 + \epsilon K_1) \tag{2.5}$$

$$K_S = \frac{1}{\sqrt{1+\epsilon^2}}(K_1 - \epsilon K_2) \tag{2.6}$$

The CP violation resulting from the combination of CP eigenstates is sometimes referred to as an indirect CP violation. The phenomenon of CP violation in neutral kaon decay has significant implications for particle physics and the study of fundamental symmetries.

In 2001, the Belle collaboration observed large CP violation in the decay of B mesons[19], which is consistent with the higher range of values allowed by the constraints of the Kobayashi and Maskawa (KM) model [37]. Also, the LHCb detector reported the initial detection of a non-zero CP asymmetry in charm decays, utilizing substantial samples of $D_0 \to K^-K^+$ and $D_0 \to \pi^-\pi^+$ decays [34].

2.4 CP Violations in the Standard Model

The Standard Model (SM) is indeed a very successful framework that describes the strong, electromagnetic, and weak interactions of subatomic particles. The predictions of the SM have been extensively tested and confirmed by numerous experimental observations.

There are two possible sources of CP violation within the SM. The first one is the CKM (Cabibbo-Kobayashi-Maskawa) matrix, which describes the mixing between different generations of quarks and is responsible for CP violation in the weak interaction. The matrix is usually parameterized in terms of four real parameters and one complex phase. The real parameters are known as the mixing angles and determine the probability of a quark of one flavor transforming into a quark of another flavor in the weak interaction. The complex phase is responsible for CP violation in the weak interaction, and this has been experimentally observed in the decay of neutral kaons, B mesons, and D mesons.

The second source of CP violation in the SM is the θ term [[38]] from the strong interaction, which is sometimes called the strong CP problem [39]. The θ term is a hypothetical term in the QCD (quantum chromodynamics) Lagrangian that violates CP symmetry. However, experimental observations have not detected any CP violation in the strong interaction, which suggests that the θ term is either zero or very small. This is known as the strong CP problem. Theoretical calculations have shown that the neutron Electric Dipole Moment (nEDM) is proportional to the value of the theta term, and a rough estimation is nEDM $\sim \theta \times 10^{-16}$ e-cm [[40], [41]]. Experimental measurements of the nEDM provide a way to test the presence of the theta term in the QCD Lagrangian and search for new physics beyond the Standard Model. The current experimental upper limit on the nEDM is very small, at around 1.8×10^{-26} e-cm [25], which implies that the value of the $\theta < 10^{-10}$.

Thus, experimental measurements of the nEDM can test these proposed solutions and search for new physics beyond the Standard Model. Ongoing experiments are searching for the nEDM with increasing precision, and future experiments are planned to push the sensitivity even further.

However, both of these sources of CP violation are insufficient to explain a critical phenomenon in our universe — that of the baryon asymmetry. Sufficient CP violation can give rise to a preference for matter over anti-matter (see next subsection). This is a preference that is reflected in our current universe which is matter dominated and not one with equal amounts of matter and anti-matter. In the following section, we briefly explore the implication of this reality on new sources of CP-violation.

2.5 Neutron Electric Dipole Moment (nEDM)

The nEDM is a measure of the distribution of electric charge within the neutron, and for many years, it was widely accepted that the laws of physics should exhibit symmetry under both parity (P) and time reversal (T) transformations. However, it is important to note that permanent electric dipole moments (EDMs) that break these discrete symmetries are of interest. In particular, the neutron EDM has been

extensively searched for experimentally. This is because the only quantum number that defines a neutron is its spin, and there are no degenerate states. As a result, only a permanent EDM that is aligned or anti-aligned with the neutron's spin can be detected. The nEDM is predicted to be extremely small in the Standard Model of particle physics. But if nEDM is not zero, it could mean that there are new sources of CP violation that are not taken into account by the Standard Model. This could help us figure out where the difference between matter and antimatter came from in the universe, which is one of the biggest questions in modern physics.

When two opposite charges of magnitude q are placed next to one another, an electric dipole moment is created, and it is specified to point in the direction of the positive charge. If $\vec{r}$ is the distance between two opposite charges (q and $-q$), the electric dipole moment is given by the Equation 2.7 and is illustrated by the Figure 2.4.

$$\vec{d} = q\vec{r} \tag{2.7}$$
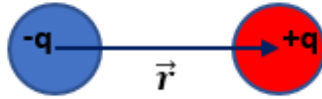
Figure 2.4: Diagram of an electric dipole moment.

The neutron is electrically neutral, but if there is any movement between its charged internal components (quarks and gluons) and its center of mass, it may develop an electric dipole moment (EDM). The time reversal and parity symmetries would both be broken by such an EDM. This may be understood by looking at the Hamiltonian of a neutron in the presence of electric ($\vec{E}$) and magnetic ($\vec{B}$) fields.

$$H = (-\mu_n \vec{S} \cdot \vec{B} - d_n \vec{S} \cdot \vec{E})/S \tag{2.8}$$

In this case, the magnetic and electric dipole moments of the neutron are denoted by μ_n and d_n, respectively. S is the magnitude of spin, while $\vec{S}$ is the spin vector. Equation 2.8 relates the electric dipole moment d_n to the electric field $\vec{E}$, and it is a fundamental equation that characterizes the behavior of electrically charged particles. When the parity and time transformation is applied, the product of $\vec{S} \cdot \vec{E}$ changes signs but in contrast, the product of $\vec{S} \cdot \vec{B}$ remains unchanged. Therefore, the electric dipole moment is a P and T violation quantity. Thus, the combined symmetry CP is broken due to the presence of CPT symmetry.

Figure 2.5 provides a visual representation of the behavior of different physical quantities when subjected to time reversal (T) and parity (P) transformations. Specifically, the figure shows how these quantities transform under T and P operations, which are fundamental symmetries of the laws of physics.

In the Standard Model of particle physics, the EDM of the neutron arises from loop diagrams involving virtual W and Z bosons in the weak interaction. These
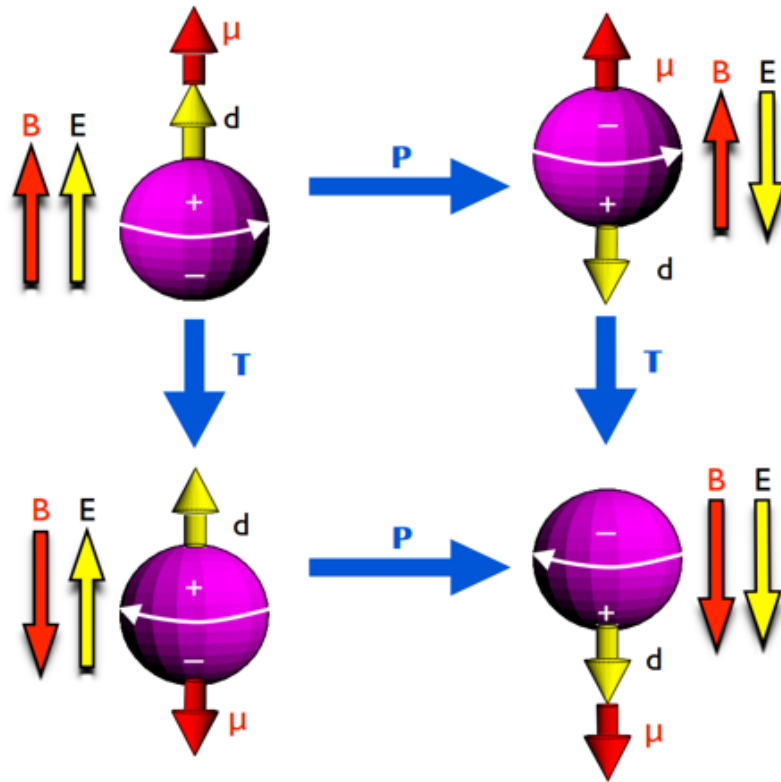
Figure 2.5: A permanent EDM is reversed by the parity operation. It is unchanged by time-reversal, but this reverses the spin, which specifies the orientation, so a non-zero EDM would be a violation of both T and P symmetry [5].

diagrams are typically third-order Feynman diagrams and involve the exchange of virtual particles between the quarks inside the neutron.

Chapter 3 nEDM@SNS Experiment Overview

The search for the neutron electric dipole moment (nEDM) is an active area of research in particle physics. In 1994, Golub and Lamoreaux proposed a novel approach to improve the measurement sensitivity of nEDM. The approach involved using ^{3}He as a co-magnetometer and the superthermal method to produce ultracold neutrons (UCNs). Recently, a collaborative project has been initiated at the Spallation Neutron Source (SNS) located at ORNL to measure the nEDM with greater sensitivity. The new measurement of nEDM@SNS is anticipated to have targeted sensitivity that is ~ 100 times better than the current limit of 1.8×10^{-26}e-cm [25]. This development is significant as it has the potential to contribute to a better understanding of the fundamental symmetries of the universe.

3.1   Ultracold Neutron (UCN) Production

First, neutrons must be acquired in order to measure the EDM of the neutron. since 1980, ultracold neutrons have been utilized in EDM studies due to their ability to greatly reduce the motional field effect and enhance the interaction duration with the surrounding fields. Utilizing the Fundamental Neutron Physics Beamline (FNPB) of the Oak Ridge National Laboratory's Spallation Neutron Source, the intended nEDM@SNS experiment will be conducted. In the FNPB line, a high-intensity proton beam is directed onto a liquid mercury target. When the protons collide with the target nuclei, a cascade of nuclear reactions occurs, which results in the production of a large number of neutrons. These neutrons are then moderated and collimated to create a beam of neutrons that can be used for a variety of experiments in fundamental neutron physics [42]. In a neutron moderator, also known as a cold source, liquid hydrogen or deuterium is used to produce cold neutrons. Through a process known as superthermal [[43], [44]], cold neutrons will be down-scattered in a superfluid ^{4}He (SFHe) bath, generating UCNs.

The superfluid ^{4}He elementary excitation dispersion curve (Landau-Feynman dispersion curve), shown in Figure 3.1, together with the free neutron dispersion curve, provide the fundamental framework. When a collision between a neutron and ^{4}He take place, it is imperative to satisfy the fundamental principles of energy and momentum conservation. This necessitates that the collision phenomenon can solely occur at the specific energy points where the respective dispersion curves of the two particles intersect with each other. For free neutrons to come to rest and become ultra-cold neutrons, they must have both energy $E = \hbar\omega$ and momentum $p = \hbar k$ that satisfy the free neutron dispersion curve,

$$\omega(k) = \frac{\hbar k^2}{2m_n} \tag{3.1}$$

where m_n is the mass of the neutron. The intersection between these lines occurs at a neutron wavelength of 8.9 Å, which allows cold neutrons with an energy of 11 K

to excite the superfluid ^{4}He and lose the necessary energy in the process, resulting in the production of ultracold neutrons. This process is commonly referred to as the superthermal process. Thus, cold neutrons with kinetic energies of 11 K and a de Broglie wavelength of 8.9 Å can be down-scattered into the UCNs by emitting a phonon. When ultracold neutrons are produced, the majority of their kinetic energy is transferred to the emitted phonons. As a result, the ultracold neutrons have very low energy and are completely reflected at all angles of incidence. This low energy causes the ultracold neutrons to remain trapped within the measurement cell [45]. On the other side, UCNs may also absorb energy $\omega(k)$ and be up-scattered to cold neutrons; however, the rate of the reverse process (up-scattering) is much lower because the number of ^{4}He atoms with high energy is significantly smaller than the number of atoms with low energy, as dictated by the Boltzmann distribution ($e^{-\frac{E}{kT}}$) when the temperature of the ^{4}He is below 1 K. In addition to its role in the production of
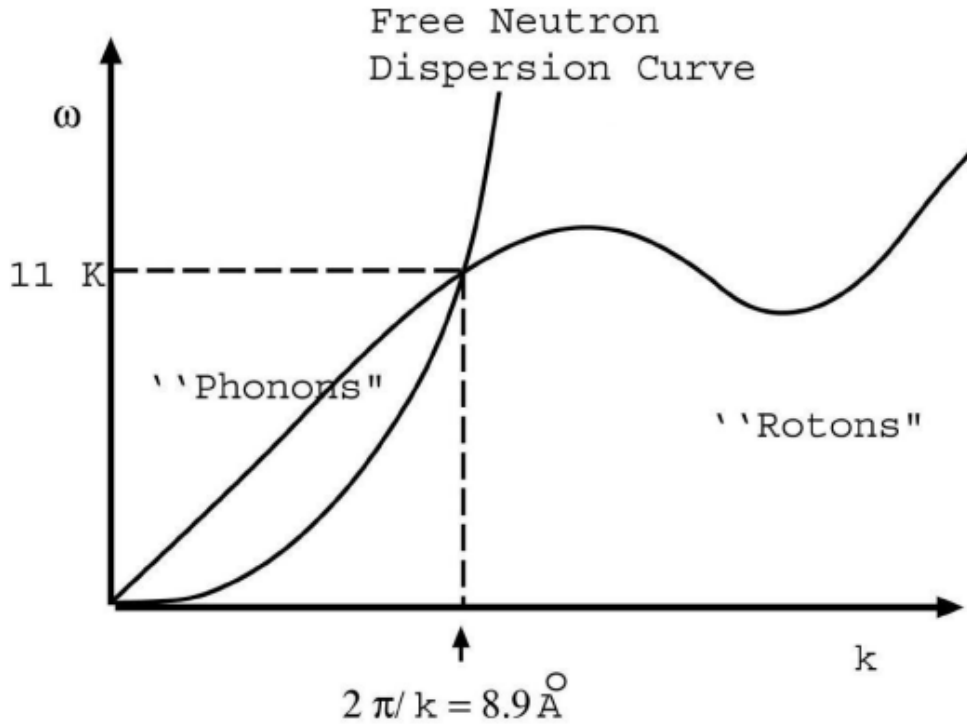
Figure 3.1: The phonon-roton dispersion curve for superfluid helium is shown coupled with the free neutron dispersion curve (parabola) [6].

ultracold neutrons, superfluid helium-4 also acts as a reliable insulator for the high electric field used in the nEDM experiment [46].

The measurement cell used in the nEDM@SNS experiment is designed to trap ultra-cold neutrons (UCNs) inside it. The cell is coated with deuterated TetraPhenyl Butadiene-doped deuterated PolyStyrene (dTPB-dPS), which has a low neutron absorption cross-section and high wavelength shifting efficiency [47]. The Fermi-potential of the deuterated polystyrene wall is 134 neV [48], which means that neutrons with

energies lower than this value will experience total reflection from the wall. This led to an increase in UCN density inside the measuring cell. However, UCNs are unstable particles and in addition to beta decay can be lost through processes such as neutron absorption by ^{3}He, up-scattering, and wall absorption. Therefore, the overall neutron loss rate can be expressed as,

$$\frac{1}{\tau} = \frac{1}{\tau_\beta} + \frac{1}{\tau_{3He}} + \frac{1}{\tau_{up}} + \frac{1}{\tau_{wall}}, \tag{3.2}$$

where τ_i is a time constant for each loss. To lower the rate of ^{3}He neutron absorption, the measurement cell's superfluid ^{4}He must be isotopically purified, removing the unpolarized ^{3}He from ^{4}He. The exceptional characteristics of superfluid ^{4}He, which encompass its non-existent neutron absorption, render it a highly advantageous medium for the storage of ultracold neutrons (UCN) with storage durations that are comparable to that of the neutron's lifetime. The target for the mean neutron lifetime in the superfluid ^{4}He-filled trap is $\sim$500 seconds, and the nominal production rate of trapped UCNs is $\sim 0.3~UCN/(cm^3.sec)$ [49]. In the superfluid ^{4}He, the neutron density will therefore reach $\rho_n \approx 150$ UCNs/cm^3 after approximately 500 seconds of UCN generation. With a more potent cold neutron source, the UCN density will undoubtedly increase as the cold neutron flux increases.

3.2   Measurement Procedure

The neutron EDM is determined by comparing the neutron Larmor frequency in parallel and antiparallel magnetic and electric fields. A homogeneous magnetic field of 30 mG is applied across the measurement volume, and the polarized UCNs are permitted to precess freely about this field. Moreover, the cell is subjected to an electric field of 75 kV/cm that is parallel to the magnetic field. In the presence of parallel magnetic and electric fields, the precession frequency is

$$h\nu_{\uparrow\uparrow} = |2\mu_n B + 2d_n E|. \tag{3.3}$$

If the electric field direction is reversed, the precession frequency is given by,

$$h\nu_{\uparrow\downarrow} = |2\mu_n B - 2d_n E|. \tag{3.4}$$

The neutron EDM is extracted from the difference between the two frequencies,

$$d_n = \frac{h\Delta\nu}{4E}. \tag{3.5}$$

The largest challenge of the experiment is to ensure that the magnetic field does not change during these two measurements. Equation 3.5 gives the electric dipole moment of the neutron, which has statistical uncertainty

$$\sigma_d \sim \frac{1}{ET\sqrt{mN}}. \tag{3.6}$$

The variables E, T, N, and m are important to optimize the nEDM@SNS experiment. E is the strength of the applied electric field, T is the duration of the neutron precession measurement, N is the number of neutrons per measurement, and m is the number of measurements. These variables are crucial in determining the sensitivity and precision of the experiment for detecting the tiny effects of the neutron's electric dipole moment (EDM). A combination of these variables, along with other experimental factors, enables the nEDM@SNS experiment to achieve a high level of sensitivity in measuring the neutron's EDM.

3.2.1   Experimental Method

The experiment is based on a concept put forth by Golub and Lamoreaux [29]. This approach takes advantage of superfluid helium properties to increase the strength of the applied electric field, number of neutrons, and measurement time. Ultracold neutrons are trapped inside the measuring cells, which are filled with superfluid ^{4}He bath [45]. Polarized ^{3}He atoms are diffused in the measuring cell. Due to the Schiff screening [50] of the nucleus, the ^{3}He atom has a very small EDM and acts as a co-magnetometer, measuring magnetic fields in the same area as the UCNs. The ^{3}He atom can measure the magnetic field's effect on the neutrons over time with a high degree of accuracy. In a recent experiment carried out at the Institut Laue-Langevin (ILL), significant experimental evidence was presented regarding the usefulness and importance of utilizing co-magnetometers, which could either have their geometric effect or their efficacy in reducing noise caused by magnetic fluctuations [[51], [52]]. SQUID (superconducting quantum interference device) magnetometers are highly sensitive devices that can detect even tiny changes in magnetic fields. In the nEDM experiment, SQUID magnetometers are used to measure the magnetic field created by the precessing magnetization of the polarized ^{3}He atoms in the measurement cell.

The ^{3}He also serves as a neutron spin analyzer. The neutron absorption cross-section of ^{3}He is highly spin-dependent: 5300 barns at 1.8 Å for the singlet state, rising as $1/v$ (where v is the neutron velocity), and almost zero for the triplet state [53] due to the Pauli exclusion principle applied to the closed shell intermediate state ^{4}He. The reaction products of neutron absorption on ^{3}He nucleus are a proton and a triton, which have a shared energy of 764 keV.

$$n + {}^3He \rightarrow {}^3H + p + 764 keV. \tag{3.7}$$
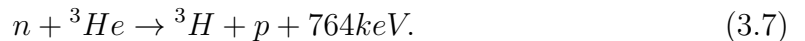
The energy released to the products of the n-^{3}He capture decay excites the liquid helium and results in the production of ultraviolet scintillation light. The scintillation rate is dependent on the alignment of the spins of the UCN and ^{3}He because the neutron-^{3}He absorption cross section is spin-dependent. It follows that the scintillation rate changes with time, given by

$$s(t) \propto 1 - \vec{P_n}.\vec{P_3} \propto (1 - P_n P_3 \cos \phi_{n3}) \propto (1 - P_n P_3 \cos[(\gamma_3 - \gamma_n)B_0 t]), \tag{3.8}$$

Where ϕ_{n3} is the angle formed by the neutron and ^{3}He's spin axes. Here P_n and P_3 are the polarizations of the neutrons and the ^{3}He, respectively, and γ_3 and γ_n are

the gyromagnetic ratios of the ^{3}He and the neutrons, respectively. Ultraviolet (UV) photons with a wavelength of 80 nm are produced as a product of this reaction and are emitted in the superfluid ^{4}He. The dTPB coating on the cell wall acts as a wavelength shifter, which absorbs the UV photons produced in the UCN detection process and re-emits them as visible light at 400 nm. They are then detected by photomultiplier or SiPM (silicon photomultiplier) tubes. This capture rate is dependent on the angle between the polarization of neutrons and ^{3}He (ϕ_{n3}). The difference between the neutron precession frequency and the ^{3}He precession frequency can be extracted from the modulation frequency of the scintillation light. It should be noted that SQUID magnetometers are used to determine the ^{3}He precession frequency. The neutron EDM signature would manifest as a shift in the neutron-^{3}He precession frequency difference corresponding to the reversal of the E relative to the B without or even with a matching change in ^{3}He precession.

3.2.2 Dressed Spin Technique

The so-called "dressed-spin approach" will be employed to search for the neutron EDM signal in addition to a SQUID magnetometer for tracking the ^{3}He's polarization. The time-averaged Larmor precession frequency for the neutron and ^{3}He is modified differently by the critical dressing approach, which involves an additional oscillating magnetic field B_1 perpendicular to the main holding magnetic field B_0 [54], resulting in an effective gyromagnetic ratio given by,

$$\gamma' = \gamma J_0(\gamma \frac{|\vec{B_1}|}{\omega_1}) = \gamma J_0(x), \tag{3.9}$$

where $x = \gamma \frac{|\vec{B_1}|}{\omega_1}$, ω_1 is the frequency of the applied dressing field. J_0 is the zeroth order Bessel function. Specifically, the dressed gyromagnetic ratios for ^{3}He and neutron in an alternating field B_1 are,

$$\gamma'_3 = \gamma_3 J_0(x_3) \tag{3.10}$$

$$\gamma'_n = \gamma_n J_0(x_n) \tag{3.11}$$

By introducing a B_1 field perpendicular to the static B_0 field, which satisfies

$$\gamma_3 J_0(x_3) = \gamma_n J_0(x_n), \tag{3.12}$$

it is possible to precess at the same frequency for neutrons and ^{3}He atoms. This situation is called "critical dressing". The dressing RF field parameter x is adjusted to eliminate the oscillating component of the scintillation light, which is dependent on the relative orientation of the electric and magnetic fields. By reversing the direction of the electric field, the relative orientation of the fields changes, resulting in a change in the oscillation frequency of the scintillation light. The value of x for which the oscillation frequency is zero is known as the critical dressing, and any change in x at this point would indicate the presence of an EDM. By carefully controlling the magnetic field and the orientation of the electric field, the experiment can be made insensitive to background magnetic fields, allowing for precise measurements of the neutron EDM.

3.2.3 Electric Field Requirements for nEDM@SNS

The measurement of the neutron EDM involves using a magnetic field to manipulate the spin of the neutron. Specifically, the experiment involves sending a beam of neutrons through a region where they are subjected to an electric field and a magnetic field. The measurement of the nEDM is a sensitive experimental technique that requires precise control of the magnetic and electric fields, as well as careful measurement of the neutron precession direction.
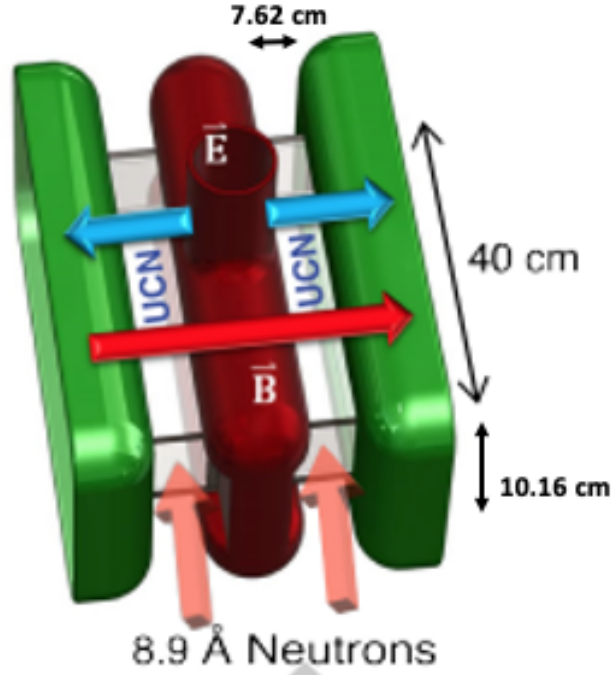
Figure 3.2: Schematic diagram of nEDM@SNS measuring cells and high voltage electrodes. The centre (red) electrode is high-voltage while the green electrodes are grounded. External coils create the magnetic holding field $\vec{B}$, which is not shown in this diagram. All fields are reversible [7].

In Figure 3.2, a diagrammatic representation of the measurement cells that are located between the high-voltage electrodes is displayed. However, if the magnetic field is non-uniform, then the neutron spins will precess at different rates depending on their location within the field. This can produce a false nEDM. Therefore, a uniform magnetic field is necessary to ensure that the measured signal is solely due to the neutron EDM. The nEDM@SNS experiment has opted for an operating magnetic holding field of 3 μT, which has been chosen to optimize the trade-off between systematic errors and statistical uncertainties. The magnetic field will be maintained at a uniform level of several ppm/cm. To enhance the sensitivity of the measurement, it is necessary to maximize the electric field, and flip the orientation of the

electric field frequently to control systematics. The target for the electric field is 75 kV/cm at the neutrons. Assuming a neutron EDM of 3×10^{-28} e-cm, this electric field corresponds to an energy shift of $\Delta E = 2.25 \times 10^{-23}$ eV. Consequently, the systematic effects of magnetic fields related to electric field reversal must be less than $\delta B_{sys} = \Delta E / \mu_n = 2.25 \times 10^{-23} eV / 6.02 \times 10^{-8} eV/T = 0.37$ fT. The stability and uniformity of the electric field are limited by the motional magnetic fields, as imposed by the principles of special relativity. Specifically, a particle, such as a neutron, moving with velocity $\vec{v}$ in an electric field experiences a motional magnetic field of

$$\vec{B_m} \approx -\frac{\vec{v}}{c^2} \times \vec{E^2}. \tag{3.13}$$

When this effect is paired with a gradient in a magnetic field, it will result in a linear frequency shift that is proportional to $\vec{E}$. The detailed calculation is shown in M Behzadipour thesis [55]. For nEDM@SNS experiment, the goal of the electric field is 75 kV/cm. Therefore, for a particle traveling perpendicular to the electric field with a $\vec{v}/c$ ratio of 10^{-8} (common for UCNs velocities), the motional magnetic field is roughly 250 pT, substantially bigger than 0.37 fT. Additionally, the magnitude of the overall holding field will shift due to the presence of this motional magnetic field by

$$B' = \frac{B_m^2}{2B_0} \approx 10 fT. \tag{3.14}$$

Thus, the fractional change in B' brought on by a little alteration in the electric field, which is given by,

$$\frac{\Delta B'}{B'} \approx 2\frac{\Delta E}{E}. \tag{3.15}$$

To maintain the systematic influence on the extraction of the EDM owing to magnetic field fluctuation below 0.2 fT [28], the permitted variation in the electric field magnitude from one direction to the other using these findings and Equation 3.15 is

$$\frac{\Delta E}{E} \leq \frac{\Delta B'}{2B'} = \frac{0.2 fT}{2(10 fT)} = 0.01. \tag{3.16}$$

This supports the idea that, in order to maintain the necessary sensitivity, the electric field's magnitude must vary by less than 1% when the field is reversed.

Neutrons that are scattered from the beam will scatter further in the dTPB-coated cell walls and HV electrodes, resulting in long path lengths within these materials. A significant number of these neutrons will be absorbed through the n + p → d + γ (2.2 MeV) reaction, which will generate prompt γ rays that can penetrate the helium-4 inside the cell and lead to ionization. However, the application of an electric field will significantly decrease ion-electron recombination, allowing most of the charge produced to separate and migrate toward the electrically-insulating inner walls of the measurement cells. According to initial MCNP simulations and taking into account the observed recombination probabilities obtained from a Seidel [56] paper, an estimated quantity of ∼6 μC of free charge is predicted to be generated per fill. To mitigate this issue, the possibility of incorporating a layer of neutron-absorbing

[6]Li-loaded material situated in close proximity to the cell's interior is under consideration. Such a measure is anticipated to result in a reduction of the free charge inside the cell by approximately a factor of two.

Additionally, some levels of free charge will be produced by the β-decay of the UCNs inside the cell, cosmic rays, and the decaying nuclei of contamination in the vicinity of the cell that were activated by either the direct cold neutron beam or scattered neutrons. Nevertheless, it is projected that the impact of these sources on the electric field will be minor in comparison to the effects of prompt γ generation during filling. The charge rate predictions from several sources have been compiled into a single collaboration document.

In Table 3.2, the ionization current is provided by the ionizing source for each stage. τ_n denotes the neutron's effective lifespan in these cells; a value of 500 s was selected to account for neutron absorption by ^{3}He, up-scattering, wall losses and β-decay. The average ionization energy for superfluid helium is also 43 eV in this document [1]. It is estimated that the rate of γ-rays entering the cell is 15 kHz and that the initial number of neutrons in each cell is around 3×10^5. During the whole measurement cycle, it is assumed that the electric field is active and at full strength.

The net charge contribution of each source is determined by integrating the charging currents (Table 3.2) with respect to time across the duration of each stage. The sum of these numbers results in 8.68 nC/cycle. The capacitance of the cell is predicted to be 16 pF[1]. This indicates that the decrease in voltage per cycle for these sources will be

$$\Delta V = \frac{8.68 \ nC}{16 \ pF} = 543V.$$ (3.17)

Consequently, the electric field will shift by a certain percentage per cycle, as shown by the following equation:

$$\frac{\Delta E}{E} = \frac{\Delta V}{V} = \frac{543 \ V}{635 \ kV} \times 100\% = 0.0855\%.$$ (3.18)

The 635 kV value was derived from the most recent revision of the experimental setup[28]. After the specified number of cycles, the field's overall strength will decrease by 1%.

$$N = \frac{1\%}{0.0855\%/cycle} \approx 11cycles.$$ (3.19)

The presence of separated charges within the experimental setup may lead to complications, as these charges will generate their own static electric fields that could weaken the overall electric field experienced by UCNs in the target area. This may occur due to screening effects caused by the separated charges. The high-voltage electrode (red in Figure 3.2) will be loaded with a fixed amount of charge (around ($\sim$70 μC)) by a Cavallo charging system [57] and then isolated, while the outside electrodes (green in Figure 3.2) are connected to ground. This design is necessary to achieve the required E-field strength of 75 kV/cm inside the cell, while reducing the demands on the high-voltage feedthroughs. Charges on the cell walls cause charges

Table 3.1: Ionization currents expected in the SNS-nEDM cell. Data from internal collaborative communications that has been copied "as is" (without alteration)[1].

Ionization Currents		
Stage	Type	Current (pA)
UCN fill	Beam neutron decays	0.48
	γ rays	9
	cosmic rays	0.12
(800 s)	Total for fill stage	9.6
Measurement	UCN decays	$0.48e^{-t/\tau_n}$
	n- ^{3}He capture	$0.14e^{-t/\tau_n}$
	cosmic rays	0.12
	γ rays	0.4
(700 s)	Total for measurement stage	$0.5 + 0.6e^{-t/\tau_n}$
Cleanup	UCN decays	$0.12e^{-t/\tau_n}$
	n- ^{3}He capture	$0.034e^{-t/\tau_n}$
	cosmic rays	0.12
	γ rays	0.4
(421 s)	Total for cleanup stage	$0.5 + 0.15e^{-t/\tau_n}$

on both electrodes to rearrange, decreasing the E-field screening effect. However, this charge rearrangement increases the E-field inside the cell wall material and, more significantly, increases the E-field in the gap between the electrodes and the cell. This larger E-field can lead to undesirable electrical breakdowns and limit the achievable E-field strength inside the cell.

In order to avoid a false EDM signal being detected, the charge must be removed from the measurement cell. This number is based on the premise that every charged particle created contributes. However, recombination effects will likely decrease the actual amount of charges, lengthening the number of cycles before the charge must be removed.

The behavior of ions and electrons on dielectric surfaces in super-cooled liquids is not well understood. Previous research [7] has shown that charging of the PMMA "cell" occurs in liquid nitrogen and superfluid helium-4, leading to a decrease in the net electric field. However, reversing the electric field can eliminate this charging effect. To minimize the impact of cell charging on the nEDM@SNS experiment and achieve the necessary sensitivity, the electric field should be regularly reversed.

The Cavallo charging system [57] in the nEDM@SNS experiment requires 17 cycles

to deliver 750 kV [58], and the complete reversal of the electric field takes a long time. However, knowing the minimum amount of electric field reversal required to remove charges from the PMMA surface can significantly reduce data collection time in the nEDM@SNS experiment. Therefore, it is crucial to measure the binding energy of ions on insulating surfaces in cryogenic liquids.

This research work investigates the feasibility of using the electro-optic Kerr effect (which is explained in Chapter 5) to measure the charging of the measurement cell and the binding energy of ions on plastic surfaces. However, the Kerr signal is weaker in liquid helium compared to liquid nitrogen [7]. Therefore, the study was carried out in cryogenic liquid nitrogen to measure the binding energy of ions on plastic surfaces. In the future, the experiment can be conducted in liquid helium to further explore its impact on the nEDM@SNS experiment.

Chapter 4 Theoretical Background of Kerr Measurement

To examine the impact of cell charging and the binding energy of ions on insulating surfaces in cryogenic liquid nitrogen on the sensitivity of the nEDM@SNS experiment, a miniature test rig was devised and built. The system had to be capable of producing electric fields of order several 10s kV/cm inside a cryogenic liquid (liquid nitrogen or superfluid helium-4), a dummy PMMA "cell" had to be inserted between the high voltage electrodes, and the stability of the electric field had to be monitored in the presence of ionizing radiation. A sketch drawing of the concept is seen in Figure 4.1. Therefore, the electro-optic Kerr effect is one of the most effective methods for
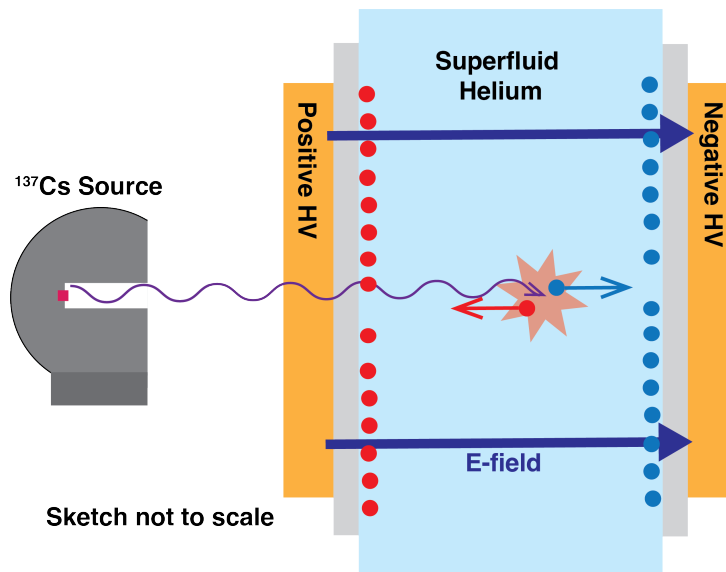
Figure 4.1: Cell charging fundamentals in cryogenic liquid configuration.

monitoring the electric field.

4.1 Electro-Optic Kerr Effect

Dielectrics are often isotropic in their electric properties owing to the random orientation of their molecules. When a strong electric field is applied to a dielectric medium, the electric field causes the molecular dipoles to align with the field, and the dielectric medium becomes birefringent, causing incoming linearly or circularly polarized light to become elliptically polarized as it propagates through the medium. This birefringence caused by an applied electric field is known as the Kerr effect.

This effect can induce or modify birefringence, which is the property of a material polarization-dependent index of refraction to split a single light beam into two beams of different polarizations that travel at different speeds and refract at different angles. By modifying the refractive index of a material through the application of an electric

field, the electro-optic effect can be used to control the polarization of light passing through the medium.

When light travels through a medium in the presence of an electric field, the electro-optic effect may be noticed. The electric field that is applied to the medium may modify or induce birefringence by modifying the medium's refractive index. It is called the electro-optic effect. The change in refractive index in the Kerr effect is proportional to the square of the electric field strength due to the nonlinear nature of the effect. Therefore, this effect is also called the quadratic effect in an electric field.

$$\Delta n = f(E^2). \tag{4.1}$$

In this section, a mathematical framework for the linear electro-optic effect is formulated based on "Nonlinear Optics" (third edition) by Boyd [8] and Polarized Light (second edition, revised and expanded) by Goldstein [59].

The constitutive relationship between the field vectors $\vec{D}$ and $\vec{E}$ in an anisotropic material has the form

$$D_i = \epsilon_0 \sum_j \epsilon_{ijk} E_j \tag{4.2}$$

or,

$$\begin{bmatrix} D_x \\ D_y \\ D_z \end{bmatrix} = \epsilon_0 \begin{bmatrix} \epsilon_{xx} & \epsilon_{xy} & \epsilon_{xz} \\ \epsilon_{yx} & \epsilon_{yy} & \epsilon_{yz} \\ \epsilon_{zx} & \epsilon_{zy} & \epsilon_{zz} \end{bmatrix} \begin{bmatrix} E_x \\ E_y \\ E_z \end{bmatrix}. \tag{4.3}$$

According to a general mathematical result, using an orthogonal transformation, every real symmetric matrix may be written in diagonal form. Physically, this finding means that some other new coordinate system (X, Y, Z) exists, connected to the coordinate system (x, y, z) by rotation of the coordinate axes. The Equation 4.3 can be simply written as

$$\begin{bmatrix} D_X \\ D_Y \\ D_Z \end{bmatrix} = \epsilon_0 \begin{bmatrix} \epsilon_{XX} & 0 & 0 \\ 0 & \epsilon_{YY} & 0 \\ 0 & 0 & \epsilon_{ZZ} \end{bmatrix} \begin{bmatrix} E_X \\ E_Y \\ E_Z \end{bmatrix}. \tag{4.4}$$

This new coordinate system is called the principal-axis system because it is represented by a diagonal matrix.

The energy density per unit volume of a wave that propagates across an anisotropic material is given by

$$U = \frac{1}{2}\vec{D}.\vec{E} = \frac{1}{2}\epsilon_0 \sum_{ij} \epsilon_{ij} E_i E_j. \tag{4.5}$$

The energy density may be defined in terms of the components of the displacement vector in the principal-axis coordinate system as

$$U = \frac{1}{2\epsilon_0}\left[\frac{D_X^2}{\epsilon_{XX}} + \frac{D_Y^2}{\epsilon_{YY}} + \frac{D_Z^2}{\epsilon_{ZZ}}\right]. \tag{4.6}$$

If we consider,

$$X = \frac{D_X}{\sqrt{2\epsilon_0 U}}, Y = \frac{D_Y}{\sqrt{2\epsilon_0 U}}, Z = \frac{D_Z}{\sqrt{2\epsilon_0 U}}, \tag{4.7}$$

these ellipsoids may be characterized by their coordinates (X, Y, Z) as

$$\frac{X^2}{\epsilon_{XX}} + \frac{Y^2}{\epsilon_{YY}} + \frac{Z^2}{\epsilon_{ZZ}} = 1. \tag{4.8}$$

Equation 4.8 describes the optical indicatrix or index ellipsoid. The equation defining the index ellipsoid assumes its simplest form in the principal-axis system; in other coordinate systems, it is provided by the generic formula for an ellipsoid,

$$\left(\frac{1}{n^2}\right)_1 x^2 + \left(\frac{1}{n^2}\right)_2 y^2 + \left(\frac{1}{n^2}\right)_3 z^2 + \left(\frac{1}{n^2}\right)_4 yz + \left(\frac{1}{n^2}\right)_5 xz + \left(\frac{1}{n^2}\right)_6 xy = 1. \tag{4.9}$$

The coefficients $\left(\frac{1}{n^2}\right)_i$ define the optical indicatrix in the new coordinate system, and they can be stated in terms of the coefficients ϵ_{XX}, ϵ_{YY} and ϵ_{ZZ} by means of ordinary coordinate transformation rules.

By following the steps outlined in Born and Wolf [60], the index ellipsoid may be used to accurately represent the optical characteristics of an anisotropic material. The optical indicatrix is changed when the medium is applied to an electric field, either static or low-frequency. It is straightforward to characterize this modification in terms of the impermeability tensor η_{ij}, which is defined by the relation

$$E_i = \frac{1}{\epsilon_0} \sum_j \eta_{ij} D_j. \tag{4.10}$$

Equation 4.10 is the inverse relation of Equation 4.2, thus $\eta_{ij} = (\epsilon^{-1})_{ij}$. Expressing the optical indicatrix in terms of the elements of the impermeability tensor (η_{ij}) by noting that the energy density $U = (1/2\epsilon_0) \sum_{ij} \eta_{ij} D_i D_j$, and defining coordinates $x = D_x/(2\epsilon_0 U)^{1/2}$, $y = D_y/(2\epsilon_0 U)^{1/2}$, and $z = D_z/(2\epsilon_0 U)^{1/2}$ respectively, the expression for U as a function of D becomes:

$$\eta_{11}x^2 + \eta_{22}y^2 + \eta_{33}z^2 + \eta_{12}xy + \eta_{23}yz + \eta_{13}xz = 1. \tag{4.11}$$

Comparing Equation 4.11 and Equation 4.9, it gives,

$$\left(\frac{1}{n^2}\right)_1 = \eta_{11}, \left(\frac{1}{n^2}\right)_2 = \eta_{22}, \left(\frac{1}{n^2}\right)_3 = \eta_{33}, \left(\frac{1}{n^2}\right)_4 = \eta_{23} = \eta_{32},$$

$$\left(\frac{1}{n^2}\right)_5 = \eta_{13} = \eta_{31}, \left(\frac{1}{n^2}\right)_6 = \eta_{12} = \eta_{21}. \tag{4.12}$$

Next, suppose that η_{ij} may be written as a power series in the magnitude of the applied electric field's components, E_k, as

$$\eta_{ij} = \eta_{ij}^{(0)} + \sum_k r_{ijk}E_k + \sum_{kl} s_{ijkl}E_k E_l + \cdots. \tag{4.13}$$

Here, the linear electro-optic effect is represented by the tensor r_{ijk}, the quadratic electro-optic effect by the tensor s_{ijkl}, etc. The electro-optic tensor r_{ijk} must be symmetric in its first two indices because the dielectric permeability tensor η_{ij} is real and symmetric. The third-rank tensor r_{ijk} is typically represented as a two-dimensional matrix, r_{hk} using contracted notation. The lowest-order modification of the optical constants $(\frac{1}{n^2})_i$ in formula (4.9) for the optical indicatrix may be written as

$$\Delta(\frac{1}{n^2})_i = \sum_j r_{ij}E_j. \tag{4.14}$$

For nonlinear samples, where the Kerr effect is significant, the index ellipsoid will include s_{ijkl} terms from Equation 4.13. since the dielectric permeability tensor ϵ_{ij} is real and symmetric, the same is true for η_{ij}, which is also real and has symmetry. Thus s_{ijkl}'s four indices can be reduced to two. To reduce the number of randomly assigned symbols, the two new indices will be called i and j, even though they are technically different from the old i and j.

$$s_{ijkl} \rightarrow s_{ij} \tag{4.15}$$

For this to work, the term $E_k E_l$ must also be contracted in the same way. $E_k E_l$ can also written as a 3×3 matrix. This matrix is symmetric, so it can be shrunk down to a 1×6 matrix that shares an index with the new s_{ij} matrix. This will produce

$$E_{kl} = E_k E_l \rightarrow \xi_j, \tag{4.16}$$

where the first three terms of ξ_j are E_k^2 with k runs from 1 to 3, while the final three terms are $2E_1 E_2$, $2E_1 E_3$, and $2E_2 E_3$. The additional factor of two in the last three terms is a result of cross-terms in the index ellipsoid. For simplify, the cross terms are defined by ξ_{kl}.

For a sample that is isotropic in the absence of an external electric field, the index of refraction is not dependent on the optical axis or the polarization of the light, and it has the same index of refraction in all three Cartesian coordinate directions. For this case, the index ellipsoid is given by the equation

$$\frac{X^2}{n^2} + \frac{Y^2}{n^2} + \frac{Z^2}{n^2} = 1. \tag{4.17}$$

where (X, Y, Z) is the principal-axis coordinate system without an electric field. If a medium is subjected to an electric field, the index ellipsoid will change according to the Equations 4.14 and will take on the form

$$\frac{X^2}{n^2} + \frac{Y^2}{n^2} + \frac{Z^2}{n^2} + 2XZ(s_{4j}\xi_j) + 2YZ(s_{5j}\xi_j) + 2XY(s_{6j}\xi_j) = 1. \tag{4.18}$$

When an electric field is applied to the medium, it is important to keep in mind that the coordinate system consisting of X, Y, and Z is not the principal-axis coordinate system. This is because the equation has cross terms that include YZ, XZ, and XY.

Let us suppose that the applied electric field has just a y component, so reducing the above equation to

$$\frac{X^2}{n^2} + \frac{Y^2}{n^2} + \frac{Z^2}{n^2} + 2XY(s_{42}\xi_y) = 1. \tag{4.19}$$

This unique situation occurs often in device implementations. It is now possible to visually locate the new principal-axis coordinate system, which we label (x, y, z). If we let

$$X = \frac{x - y}{\sqrt{2}}, \qquad\qquad Y = \frac{x + y}{\sqrt{2}}, \qquad\qquad Z = z \tag{4.20}$$

Equation 4.19 becomes

$$(\frac{1}{n^2} + s_{42}\xi_y)x^2 + (\frac{1}{n^2} - s_{42}\xi_y)y^2 + \frac{z^2}{n^2} = 1. \tag{4.21}$$

In its principal-axis system, it defines an ellipsoid. This might also be written as

$$\frac{x^2}{n_x^2} + \frac{y^2}{n_y^2} + \frac{z^2}{n_z^2} = 1. \tag{4.22}$$

where the new primary values of the refractive index at the physically plausible limit of $s_{42}\xi_y \ll 1$ are provided by

$$n_x = n - \frac{1}{2}n^3 s_{42}\xi_y \tag{4.23}$$

$$n_y = n + \frac{1}{2}n^3 s_{42}\xi_y \tag{4.24}$$

Thus, using $\xi_y = E_y^2$,

$$\Delta n = \mid n_x - n_y \mid = n^3 s_{42} E_y^2. \tag{4.25}$$

Equation 4.25 shows the relationship $\Delta n \propto E^2$. The Kerr constant (K) is a convenient way to aggregate all of the potential (and usually unknown) contributions from the constituents of s components.

$$\Delta n = KE^2 \tag{4.26}$$

Figure 4.2 depicts the curve produced by the intersection of the plane perpendicular to the propagation direction (i.e., the plane z = Z = 0) and the index ellipsoid. In the absence of a static field, the curve has the shape of a circle, indicating that the refractive index has the value n_0 for all polarization directions. This curve has the shape of an ellipse in the situation when a field is applied.

If a light beam travels through a modulator medium in the $z = Z$ direction, then a wave polarized in the x-direction will have a different velocity than a wave polarized in the y-direction. As the two polarization components move through the modulator medium for a length of L, they will accumulate a phase difference. The phase difference, known as the retardation, is

$$\Gamma = \frac{2\pi}{\lambda} \mid n_x - n_y \mid L. \tag{4.27}$$

28
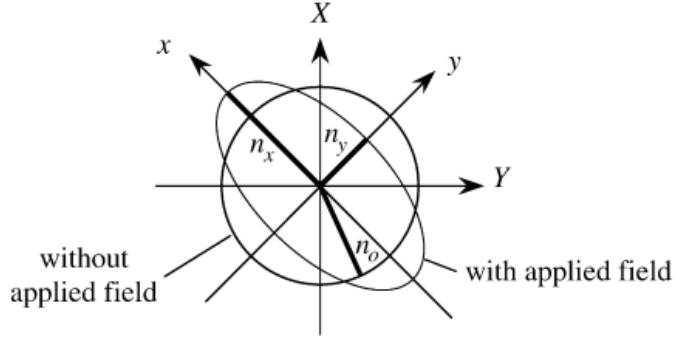
Figure 4.2: The intersection of the index ellipsoid with the plane z = Z = 0 in the presence and absence of applied electric field [8].

Equation 4.27 applies to any linear birefringence phenomenon that yields various indices of refraction for different linear polarization states of light. When the two principal axes that produce the effect are plane polarized at an angle of $\pi/4$, the strength of the effect is greatest. When maximized, the relation between ellipticity and Γ is

$$\epsilon = \frac{\Gamma}{2}. \tag{4.28}$$

From Equations 4.26, 4.27, and 4.28, the ellipticity is

$$\epsilon = \frac{\pi}{\lambda} K E^2 L. \tag{4.29}$$

This method is used as a strategy for keeping track of changes in the strength of the net electric field in a target area. Although this approach may appear excessive, the very low temperatures at which liquid nitrogen and superfluid helium are found make it necessary to use this method.

4.2 The Interaction Between Two Non-Polar Molecules

Understanding the molecular interaction is highly crucial if one wishes to have any prospect of comprehending the binding energy of ions on the surfaces of plastics. In our experimental setup, a cesium-137 source was utilized to ionize the liquid nitrogen. The source had a high activity level of around 28 mCi during the data collection process and was contained within a Berthold model LB 744014 lead shield container. The ionizing radiation from the source was able to escape through a narrow, 9-cm long collimating channel with a diameter of approximately 2 cm. The cesium-137 isotope underwent decay with 662 keV γ rays and 514 keV β particles. A Geant4 simulation demonstrated that only the gamma radiation was able to reach the central fiducial volume, which is the volume situated between the PMMA plates [61]. The gamma radiation possessed enough energy to ionize the liquid nitrogen, generating N_2^+ ions and electrons. Due to the small volume of liquid nitrogen, it is less likely

for a gamma ray to interact with it in such a way as to ionize to produce N_2^{++} ions. Consequently, solely nitrogen ions (N_2^+) and electrons exist in our specific scenario.

N_2^+ ions are non-polar molecules and do not have a permanent dipole moment. In the presence of an electric field, the electrons in the N_2^+ ions will experience a force. However, this force will not be sufficient to create a permanent dipole moment, as the electrons will not be redistributed in a way that creates a net dipole moment. As a result, N_2^+ ions will not be affected by an electric field to the same degree as polar molecules. Thus, N_2^+ ions can experience a temporary dipole moment, known as an induced dipole. The induced dipole moment of N_2^+ ions in an electric field is expected to be relatively small. It is worth noting that, while N_2^+ ions are not polar molecules, they may still be influenced by an electric field through ionic drift.

PMMA is a non-polar polymer that lacks a permanent dipole moment. Nonetheless, when an electric field is present, PMMA can develop an induced dipole moment. When PMMA is placed in an electric field, the electrons in the polymer will experience a force due to the electric field. This force can cause a redistribution of electrons within the polymer, creating a temporary dipole moment. The strength of the induced dipole moment is directly proportional to the strength of the electric field and the polarizability of the PMMA. However, the polarizability of PMMA is relatively small, so the induced dipole moment is small.

since for our purposes we only have non-polar molecules, only the interaction between two non-polar molecules is covered in this section. Principally, London dispersion forces, also known as van der Waals forces (vdW), govern the interaction between two non-polar molecules. These forces are the consequence of the transient dipoles created by the random motion of electrons in non-polar molecules. As the electrons in one molecule travel, they generate a temporary dipole that may then interact with the temporary dipoles of adjacent molecules. The binding energy of ions on the surface of PMMA can depend on a variety of factors, such as the charge state and size of the ion, the temperature and humidity, the chemical nature of the surface, etc. However, as PMMA is a non-polar polymer, the binding energy of ions on its surface is generally relatively low and is usually dominated by London dispersion forces.
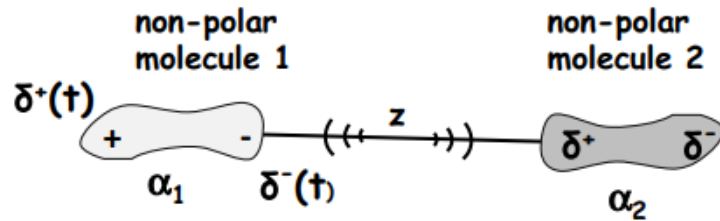
Figure 4.3: The interaction of two non-polar molecules separated by distance z. At some instant in time with the application of E-field, the oscillating mass in molecule gets dislocated away from the fixed mass inducing dipole moment with the separation of $\delta^+(t)$ and $\delta^-(t)$ [9].

For dissimilar atoms or molecules having ionization energies I_1, I_2 and polariz-

abilities α_1 and α_2 interacting with each other in a medium with a uniform dielectric constant κ, the strength of interaction between two non-polar molecules, also called the London dispersion relation, can be represented by the following equation: [62]

$$U_{vdW}^{London}(z) = -\frac{3}{2}\frac{\alpha_1\alpha_2}{(4\pi\kappa\epsilon_0)^2}\frac{I_1 I_2}{I_1 + I_2}\frac{1}{z^6}. \tag{4.30}$$

Theoretically, this gives the binding energy of ions on surfaces. Generally, the binding energy can be measured using techniques such as X-ray photoelectron spectroscopy (XPS) or Secondary Ion Mass Spectrometry (SIMS). However, in this instance, we are using Kerr effect measurement to determine the binding energy of ions on PMMA surfaces inside the cryogenic liquid. The approach we are utilizing to determine the binding energy inside cryogenic liquid is completely novel.

4.2.1 Electrostatic Desorption

In this work, we demonstrate the removal of ions and/or electrons from a surface by reversing electric fields. It is based on the idea that when a voltage is provided in the opposite direction from where the ions were adsorbed, they will be expelled from the surface, and is known as electrostatic desorption. Electrostatic desorption is often accomplished by applying a high voltage to the surface, which generates an electric field powerful enough to dislodge the forces binding the ions to the surface. After being desorbed, the ions recombine and get neutralized. The analysis of adsorbed ions on the surface can be done using this approach, which is mostly utilized in mass spectrometry and is thought to be a non-destructive procedure. It is important to keep in mind that the nature of the surface, the type of ions adsorbed, and the experimental setup all play a significant role in how successfully electrostatic desorption occurs.

The electrostatic desorption force can be calculated using Coulomb's law, which states that the force between two charges is proportional to the product of the charges and inversely proportional to the square of the distance between them. In the case of electrostatic desorption, the force acting on the adsorbed ion is the force of the electric field acting on the ion's charge.

The equation for calculating the electrostatic desorption force is

$$\vec{F} = q\vec{E}, \tag{4.31}$$

where $\vec{F}$ is the force of the electric field acting on the ion's charge, q is the charge of the ion, and $\vec{E}$ is the strength of the electric field.

Alternatively, the electrostatic force can be calculated as

$$\vec{F} = -\nabla U, \tag{4.32}$$

where U is the electrostatic potential energy and ∇ is the gradient operator. It is important to note that the electrostatic desorption force is not the only force acting on the adsorbed ion; here van der Waals forces can play a significant role in the process of desorption. The magnitude of the electrostatic desorption force can also

be affected by the distance between the ion and the surface, the dielectric constant of the medium, and the ion's polarizability.

Considering only the London dispersion relation as an attractive interaction between two molecules, the van der Waals potential is given by,

$$U_{vdW}(z) = -\frac{A}{z^6} + \frac{B}{z^{12}}, \tag{4.33}$$

where $A = \frac{3}{2}\frac{\alpha_1\alpha_2}{(4\pi\epsilon_0)^2}\frac{I_1 I_2}{I_1+I_2}$, $B = A(\frac{\alpha_1\alpha_2}{(4\pi\epsilon_0)^2})^{1/6}$, and z is the distance of separation between both molecules. The binding energy between two molecules can be estimated with the known values of A and B. With the known values of polarizability of N_2^+, $\alpha_0(N_2^+) =$
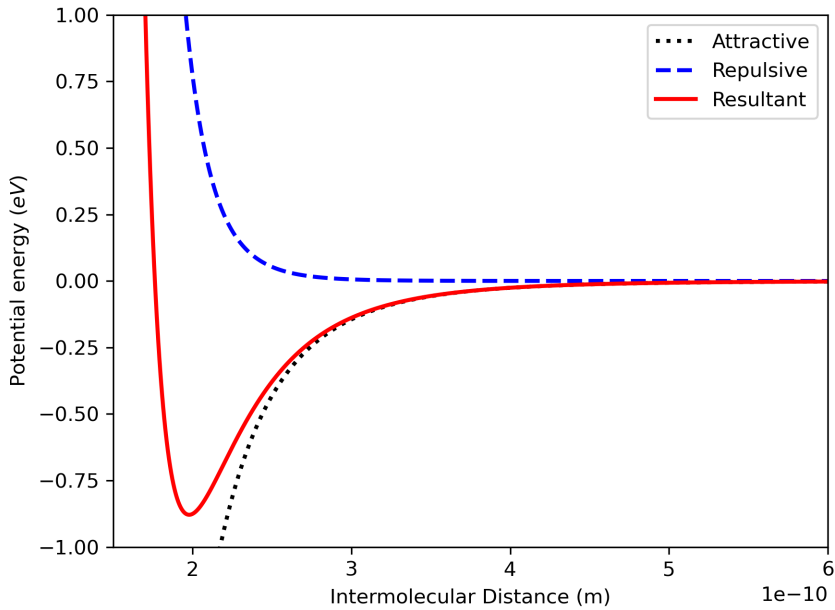
Figure 4.4: The van der Waals interaction of an N_2^+ molecule on the PMMA surface as a function of distance The blue dotted line is the repulsive potential, the black line is the attractive potential, and the solid red line is the resultant of the attractive and repulsive potentials.

$\frac{\alpha_1}{4\pi\epsilon_0} = 1.07 \times 10^{-30} m^3$ [63], polarizability of PMMA $\alpha_0(\text{PMMA}) = \frac{\alpha_2}{4\pi\epsilon_0} = 2.80 \times 10^{-29} m^3$ [64], ionization energies $I_1(N_2^+) = 15.58$ eV [65], $I_2(PMMA) = 7.21$ eV [64], the values of A and B are calculated. With these known A and B values, plotting the Equation 4.33 gives the plot shown in Figure 4.4.

It shows two 'parts': a repulsive term and an attractive term. The attractive component arises from the van der Waals forces between the molecules, while the repulsive component arises when two molecules come too close to each other, the electrons in the outermost orbitals of the molecules will repel each other due to their negative charges. It is also called the "Lennard-Jones potential curve". The Lennard-Jones potential curve has the shape of a "double-well" potential, with a minimum at a

distance called the equilibrium distance, where the attractive and repulsive forces are balanced. From the plot, this value is 1.98 Å and the corresponding energy is -0.88 eV, which is also the binding energy. As the particles move closer together than the equilibrium distance, the repulsive forces dominate, and the potential energy increases rapidly. Similarly, as the particles move further apart, the attractive forces weaken, and the potential energy decreases slowly. Thus, the estimated binding energy of N_2^+ molecule on the PMMA surface is -0.88 eV.

Chapter 5 Measuring Kerr Rotation

The most popular methods for measuring the optical rotation of linearly polarized light include combining polarizers and wave plates to detect variations in intensity. There are various methods for assessing the polarization state of light. The techniques for measuring Kerr rotation in this study are described in this chapter. The main focus of the discussion will be on a triple modulation method for accurate measurements of Kerr rotation angles and different system calibrations.

5.1 Optical Setup
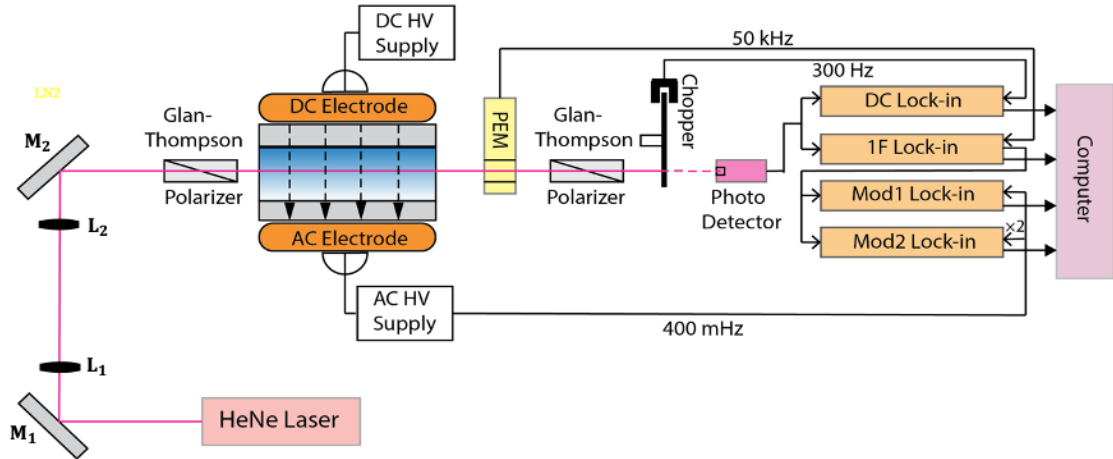
Figure 5.1: The schematic diagram of the optical set-up for measurement of the electro-optic Kerr effect.

Figure 5.1 depicts the passage of a low-power helium-neon laser beam (HRS015 from Thorlabs) through a cryostat and several optical components. The laser beam has a wavelength of 632.8 nm and a power of < 5 mW in the intensity-stabilized mode. The laser passes through steering optics, a polarization stage, a sample, and analyzer optics. The beam is well-collimated, and it travels through the cryogenic system using two alignment mirrors (M_1 and M_2), and two focusing convex lenses (L_1 and L_2). The light is linearly polarized before entering the cryostat using a Glan-Thompson polarizer. The laser beam's polarization changes as it passes through the cryogenic medium, which is exposed to a horizontal electric field, inducing an ellipticity that is proportional to the square of the electric field due to the electro-optical Kerr effect. After that, a photoelastic modulator (PEM, Hinds PEM 100) and an additional Glan-Thompson prism are used to measure the polarization of the light. Finally, the light is detected by a photodetector (Hinds DET-100-002).

To achieve maximum sensitivity in the system, careful laser beam alignment and ellipsometry setup are necessary. In particular, since the laser beam has to pass through a narrow-width (~3 mm) and 3 cm long space between the PMMA plates, it is crucial to correctly collimate the beam to typical beam sizes of less than 1 mm (Figure 5.2). This is necessary to ensure that the beam does not scrape the PMMA plates as it passes through the electrode system. To achieve this, the transmitted power was measured as a function of the horizontal laser beam angle, and adjustments were made to reduce touching the walls to a minimum. Once this was achieved, the beam was positioned for maximum transmission. Figure 5.3 displays the transmitted power in μW as a function of the horizontal laser beam angle in arbitrary units (A.U.). The maximum transmitted power is around 300 μW, which is where the beam was optimally positioned.
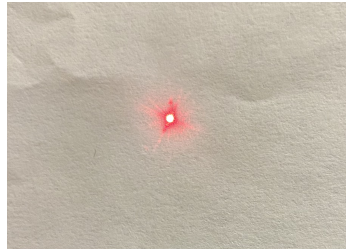
Figure 5.2: The picture of the collimated laser beam before entering the cryostat. The spot in the picture represents the laser beam size whose diameter is ~1 mm.
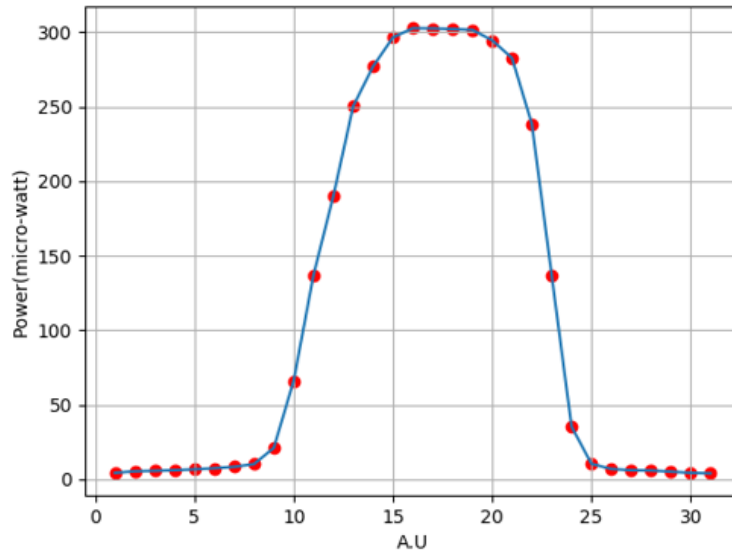
Figure 5.3: Transmission power of the laser beam through the PMMA plates electrode system with the horizontal laser beam angle. The adjustment is set when the transmission power is maximum.

To set up the ellipsometry, the initial laser beam was polarized at an angle of $\theta_p = \pi/4$ with respect to the direction of the electric field, the angle of the PEM

was set to $\theta_{PEM} = \pi/4$, and the second Glan-Thompson prism was set to $\theta_a = 0$, i.e. along the horizontal direction. These specific parameters were chosen to achieve a decent signal-to-noise ratio and a distinct signal for this experiment. A Thorlabs PAX1000IR1(/M): 600–1080 nm polarimeter was used to measure the polarization state. This allows for measuring the optical rotation of the sample, displaying the measurement results, and calibrating the polarimeter, which involves adjusting the instrument to ensure accurate measurements.

The software GUI for the PAX1000 series polarimeter shows equally-sized polarization stage and Poincaré sphere measurement windows after the Glan-Thompson polarizer, photo-elastic modulator, and Glan-Thompson analyzer respectively. These measurement windows are depicted in Figures 5.4, Figure 5.5, and Figure 5.6.

A Poincaré sphere (gray sphere) measurement window is a graphical representation of the polarization state of light. The Poincaré sphere is a three-dimensional sphere that can be used to represent the polarization state of light in terms of its ellipticity, orientation, and degree of polarization. The measurement window typically displays the Poincaré sphere and allows the user to adjust the polarization state of incident light using a polarization stage while observing the changes in the sphere.
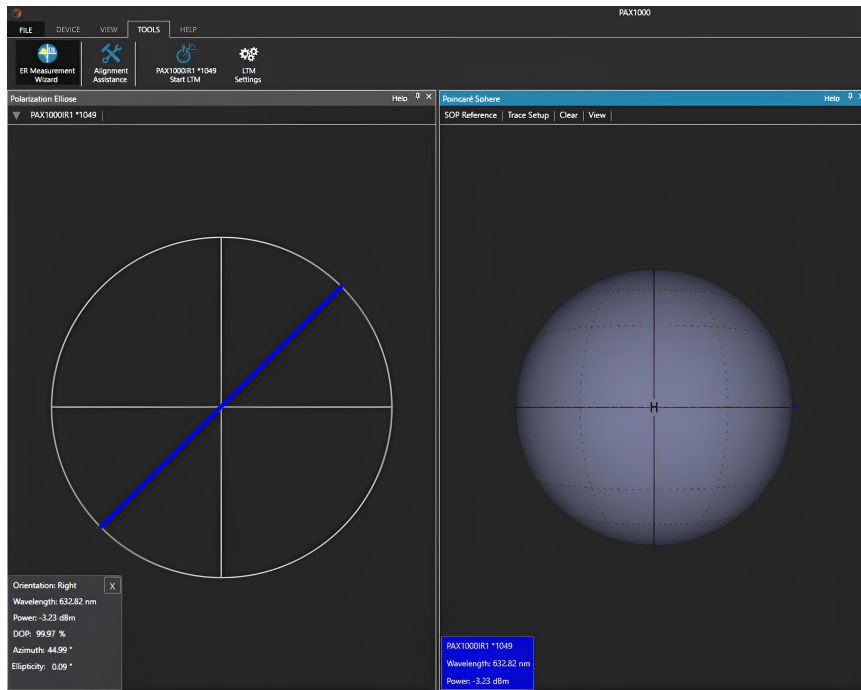
Figure 5.4: The polarization stage and the Poincaré sphere of light after it has passed through the first Glen-Thompson Polarizer (before cryostat).

In the study of light polarization, the elliptical and rotational components of the polarization state are represented by distinct harmonics of the frequency of PEM modulation. In this configuration, the first harmonic of the PEM ($f = 50$ kHz) corresponds to the ellipticity. The laser beam was modulated using an optical chopper at a frequency of around 300 Hz, and a separate lock-in amplifier, labeled "DC Lock-in" in Figure 5.1, was used to monitor the laser intensity. This modification eliminated
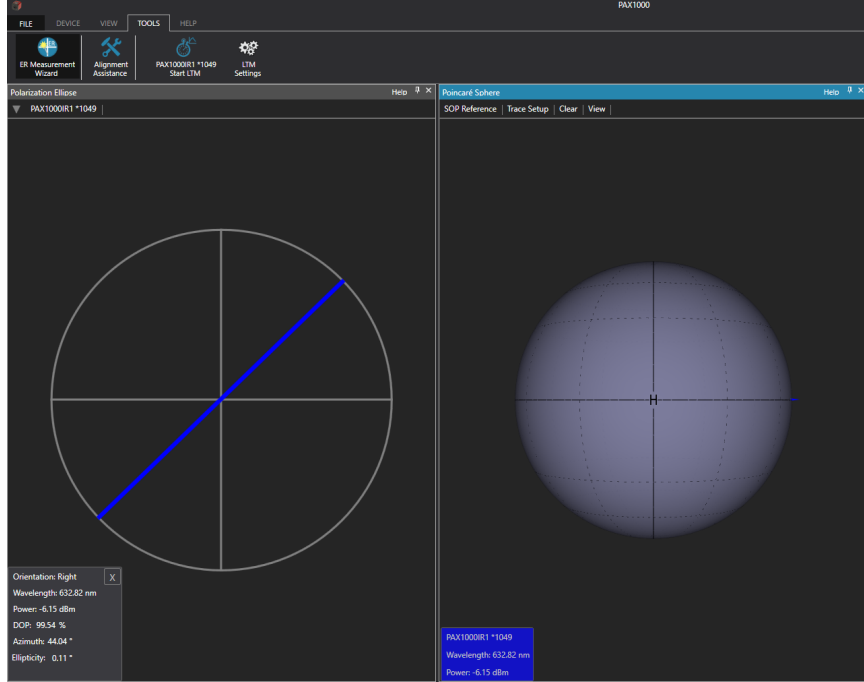
Figure 5.5: The polarization stage and the Poincaré sphere of light after it has passed through the photoelastic modulator (PEM).

any systematic effects caused by residual laser intensity drifts. since the expected signals from the electro-optic Kerr effect are small, the applied electric field was also modulated at a low frequency, typically about 400 mHz [[7], [66], [67]]. The applied modulation frequency is low since a higher modulation frequency would result in significant signal distortions due to RC effects. This low modulation helps to improve the signal-to-noise ratio of the measurements and makes it easier to detect the small changes in polarization induced by the electric field. DC and AC components were present in the time-dependent field. The two electrodes create an electric field in which the sample is placed. One electrode is kept at a constant positive voltage (DC), while the other is AC modulated with some DC offset at values that stay negative. Because of this, the induced electric field has the following shape:

$$E(t) = \frac{V_{DC}}{d} + \frac{V_{AC}\cos(\omega t)}{d}. \tag{5.1}$$

In equation 5.1, V_{DC} represents the DC offset of the potential difference between the electrodes, V_{AC} represents the amplitude of the AC component of the potential difference between the electrodes, d represents the distance between the two electrodes, ω represents the angular frequency at which the AC supply is modulated, and t represents the elapsed amount of time. The induced Kerr effect in the system is proportional to the square of the electric field, which is a combination of the DC and AC components of the applied potential difference. Therefore, the induced Kerr effect given by Equation 4.29 becomes,

$$\epsilon(t) = \frac{\pi}{\lambda}K(\frac{V_{DC}^2}{d^2} + \frac{V_{AC}^2}{2d^2} + \frac{2V_{DC}V_{AC}}{d^2}\cos(\omega t) + \frac{V_{AC}^2}{2d^2}\cos(2\omega t))L. \tag{5.2}$$

37
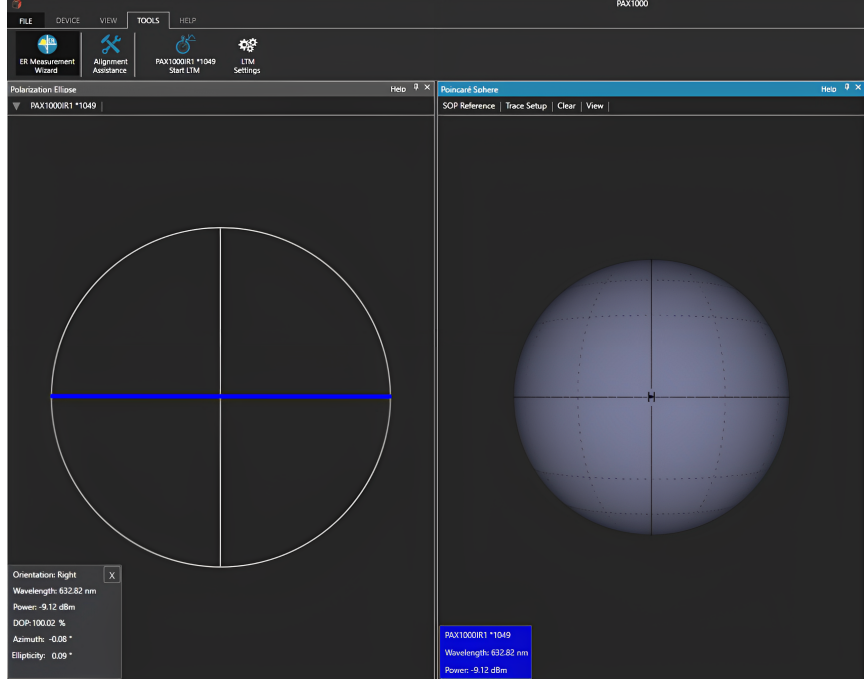
Figure 5.6: The polarization stage and the Poincaré sphere of light after it has passed through the second Glen-Thompson Polarizer (after cryostat).

Equation 5.2 describes the induced Kerr effect in the system, which consists of two oscillating terms: the first harmonic term and the second harmonic term. The first harmonic term is proportional to the product of V_{DC} and V_{AC} and the second harmonic term is proportional to V_{AC}^2. The L is taken into account along the entire laser path where the electric field is non-zero. This means that the L must take into account any fringe effects that may occur due to the interference of the laser beam with the electric field. These fringe effects can lead to variations in the electric field intensity along the laser path, which can in turn affect the induced ellipticity of the light. Therefore, it is important to carefully consider the length L and any potential fringe effects in order to accurately calculate the induced Kerr effect. The two harmonic terms can be expressed as follows: First harmonic term:

$$\epsilon_1(t) = \frac{\pi}{\lambda} K \frac{2V_{DC}V_{AC}}{d^2} \cos(\omega t)L, \tag{5.3}$$

Second harmonic term:

$$\epsilon_2(t) = \frac{\pi}{\lambda} K \frac{V_{AC}^2}{2d^2} \cos(2\omega t)L. \tag{5.4}$$

The first harmonic term depends on both the DC and AC components of the applied potential difference, while the second harmonic term only depends on the AC component.

To isolate the contributions of the induced Kerr effect, the experimental setup included two lock-in amplifiers labeled "MOD1 Lock-in" and "MOD2 Lock-in" in Figure 5.1. The first harmonic cross term, which is proportional to the product

of V_{DC} and V_{AC}, is sensitive to any cell charging due to ionization, which would lower the DC component of the electric field over time. The second harmonic term, which is proportional to V_{AC}^2, is used to monitor the stability of the AC amplitude. The sensitivity of the second harmonic term is four times lower than that of the first harmonic cross term. Thus, the second harmonic term has a lower signal-to-noise ratio than the first harmonic term. As the first harmonic term is of interest, the second harmonic term was only measured to monitor the stability of the AC components while taking data.

5.2 Kerr Signal Measurement with a Triple Modulation Method

Three sources of deliberate signal modulation are present, as shown in the preceding section. Modulating these parameters permits the detection of small signals in a noisy environment with a huge background. The first source is the optical chopper, which helps to eliminate ambient light-induced noise and provides a more stable intensity measurement for the laser. The second source is an electric field applied to the sample. Modulating this permits accurate measurements of tiny signals in noisy backgrounds. Lock-in amplifiers capture these signals by using phase-locking methods and very narrow bandpass filters to reject any backgrounds that are not within a restricted bandwidth around a particular frequency, drastically lowering the amount of background noise that might interfere with the signal. The last modulation is the PEM, which is a birefringent fused silica crystal oscillating at 50 kHz to convert a polarization into an intensity of the probe beam; the final light intensity in the detector is dependent on the PEM frequency and its harmonics [[67], [66]]. The 50 kHz PEM is used in ellipsometry experiments because it provides a high signal-to-noise ratio for the lock-in detection method. The lock-in method is a sensitive technique that can detect small changes in the polarization of light, and it requires a modulated signal to provide a reference for detection.

The photoelastic modulator is a device used to modulate the polarization state of light in optical systems. It is made up of a birefringent crystal that changes its birefringence in response to an electrical field applied by a piezoelectric transducer. The frequency of modulation is determined by the frequency of the electrical field and the modulated frequency of our PEM is 50 kHz. This modulation of polarization can be used to measure the anisotropic properties of a sample by analyzing the change in polarization of light after it passes through the sample. The device is commonly used in optical spectroscopy and ellipsometry experiments. The PEM modulates the probe light's polarization by altering the index of refraction for polarization components perpendicular and parallel to the axis of the crystal, which dynamically changes the polarization of the light through all states of polarization at the frequency of the applied voltage. The device's optical retardation is stated as

$$\delta_{PEM}(\lambda, t) = A \sin(\omega_p t) + \delta_0(\lambda), \tag{5.5}$$

where A represents the peak strain amplitude of the photo-elastic modulator (PEM), and ω_p is the modulated frequency of the PEM. Additionally, δ_0 represents a small

correction factor that accounts for any residual static strain present in the PEM. When developing these optical components, typically only materials with a small δ_0 are used, and manufacturers account for it. This permits disregarding the term δ_0. The Jones matrix formalism can be used to explain the effects of the PEM on the polarization state of light, and it provides an accurate and convenient tool to predict the output polarization state of modulated light. If the optically anisotropic sample has different reflection coefficients for the x and y axes, then the Jones matrix formalism describes a PEM with stress on the y-axis [7] as follows:

$$M_{PEM} = \begin{bmatrix} 1 & 0 \\ 0 & e^{i\delta} \end{bmatrix}. \tag{5.6}$$

since the element $e^{i\delta}$ in the Jones matrix is expressed as

$$e^{i\delta} = \cos\delta + i\sin\delta = \cos[A\sin(\omega_p t)] + i\sin[A\sin(\omega_p t)], \tag{5.7}$$

the two terms can be expanded using a series of Bessel functions. This yields

$$\cos[A\sin(\omega_p t)] = J_0(A) + 2\sum_{j=1}^{\infty} J_{2j}(A)\sin[2j\omega_p t], \tag{5.8}$$

and

$$\sin[A\sin(\omega_p t)] = 2\sum_{j=1}^{\infty} J_{2j-1}(A)\sin[(2j-1)\omega_p t]. \tag{5.9}$$

The integer Bessel functions are based on the Bessel angle A, which is measured in radians and is related to the size of the modulation and, usually, the drive voltage. If the drive voltage is set so that $A_0 = 2.4048$, then $J_0(A_0) \sim 0$, and the DC term in Equation 5.8 vanishes, simplifying the analysis. Also, the first two integer Bessel functions are close to their maximums for this value of A, and the higher-order integer Bessel functions are getting closer and closer to zero.

If the PEM is then rotated around the axis of incidence by some angle, in our case $\pi/4$, then the Jones matrix may likewise be rotated using the Jones calculus in order to accurately characterize the new location,

$$M_{PEM} = \begin{bmatrix} \cos(\pi/4) & \sin(\pi/4) \\ -\sin(\pi/4) & \cos(\pi/4) \end{bmatrix} \begin{bmatrix} 1 & 0 \\ 0 & e^{i\delta} \end{bmatrix} \begin{bmatrix} \cos(\pi/4) & -\sin(\pi/4) \\ \sin(\pi/4) & \cos(\pi/4) \end{bmatrix}. \tag{5.10}$$

This gives,

$$M_{PEM} = \frac{1}{2} \begin{bmatrix} 1+e^{i\delta} & -1+e^{i\delta} \\ -1+e^{i\delta} & 1+e^{i\delta} \end{bmatrix} \tag{5.11}$$

A similar manner of representation may be achieved by using Jones matrices for the Kerr effect [68],

$$M_{sample} = \begin{bmatrix} 1 & 0 \\ 0 & e^{i\Gamma} \end{bmatrix}. \tag{5.12}$$

For maximum Kerr effect in the medium, the rotation of the polarizer and analyzer with angle $\pi/4$ and $\pi/2$ are required. Thus, the Jones matrices for the polarizer and analyzer are

$$M_{polarizer,\pi/4} = \frac{1}{2}\begin{bmatrix} 1 & 1 \\ 1 & 1 \end{bmatrix} \tag{5.13}$$

$$M_{analyzer,\pi/2} = \begin{bmatrix} 1 & 0 \\ 0 & 0 \end{bmatrix}. \tag{5.14}$$

Calculating the ultimate state of the electric field of the laser, denoted by $\vec{E}_f$, in terms of its beginning field, denoted by $\vec{E}_0$, is possible by using Equations 5.11 and 5.12 in conjunction with the matrices for linear polarizers [59] with Equations 5.13 and 5.14. Define $\hat{z}$ as the axis of propagation and $\hat{y}$ as the direction of the electric field that is being applied externally, and for the sake of ease, begin with light that is linearly polarized in alignment with the polarizing Glan-Thompson. Using Jones matrices, the final electric field of a laser passing through a sample along with different optical elements generates a Kerr rotation, which is given by,

$$\vec{E}_f = M_{analyzer,\pi/2}.M_{PEM}.M_{sample}.M_{polarizer,\pi/4}.\vec{E}_0. \tag{5.15}$$

since the initial laser beam is linearly polarized by an angle of $\pi/4$ with the electric field, so,

$$\vec{E}_0 = \frac{E_0}{\sqrt{2}}\begin{bmatrix} 1 \\ 1 \end{bmatrix}. \tag{5.16}$$

Plugging the value of Equations 5.11, 5.12, 5.13, 5.14, and 5.16 in Equation 5.15,the obtained equation will be,

$$\vec{E}_f = \begin{bmatrix} 1 & 0 \\ 0 & 0 \end{bmatrix}\frac{1}{2}\begin{bmatrix} 1+e^{i\delta} & -1+e^{i\delta} \\ -1+e^{i\delta} & 1+e^{i\delta} \end{bmatrix}\begin{bmatrix} 1 & 0 \\ 0 & e^{i\Gamma} \end{bmatrix}\frac{1}{2}\begin{bmatrix} 1 & 1 \\ 1 & 1 \end{bmatrix}\frac{E_0}{\sqrt{2}}\begin{bmatrix} 1 \\ 1 \end{bmatrix}. \tag{5.17}$$

This gives

$$\vec{E}_f = \frac{E_0}{2\sqrt{2}}\begin{bmatrix} (e^{i\delta}+1)+e^{i\Gamma}(e^{i\delta}-1) \\ 0 \end{bmatrix}. \tag{5.18}$$

since the electric field is not directly measured in most laser experiments, and instead, the intensity of the light is measured. The normalized relation between intensity and the electric field is given by,

$$\frac{I_f}{I_0} = \frac{\vec{E}_f^{+}\vec{E}_f}{\vec{E}_0^{+}\vec{E}_0}. \tag{5.19}$$

Here, $\vec{E}_f^{+}$ and $\vec{E}_0^{+}$ are the complex conjugates of $\vec{E}_f$ and $\vec{E}_0$ respectively. When the values from Equations 5.18 and 5.16 are substituted into Equation 5.19, the resulting equation is solved as follows

$$\frac{I_f}{I_0} = \frac{1}{2}[1 - \sin\delta\sin\Gamma], \tag{5.20}$$

41

where $\sin\delta$ reflects the influence of the PEM on the system and Γ conveys the Kerr effect. The value of $\Gamma \ll \delta$. Thus, $\sin\Gamma \approx \Gamma$. Now, the Equation 5.20 becomes,

$$\frac{I_f}{I_0} = \frac{1}{2}[1 - \Gamma\sin\delta]. \tag{5.21}$$

Inserting the value of $\sin\delta$ from Equation 5.9, the above Equation 5.21 becomes

$$\frac{I_f}{I_0} = \frac{1}{2}[1 - \Gamma(2J_1(A)\sin(\omega_p t) + 2J_3(A)\sin(3\omega_p t) + ...)]. \tag{5.22}$$

As a result, the photodiode's ability to detect light is determined by a sum of factors that are functions of the PEM resonant frequency of 50 kHz. The odd terms (J_1, J_3, etc.) of the series determine the Kerr rotation angle. It is possible to estimate the rotation angle by isolating the signal at the first harmonic of 50 kHz and utilizing lock-in amplifier techniques. Taking into account the first harmonic,

$$\frac{I_{1f}}{I_0} = \Gamma J_1(A). \tag{5.23}$$

The external electric field that passes through the sample, however, governs the value of Γ. The Kerr effect in the sample is driven by the 400 mHz electric field oscillation. Combining Equations 4.28 and 5.2, the following relationship is created:

$$\Gamma = 2\frac{\pi}{\lambda}K\left(\frac{V_{DC}^2}{d^2} + \frac{V_{AC}^2}{2d^2} + \frac{2V_{DC}V_{AC}}{d^2}\cos(\omega t) + \frac{V_{AC}^2}{2d^2}\cos(2\omega t)\right)L. \tag{5.24}$$

The cross-term oscillates with a sine wave and exhibits sensitivity to the DC high voltage (DC offset owing to the electric field). This is really important to the experiment that we are doing. This cross-term oscillates at the first harmonic of the field's frequency, which means that the output of the 1F lock-in amplifier (LIA) can be used as the input for another LIA (known as the Mod1 LIA). The mod1 LIA can be used to isolate a signal at the first harmonic of the reference frequency for the electric field. Thus, this process enables the accurate measurement of the electric field. Finally, the Mod1 LIA will measure an RMS voltage that is equivalent to the following intensity:

$$I_{mod1} = \frac{2\pi K J_1(A) I_0}{\lambda}\frac{2V_{DC}V_{AC}}{d^2}L. \tag{5.25}$$

If we define ϵ_1 as

$$\epsilon_1 = \frac{\pi K}{\lambda}\frac{2V_{DC}V_{AC}}{d^2}L, \tag{5.26}$$

the above equation 5.25 becomes,

$$I_{mod1} = 2J_1(A)\epsilon_1 I_0. \tag{5.27}$$

For the triple modulation technique, the photodetector is connected to four lock-in amplifiers, as shown in Figure 5.1. Each lock-in amplifier is set to one of the three modulation frequencies. The Mod1 and Mod2 LIAs are referenced by the same

electric field frequency of 400 mHz. The DC lock-in amplifier is linked to the optical chopper with a frequency of 300 Hz. As explained above, the 1F lock-in amplifier is driven by the photoelastic modulator at 50 kHz.

Thus, the DC LIA measures an RMS voltage of

$$I_{DC} = \frac{I_0}{2}. \tag{5.28}$$

Equation 5.28 is divided by two to account for the open-close profile of the optical chopper. Taking the ratio of equations 5.27 and 5.28

$$\frac{I_{mod1}}{I_{DC}} = 4J_1(A)\epsilon_1. \tag{5.29}$$

Here the value of $A = A_0 = 2.4048$.

With reference to the optical chopper, the DC lock-in amplifier calculates the beam's overall intensity. Because a lock-in amplifier monitors the input signal's V_{rms} value, the voltage of the lock-in amplifier must be multiplied by a factor of $\sqrt{2}$ to get the real voltage. Additionally, the DC signal displayed on the lock-in amplifier is impacted by the square wave signal of the optical chopper, requiring a Fourier decomposition of the signal. As a result, the 300 Hz lock-in amplifier rms signal displayed is multiplied by a factor of $2/\pi$, which affects the real DC signal [66]. Thus, the DC voltage is written as,

$$V_{DC}^{amp} = \sqrt{2}2\frac{\pi}{4}V_{DC}^{LIA}. \tag{5.30}$$

The second lock-in amplifier is a 1F or PEM lock-in, which is referenced to the PEM frequency of the first harmonic at 50 kHz. since the electric field is modulated, the voltage and rotation angle are proportional. Due to the fact that the PEM signal still contains this modulation, the demodulated voltage that the PEM lock-in amplifier shows will have a component that oscillates at the frequency of the electric field modulation. As a result, an analog output from the PEM lock-in amplifier, which is proportional to the voltage detected, is utilized as input to the Mod1 and Mod2 lock-in amplifiers. The Mod1 and Mod2 lock-in amplifiers are referenced to the frequency of the electric field modulation. The voltage signal generated by the rear output of the 1F lock-in amplifier (Model 7280 Wide Bandwidth DSP Lock-in Amplifier) is scaled as a percentage of 2.5 V, depending on the ratio of the front panel voltage value to the sensitivity setting. The final voltages from Mod1 and Mod2 lock-in amplifiers are

$$V_{Mod1}^{amp} = \frac{2\sqrt{2}\sqrt{2}}{2.5V}V_{sen}V_{Mod1}^{LIA}. \tag{5.31}$$

$$V_{Mod2}^{amp} = \frac{2\sqrt{2}\sqrt{2}}{2.5V}V_{sen}V_{Mod2}^{LIA}. \tag{5.32}$$

Here V_{sen} is the sensitivity applied for the 1F lock-in amplifier.
Taking the ratio of Equation 5.31 and 5.30

$$\frac{V_{Mod1}^{amp}}{V_{DC}^{amp}} = \frac{\sqrt{2}}{(2.5V)\pi}V_{sen}\frac{V_{Mod1}^{LIA}}{V_{DC}^{LIA}}. \tag{5.33}$$

Also, taking the ratio of Equation 5.32 and 5.30

$$\frac{V_{Mod2}^{amp}}{V_{DC}^{amp}} = \frac{\sqrt{2}}{(2.5V)\pi} V_{sen} \frac{V_{Mod2}^{LIA}}{V_{DC}^{LIA}}. \tag{5.34}$$

The ellipticity of first harmonic of the electric field is extracted using Equations 5.29 and 5.33 which gives

$$\epsilon_1 = \frac{\sqrt{2}V_{sen}}{(2.5V)\pi J_1(A)} \frac{V_{Mod1}^{LIA}}{V_{DC}^{LIA}}. \tag{5.35}$$

Experimentally, ϵ_1 is directly proportional to the ratio of Mod1 lock-in to the DC lock-in amplifier signals.

$$\epsilon_1 \propto \frac{V_{Mod1}^{LIA}}{V_{DC}^{LIA}}. \tag{5.36}$$

Similarly, the second harmonic of the electric field is extracted from Mod2 and DC lock-in amplifiers following the same method, which is given as

$$\epsilon_2 = \frac{\sqrt{2}V_{sen}}{(2.5V)\pi J_1(A)} \frac{V_{Mod2}^{LIA}}{V_{DC}^{LIA}}. \tag{5.37}$$

That is,

$$\epsilon_2 \propto \frac{V_{Mod2}^{LIA}}{V_{DC}^{LIA}}. \tag{5.38}$$

It is important to note that the inputs for the MOD1 and MOD2 lock-in amplifiers were obtained by routing the signal through the 1F lock-in amplifier from the detector. To ensure that the signal was not distorted, the integration time constant of the 1F lock-in amplifier had to be chosen to be short enough. This was not a problem since the PEM frequency was 50 kHz and the modulation frequencies for MOD1 and MOD2 were 400 mHz and 800 mHz, respectively. The time constant of the 1F lock-in was usually set at 20 μs.

Chapter 6 Experimental Setup

6.1 Cryogenic System

Both liquid nitrogen and liquid helium must be used for the measurements. For the use of liquid nitrogen, we need a setting that can maintain a temperature of 77 K or below during a prolonged measurement period. For liquid helium, it requires a setting that can support a temperature of 2.18 K or below for a number of hours during measurements.

6.1.1 The Cryostat

The observations in this research were carried out using a modified Janis Research SuperTran cryostat 380 (STVP-100), which was initially intended to use a continuous gas flow to cool small samples to 4.2 K. Figure 6.1 represents the schematic diagram of the cryostat in our lab. This cryostat consists of an outer vacuum chamber (OVC) with the radiation shield, an inner vacuum chamber (IVC), and a cooling mechanism. OVC minimizes heat transfer between the cryostat and the surrounding environment. The cooling mechanism, which is usually a refrigeration system, removes heat from the inner chamber and maintains the desired low temperature.

The inner chamber, which has the electrodes and the windows, was first cooled by sending liquid nitrogen through a transfer line from a dewar to the primary fill line of the cryostat. It normally takes around an hour to cool the system to 70 K. Right beneath the helium container, there is a level sensor. It is made up of two copper cylinders that are fixed on a plastic plate in a concentric fashion. As the low-pressure nitrogen gas is gradually replaced with liquid nitrogen, the copper cylinders act as a capacitor, which changes in capacitance. The capacitance reading in the vacuum was measured to be 64 pF, while the introduction of liquid nitrogen elevated the reading to 90 pF. The capacitance of the system was determined with a precision of 0.5 pF. However, it should be noted that a potential risk of exposing the high-voltage electrodes to arcing arises when the nitrogen level decreases, potentially leading to measurement disruptions. To mitigate this risk, an alert is implemented to notify the user of low nitrogen level, enabling early correction of excessive voltage before arcing occurs, and safeguarding the accuracy of the measurements. A heating block is situated directly beneath the level sensor, but it was not utilized during the filling of liquid nitrogen. This is a cylindrical copper disk that has a hole drilled through it so that a heater can be mounted inside of it. Additionally, the top of the block is equipped with a temperature diode. The PMMA cell and electrodes are located below that. The construction of the IVC, including the use of specific metals and a specialized mechanical structure, provides protection against conduction and convection caused by the low vacuum environment in which it is used. All of this contributes to reducing the amount of heat that is pumped into the cryogenic fluid in the inner chamber.
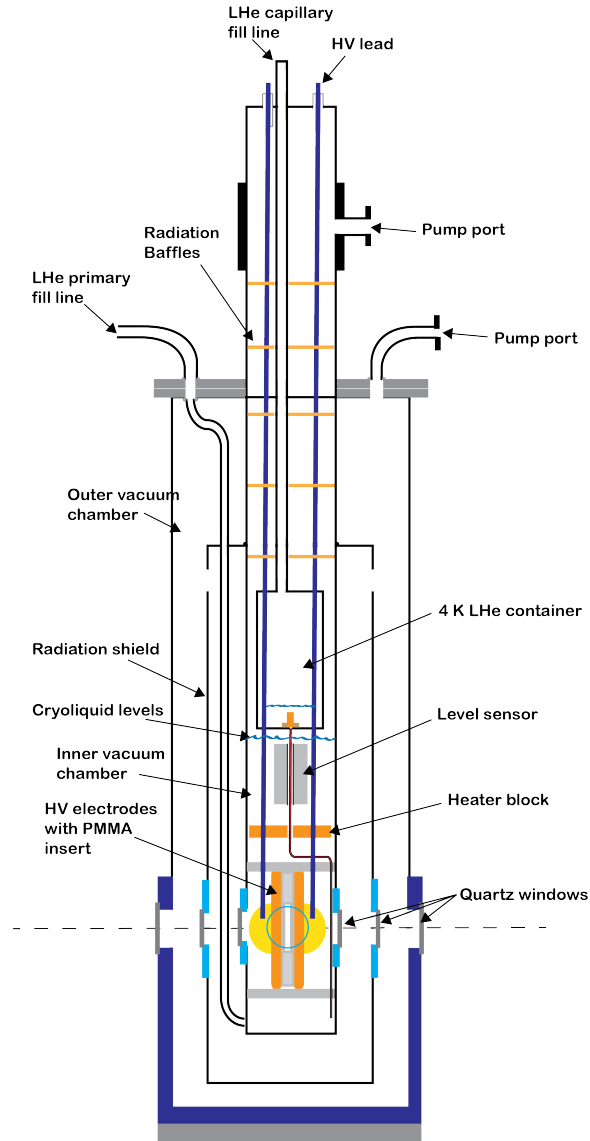
Figure 6.1: The cryostat used for cell charging and binding energy of ions measurements.

The outer chambers of the cryostat are evacuated to a pressure of around 10^{-6} torr during a cooldown. The presence of the windows, connected to the cylindrical structure (radiation shield), creating the barrier between the outer chambers, offers some degree of thermal radiation shielding. This area is known as the "vacuum jacket". Two windows are affixed to the sides of the IVC. The manufacturer applied Versamid 140 hardener and D.E.R. 331 epoxy resin to attach these windows. The four remaining windows, visible on both the radiation shield and the outer vacuum jacket, are also aligned along the same arc. Due to the shared vacuum space on both sides of the windows of the radiation shield, they are securely fastened but not sealed. The windows on the outer vacuum chamber are sealed using O-rings, which are designed to maintain their effectiveness at room temperature.
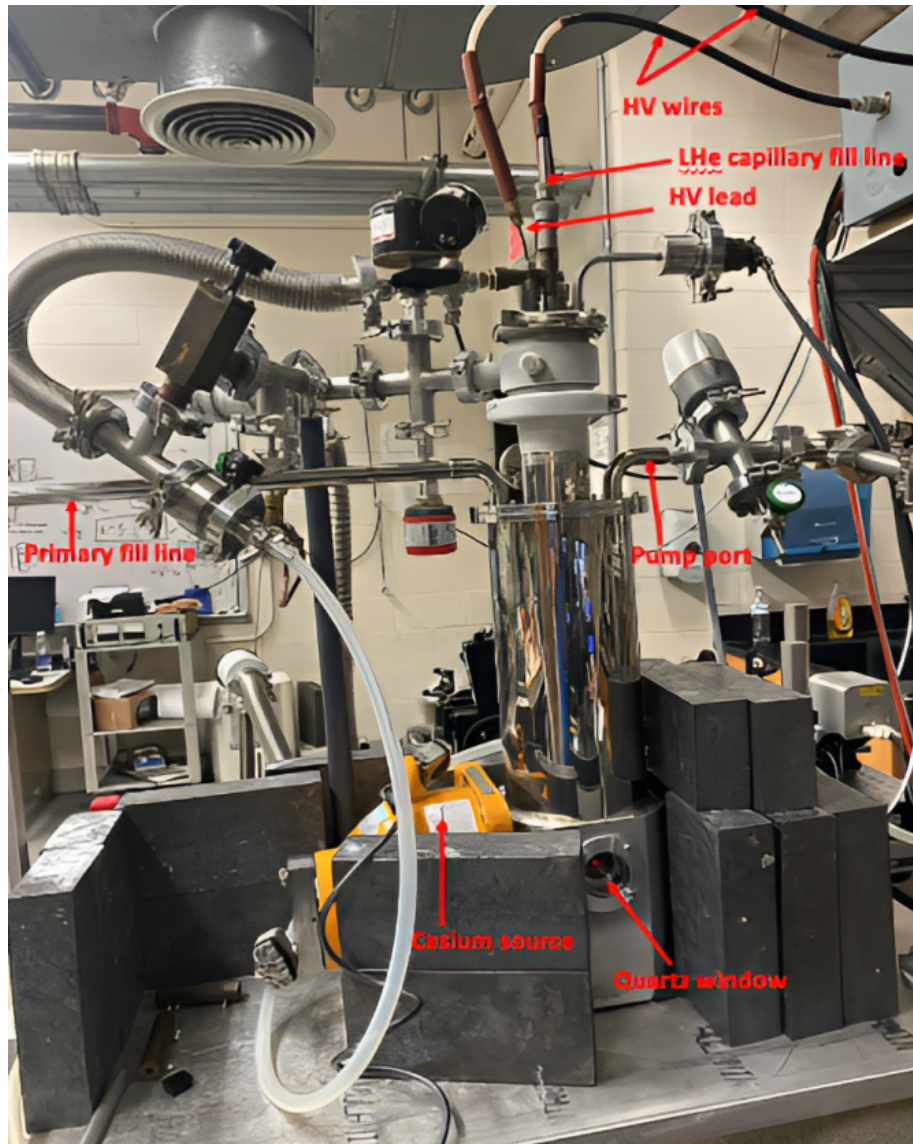
Figure 6.2: The actual picture of the cryostat, showing the laser beam exiting from the window of the cryostat. Both of the wires that extend from the top of the cryostat are connected to high voltages.

6.1.2 Cooldown with Liquid Nitrogen (LN2)

The process of cooling down the cryostat is crucial to this experiment, as it utilizes liquid cryogens, such as nitrogen or helium, to decrease the temperature of the sample. However, in this particular experiment, only liquid nitrogen (LN2) is utilized for cooling down the cryostat. When filling the cryostat with liquid nitrogen, only the primary fill line is used, and the level of liquid nitrogen can be adjusted to suit the experiment's needs. Prior to the introduction of liquid nitrogen, it is necessary to evacuate the vacuum jacket and clean and evacuate the inner vacuum chamber (IVC). A schematic diagram of the cryostat with the two pumping systems is shown in Figure

6.3. To achieve a pressure of 10^{-5} torr (measured by Edwards pressure gauge) at room temperature in the vacuum jacket, a Pfeiffer HiCube 80 Eco turbo pump is used. An Edwards E2M18 direct drive oil pump (roughing pump) is used to pump the IVC pressure down to approximately 10^{-3} torr, as measured by an Edwards Active Gauge ATC-E thermocouple pressure gauge. Depending on the initial conditions present in these chambers, it may take several days to reach these pressures. The attainment of these inner and outer vacuum pressures indicates that the system is ready for cooling.
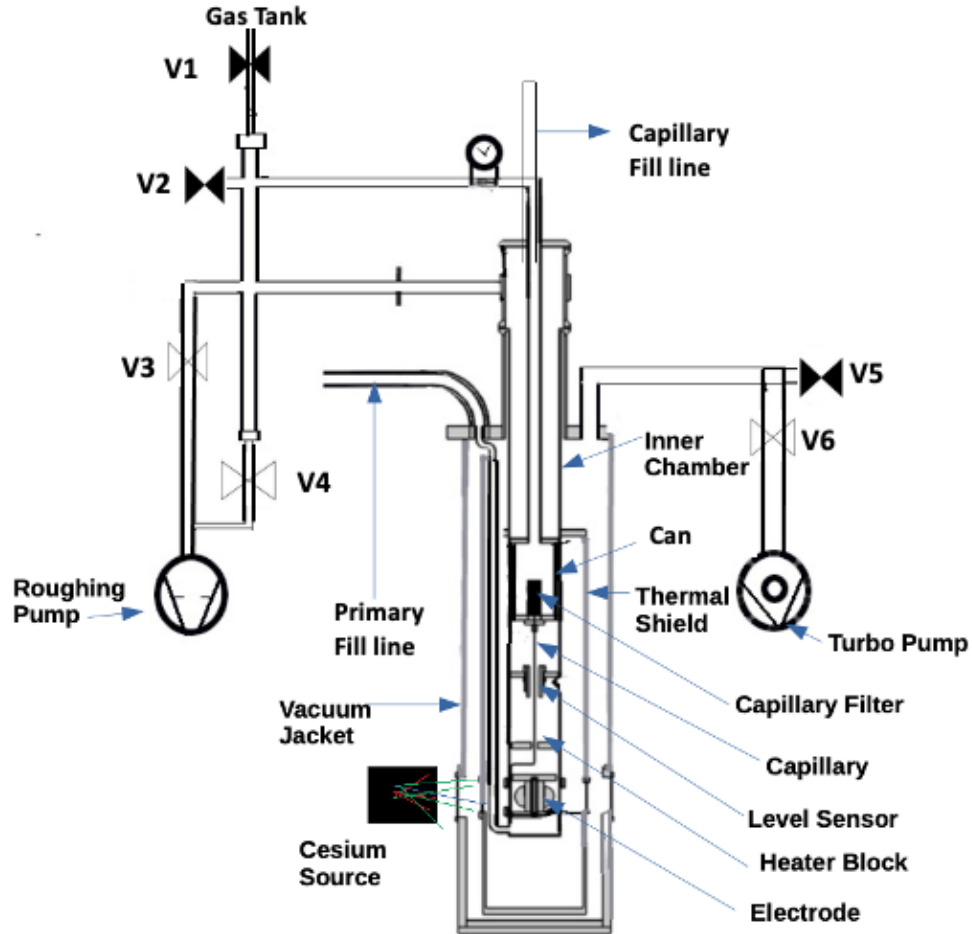
Figure 6.3: This figure shows a schematic diagram of a cryostat with a pumping system. The gate valves with black color indicate that they are closed, while the gate valves with no color are opened.

Transporting liquid nitrogen is easier than transporting liquid helium, which requires more specialized equipment. To prepare the transfer line for liquid nitrogen, one end is placed into the supply dewar for about 15 minutes to purge the line. During this time, valves V3 and V4 are closed to the inner vacuum chamber (IVC), and valve V1 is opened to backfill the IVC with pure nitrogen gas until the pressure is just

over atmospheric pressure, preventing ambient air from entering the chamber when the transfer line is inserted. Once the line is cleaned, it is connected to the primary fill line of the cryostat, and valves V3 and V4 are opened to begin the cooling process. Cryopumping causes the pressure in the outer vacuum chamber to drop from 10^{-5} torr to 10^{-6} torr. To prevent the liquid nitrogen in the fill line from becoming solid, the pressure in the IVC must be maintained at a level greater than 94 torr, usually around 300 torr. The IVC is cooled at a rate of roughly 6 K/min to protect the system from thermal shock, which is controlled by two separate valves: one on the transfer line and the other on valve V3 leading to the roughing pump.

Continuous transfer is performed until the target level of liquid and temperature of around 70 K are attained. After that is done, the valves (V3 and V4) that lead from the pump to the IVC are closed. As soon as the valves V3 and V4 are shut, pressure in the IVC starts rising to atmospheric levels. Once the IVC reaches atmospheric pressure, a valve that connects to the tank is removed and a long tube (V1) is opened, allowing it to be free to the atmosphere. Venting the gas to the environment maintains pressure and reduces bubbling. Ventilation through the long tube gets rid of the risk of contamination by making it fight against the system's positive pressure before it can get in. Before reaching the temperature at which it begins to bubble, the LN2 stays still. 77 K is the temperature at which LN2 begins to bubble. Therefore, the time required to take the data should be anywhere between 70 K and 77 K. The approximate time for this is around 4 hours, which is sufficient time to take the data. As soon as the bubbling temperature is reached, the laser beam is affected, and the data become noisy.

6.2   High Voltage System

The high voltage used in the experiment was created using two Spellman SL30PN150 power supplies (Figure 6.4), with one connected to each electrode. The supplies have positive and negative polarity settings, respectively. Their back panel ground connectors were linked together to guarantee that they share a common ground. Each supply has a maximum potential difference of 30 kV, for a combined maximum potential difference of 60 kV. Both of these are DC voltage sources. The negative polarity of an electrode is modulated by a function generator (Agilent 33120A harmonic waveform generator) with a frequency of 400 mHz [7]. The positive polarity of the electrode is connected to one of the DC Spellman voltage sources. A resistance box (shown in Figure 6.5) is used to limit the amount of current that flows between the supply and the electrodes. This prevents unwanted potential damage to the power supplies. Each supply powers a different electrode, although both utilize the same circuit layout.

For a negative electrode circuit layout, say, (HV$_-$) the values of the three resistors in the grounded resistance box are $R_s = (19.93 \pm 0.01)$ MΩ, $R_1 = (99.73 \pm 0.01)$ MΩ, and $R_2 = 10$ kΩ respectively (measured by an Agilent 3458A $8\frac{1}{2}$ Digital Multimeter). The three resistors serve as voltage dividers, with the R_s resistors connected in series with each electrode. This arrangement is designed to limit the current flow and protect the supplies from any damage. This restricted the current to a maximum of ($I_{max} = \frac{30kV}{19.93M\Omega}$) 1.51 mA at a voltage of 30 kV. This step was taken to reduce

Figure 6.4: At the bottom left of the picture are two Spellman SL30PN150 high voltage (HV) power sources. The top items on the top shelf are a waveform generator and a digital multimeter.

the heating effect in the resistors. Following the current-limiting resistor, the circuit branches out in two different directions. There is a route that goes straight to the electrode. The second path connects to ground through two more resistors, with R_1 and R_2. This division creates a basic voltage divider. The HV$_-$ involves an AC supply with DC offset that cannot be directly controlled from Spellman. This is operated through function generator. The voltage drop across R_2, can be used to monitor the electrode voltage (V_E). The voltage V_2 is measured with a digital multimeter (Keysight 34401A $6\frac{1}{2}$ Digital Multimeter).

If V_{supply} is the potential difference provided by the supply, then the voltage at the electrode V_E is given by

$$V_E = \frac{R_1 + R_2}{R_s + R_1 + R_2} V_{supply}. \tag{6.1}$$

Inserting the value of R_1, R_2, and R_s in Equation 6.1,

$$V_E = \frac{99.73 M\Omega + 10 k\Omega}{19.93 M\Omega + 99.73 M\Omega + 10 k\Omega} V_{supply} = 0.8335 V_{supply}. \tag{6.2}$$

since, the voltage drop across R_2 is measured, which is given by the relation,

$$V_2 = \frac{R_2}{R_s + R_1 + R_2} V_{supply}. \tag{6.3}$$
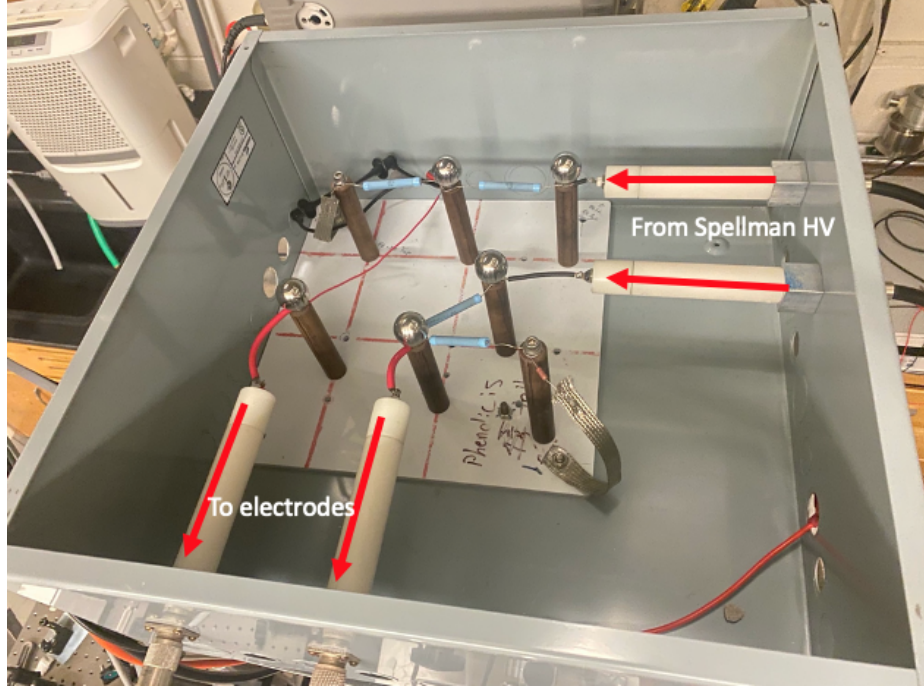
Figure 6.5: A resistance box that has two circuit layouts: one for negative AC voltage with DC offset HV$_-$ and the other for positive DC voltage HV$_+$. Each circuit layout has resistors that form a fundamental voltage divider circuit.

From Equations 6.2 and 6.3, the electrode voltage and measured voltage relationship is established which is

$$V_E = (1 + \frac{R_1}{R_2})V_2 = 9974V_2. \tag{6.4}$$

Similarly, the positive electrode circuit layout, say, (HV$_+$) also consists of three resistors in a grounded resistance box: $R'_s = (20.96 \pm 0.01)$ MΩ, $R'_1 = (100.37 \pm 0.01)$ MΩ, and $R'_2 = 10$ kΩ (measured by an Agilent 3458A $8\frac{1}{2}$ Digital Multimeter). R'_s limits the current to a maximum of 1.43 mA at 30 kV. The circuit branches out in two directions, with one path going straight to the electrode and the other path containing R'_1 and R'_2 which create a voltage divider. Using the voltage divider relation, the electrode voltage (V'_E) is measured using the Equation 6.1 with the known values of R'_s, R'_1, and R'_2. The positive electrode circuit layout for (HV$_+$) involves a DC supply that can be controlled directly from Spellman. By knowing the value of the DC supply voltage i.e. V_{supply}, the voltage of the electrode can be measured.

6.2.1 Impact of External Circuitry on the Electric Field

Utilizing high-resistance resistors may have a range of effects on the HV applied. Concerns such as the change in voltage at the electrodes owing to resistor tolerances, temperature coefficients, and voltage coefficients must be carefully evaluated. As external current limiters, metal-oxide resistors (ROX; Vishay) were employed. Two further resistors in series, with values of $\sim$100 MΩ and 10 kΩ, were connected in
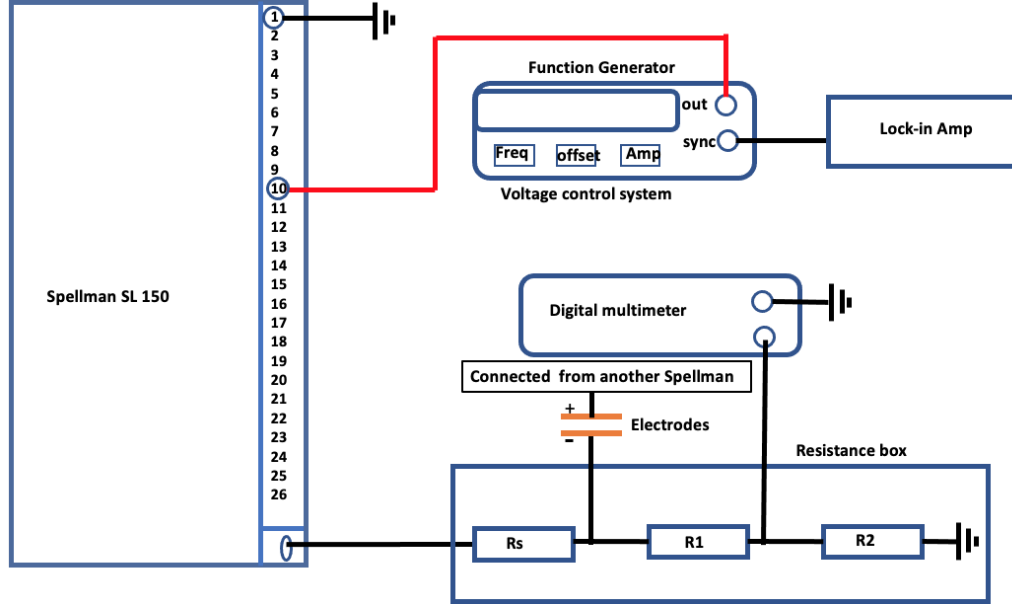
Figure 6.6: Schematic diagram of resistors connected in the resistance box.

parallel with the electrode. This enabled the electrode voltage at the 10 kΩ resistor test point to be monitored. The coefficients of temperature were reported as 200 ppm/°C. since the laboratory temperature was maintained within 1 °C and the charging currents were considerably below ∼1.5 mA throughout data collection, any temperature-dependent HV variations were insignificant (because of low power ∼4 W for 20 kV). The resistor's voltage coefficient is another factor to consider. It is a nonlinear phenomenon that produces a change in the resistance as the applied voltage varies. The ROX metal-oxide resistors have stated values of 4 ppm/V. This might result in a 4% variation between the voltage recorded at the test point and the voltage measured at the electrodes. However, calibration and comparison of the two resistor chains for the electrodes revealed a linear response to the applied HV, and the measured voltages at the test sites (across the 10 kΩ resistors) varied by about 2% as shown in Figure 6.7.

The measurement of actual value of resistances in HV$_-$ (given by $R_s = (19.93 \pm 0.01)$ MΩ, $R_1 = (99.73 \pm 0.01)$ MΩ, and $R_2 = 10$ kΩ) and HV$_+$ (given by $R'_s = (20.96 \pm 0.01)$ MΩ, $R'_1 = (100.37 \pm 0.01)$ MΩ, and $R'_2 = 10$ kΩ) helps to explain the variation of this effect by around 1.5%. Another 0.5% effect may be attributed to other factors, as previously explained. The real electrode voltages were adjusted to account for this impact. Furthermore, the equipment's support structures were placed in chambers filled with sand to dampen vibrations and reduce noise caused by microphonics.
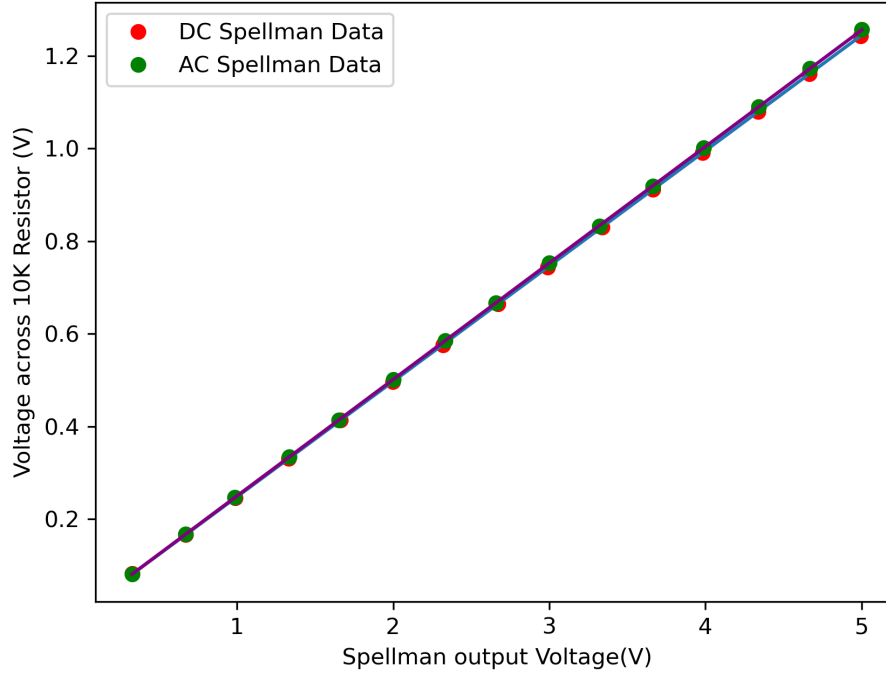
Figure 6.7: Linearity relationship of the applied Spellman high voltage and the measured voltages at the test points 10 kΩ resistor. The red points are DC Spellman data and the green points are AC Spellman data. The Spellman output voltage is determined using the control voltage measurement, with 30 kV equating to 10 V. The measurement of voltage across a 10 kΩ resistor is performed up to 15 kV of applied Spellman high voltage. During this measurement, the connection with the electrodes were disconnected to prevent any potential sparking.

6.2.2 RC Effects

In addition to the resistors that have already been described, the internal capacitances of the power supply each measured 4 nF. Even at a modulation frequency of $f_{mod} = 400$ mHz (T = 2.5 s), the RC time constant of 480 ms that is produced by the combination of these huge resistances and capacitors cannot be considered inconsequential. The data obtained from the lock-in amplifiers were utilized to determine the ellipticity by applying Equation 5.37. The lock-in signal, on the other hand, simply shows a voltage that is proportional to a reference frequency called f_{mod}. Any signal distortion reduces the amplitude at the base frequency by shifting the signal intensity into higher harmonics. A combination of a ∼100 MΩ and a 10 kΩ resistor, both linked in series, were coupled in parallel to each electrode to measure and monitor the high voltage at the electrodes.

In this setup, a 2.5 V voltage drop across a 10 kΩ resistor equated to 30 kV at a single electrode. An ADC connected to the data acquisition computer or a regular voltmeter may both be used to measure this modest voltage drop. The voltage on

each electrode is represented by the values taken from its V_2. This data are multiplied by $\sim$10,000 in order to determine the actual voltage on the electrode.
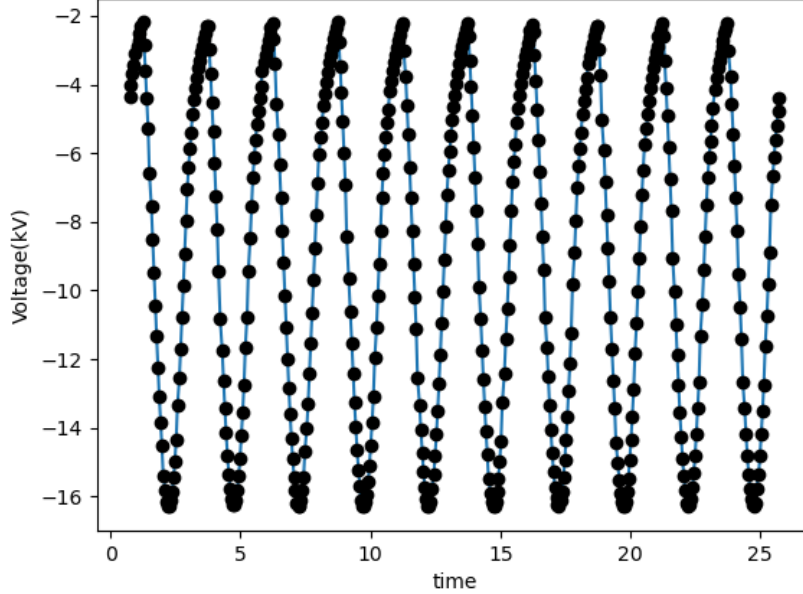
Figure 6.8: Voltage drop signal measured across the measurement resistor, R_2. A sinusoidal driving waveform of frequency of 400 mHz was applied in HV$-$ loop.

Figure 6.8 displays the AC signal obtained from the electrode circuit layout (HV$_-$). The Fast Fourier Transform (FFT) of the AC signal is shown in Figure 6.9. According to the FFT plot, the typical AC amplitude at the electrodes was found to be approximately -6.87 kV, based on the first peak observed at 400 mHz. The DC offset at the electrodes was also determined to be $2V_{DC} = -17.99$ kV, which was represented by the peak at zero frequency. In addition, peaks at 800 mHz, 1200 mHz, and 1600 mHz were observed, and these peaks were attributed to the RC effect, which contributed only 13.3% of the total signal. The reason for using 2 V_{DC} is because when the FFT is applied to a real-valued time-domain signal, it produces a complex-valued frequency-domain signal that is symmetric about frequency zero. This means that the FFT contains both positive and negative frequency components, but the negative frequency components are just the complex conjugate of the positive frequency components. Based on the electrode circuit layout (HV$_+$), the DC value was determined to be 5.805 kV. Taking into account the contributions from both electrodes, the overall DC offset was approximately 14.80 kV.

By using Fourier transforms or a direct comparison of the monitored signal and the lock-in signal, the impact on the signal might be identified. The peak value retrieved from the RMS value recorded by the lock-in amplifier was found to be 86.7% of the actual peak value across the resistor using both approaches, indicating a 13.3% loss in
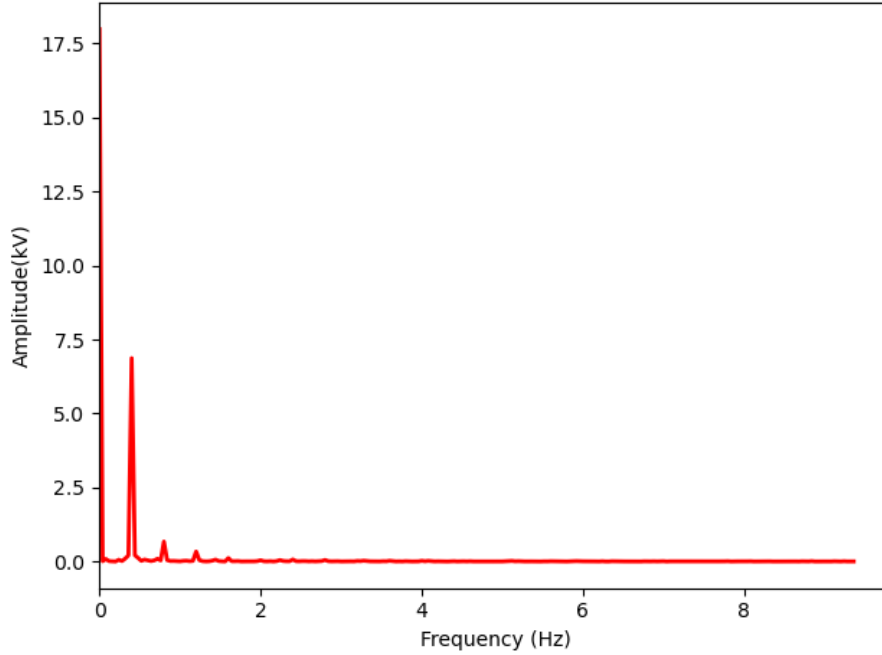
Figure 6.9: Fourier transforms of the monitored signal from Figure 6.8.

signal caused by the RC effect at $f_{mod} = 400$ mHz. This signal reduction's uncertainty is 0.54%.

The whole high-voltage circuit was simulated using the electrical circuit modeling program LTspice [69], which demonstrated a discernible signal perturbation at frequencies as low as 10 mHz. This is because reducing the frequency may lessen RC disturbances. The drawback of adopting a low frequency is that it will result in more $1/f$ noise and longer data collection periods. The high voltage values previously described were selected because there was only a little loss from the RC effect and because the boost to the signal would eventually be negated by the loss of data points. This effect was accounted for in the data analysis [7].

Chapter 7 Measurements and Results

7.1 System Calibration and Noise Reduction

The calibration of the system should be carefully considered before examining the cell charging action and measuring the binding energy of ions on PMMA surfaces. Using the same experimental setup, Mark Broering reports his findings for the determination of the Kerr constant of LN2. The measurement of LN2's Kerr constant is shown in Figure 7.1. His thesis [7] includes details on this measurement. The value determined by Sushkov, et al. [70] and his measurement are in excellent agreement. The values of the Kerr constant of LN2 obtained by Mark Broering and Sushkov, et al. are given by Equations 7.1 and 7.2.

$$(K_{LN2})_{Broering} = (4.38 \pm 0.10) \times 10^{-18} (\frac{cm}{V})^2 \tag{7.1}$$

$$(K_{LN2})_{Sushkov} = (4.38 \pm 0.15) \times 10^{-18} (\frac{cm}{V})^2. \tag{7.2}$$
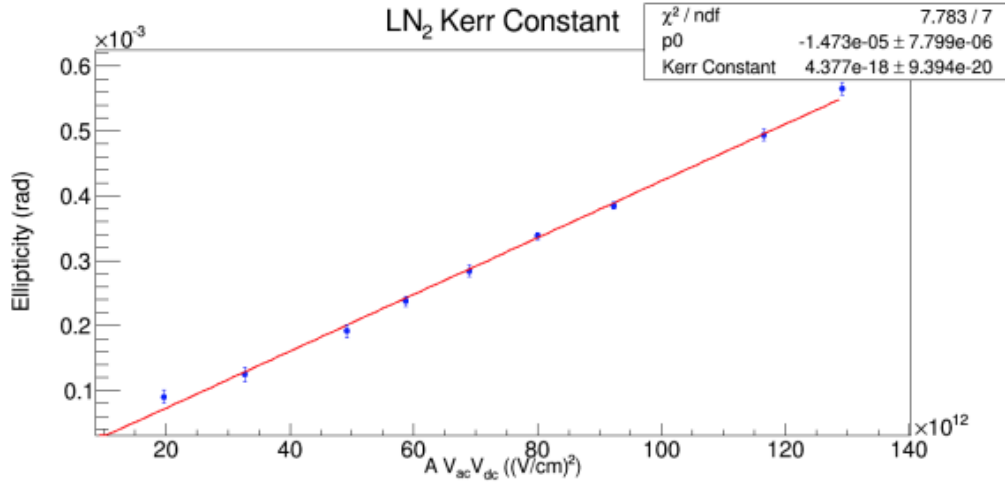
Figure 7.1: The plot shows the ellipticities that were measured at various voltages inside LN2. The value of $A = \frac{2\pi L_{eff}}{\lambda d^2}$ and the slope is equal to the Kerr constant [7].

In addition to system calibration by measuring the Kerr constant of LN2, system enhancement also includes laser beam alignment. The alignment of a laser beam is very challenging and time consuming. To properly pass a laser beam through a small gap between PMMA plates, the beam must be collimated and accurately steered through the electrode system to prevent scraping of the plates. The typical beam size is kept small (less than 1 mm in diameter; see Figure 5.2) and the alignment is adjusted for maximum transmission by measuring the transmitted power as a function of the horizontal laser beam angle. Figure 5.3 shows the measured laser

beam profile passing through the small gap between PMMA plates. The maximum power transmitted through the cryostat is measured where the alignment is adjusted for minimizing the scraping of the laser beam on the walls of PMMA surfaces.

To test the performance of the system and improve the sensitivity of the measurement of ellipticities of a few microradians at room temperature, the prototype setup is designed to measure the Kerr constant of olive oil as shown in Figure 7.2.
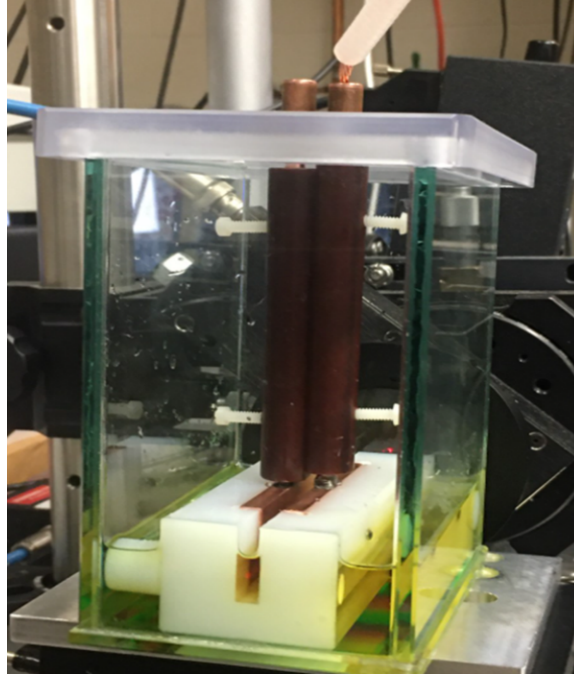
Figure 7.2: Experimental setup for measuring the Kerr constant of olive oil. A laser beam passes through the gap of a glass jar containing the olive oil, while two connectors at the top of the jar supply voltage.

Olive oil is a suitable liquid for measuring the Kerr constant due to its high Kerr effect [71], non-conductive nature, and low viscosity. According to Mousavi's study [71], the Kerr constant of fresh olive oil is 1.49×10^{-9} m/V^2. The high Kerr constant of fresh olive oil enables more precise and accurate measurements of the Kerr effect. This test identified many exterior noise sources, including vibrating cables, operating pumps, and other ambient sources. After minimizing these different sources, Kerr constant of olive oil was measured in various electric fields. Figure 7.3 displays the measurement of the Kerr constant of olive oil at various electric fields and dates in the year 2021. Based on this measurement, two effects were observed in olive oil. The first is the impact of aging, followed by the dependency on the electric field.

The aging process could potentially affect the Kerr constant of the coil by altering its chemical composition or physical properties. For instance, exposure to light, heat, or oxygen could cause oxidation of the oil, which could lead to changes in its refractive index or viscosity. In addition to that, there may be the presence of impurities that have been introduced to it through time. These changes could, in
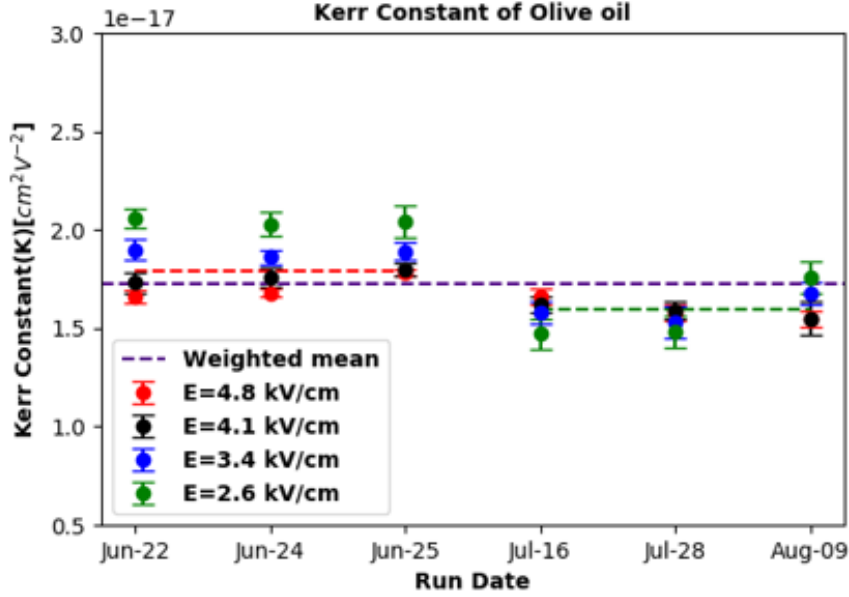
Figure 7.3: Kerr constant measurement of olive oil at different electric fields at different dates and times. The weighted means of all the data are purple dotted lines. Weighted mean of first three data is red dotted line. Weighted mean of last three data is green dotted line.

turn, affect the magnitude of the Kerr effect and the extracted value of the Kerr constant. This effect is observed in Figure 7.3. The measured value for the weighted mean of the Kerr constant, represented by the purple dotted line in Figure 7.3, is $(1.729 \pm 0.008) \times 10^{-17} (\frac{cm}{V})^2$. The Kerr constant measured on June 22, June 24, and June 25 seems to be constant with a mean value of $(1.787 \pm 0.009) \times 10^{-17} (\frac{cm}{V})^2$ (red dotted line). When we tested the same olive oil in July and August, however, the Kerr constant values dropped, with an average value of $(1.598 \pm 0.015) \times 10^{-17} (\frac{cm}{V})^2$ (green dotted line).

As demonstrated in Figure 7.4, the Kerr constant of olive oil is also dependent on the magnitude of the electric field. All the measurements were taken on the same day, June 25, 2021. Here, the electric field lowers as the electric field increases and looks saturated at higher electric field levels. To confirm this saturation, more measurements are necessary at higher electric fields.

The olive oil is used just to find the sources of outside noise in our system and make the system more sensitive. Therefore, a detailed examination of the data for the olive oil was not carried out. To verify these two effects, further investigation is necessary.

The primary objective of this study is to investigate the use of olive oil as a medium for identifying and minimizing external noise sources. However, it should be noted that the handling and storage of the olive oil were not carried out using the same stringent protocols required for measuring the Kerr constant. Therefore, the Kerr constant values obtained in this study may exhibit variations due to po-
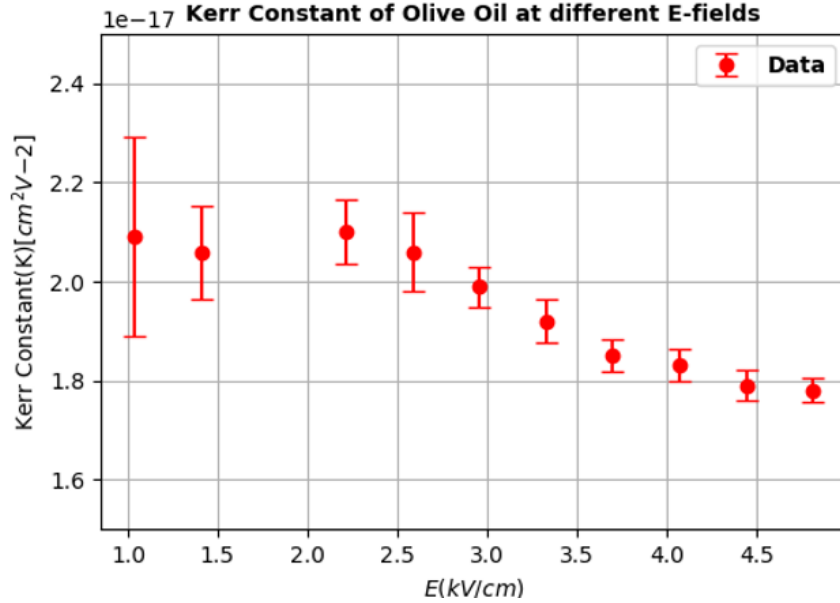
Figure 7.4: Variation of the Kerr constant of olive oil with the magnitude of electric fields.

tential inconsistencies in the handling and storage of the olive oil. Nevertheless, this study demonstrates an effective strategy for identifying and mitigating external noise sources in Kerr effect measurements, by employing olive oil as a medium. The results indicate that the use of olive oil as a medium leads to a substantial reduction in noise levels, by up to 30% compared to previous studies conducted by Broering [7]. This finding contributes significantly to the refinement of the Kerr effect measurement technique and enhances its accuracy and reliability.

7.2 (Quasi-Static) Dielectric Constant of PMMA

In the nEDM@SNS experiment, the dielectric constant of PMMA is important to know at low temperatures because PMMA material is used in the measuring cells where the electric field is applied. The dielectric constant determines the strength of the electric field that can be applied across the PMMA plates, and accurate measurements require understanding and controlling the electric and magnetic fields within the apparatus. Changes in the dielectric constant of PMMA at low temperatures can affect the strength of the electric field and the accuracy of the measurements, making it crucial to know the dielectric constant in this range.

The dielectric constant depends on various factors, including the type of material, temperature, and frequency of the electric field. At a molecular level, it represents the degree to which the electrons in the material can be displaced by an electric field. In this study, the frequency of the electric field is low (400 mHz), so it is termed a "quasi-static dielectric". The temperature dependence of the dielectric constant has not been extensively explored. Shirvel Stanislaus, a collaborator on nEDM@SNS,

investigated how the dielectric constant of PMMA changed with temperature. According to his research, PMMA's dielectric constant drops as temperature decreases. The measured dielectric constant of PMMA at 77 K is around 2.04 [72]. The systematic and statistical uncertainties are not available for taken into account in this measurement.

Similarly, Mark Broering's thesis [7] measured the dielectric constant of PMMA at 70 K using the same experimental setup as our study. The dielectric constant was found to be $1.8 \pm {}^{0.4}_{0.3}$, assuming no shrinkage of the PMMA and electrode system. However, our study acknowledges that the contraction of the system at 70 K is an important factor to consider in determining the precise value of the dielectric constant of PMMA. Thus, the experimental geometry was constructed based on the contraction of the PMMA electrode system to obtain more accurate results.
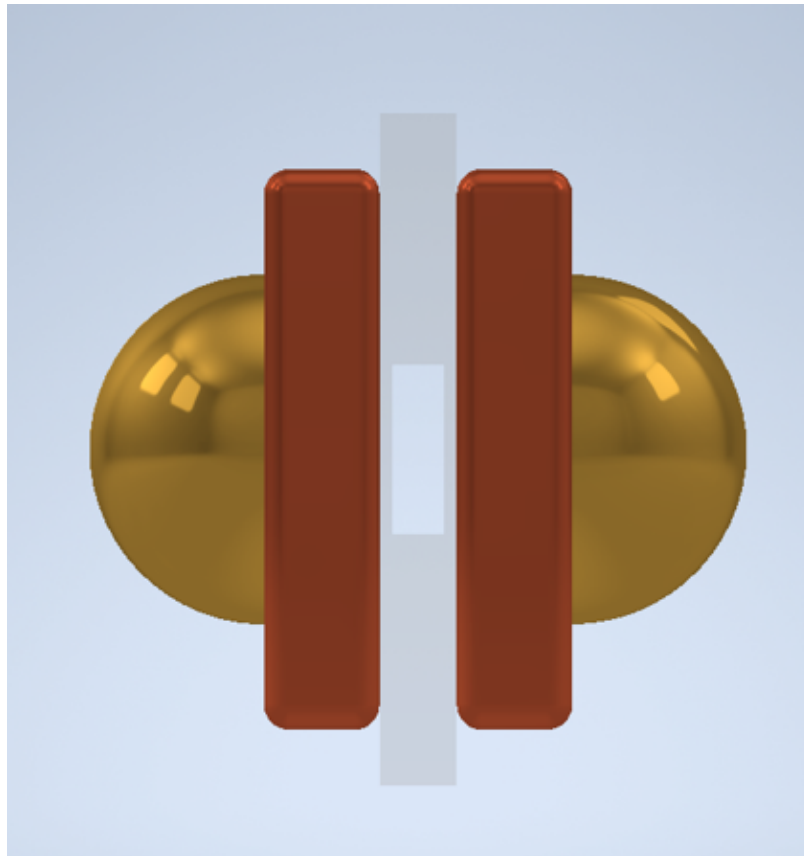
Figure 7.5: COMSOL geometry created for the experimental area. The two reddish-brown areas represent the copper electrodes. Between the electrodes, two thin glued PMMA plates were inserted to form the central gap. The gap was filled with liquid nitrogen during the experiment. The geometry was designed to enable accurate measurement of the dielectric properties of PMMA.

This study aims to determine the dielectric constant of PMMA using both computational and experimental methods. To achieve this objective, the first step was to construct a geometry for the COMSOL simulation. The geometry created in

COMSOL to represent the experimental region is shown in Figure 7.5. For this illustration, the majority of the background elements were concealed to emphasize the cell arrangement. Every object has to have a material given to it after the geometry has been generated. All pertinent physical characteristics must be encoded into that substance. The relative permittivity κ is necessary for straightforward stationary electric field models.

The sample region was designed as a capacitor consisting of three layers of dielectric materials. The experimental setup involved the insertion of two thin-walled PMMA plates into the space between the copper electrodes, with a central area filled with liquid nitrogen to maintain a low temperature. The gap between the electrodes was constructed using a two-piece clamp shell PMMA design that was carefully glued together to form a single unit. The precise positioning of the PMMA plates in close proximity to each other allowed for accurate measurement of the dielectric properties of PMMA at low temperatures. The use of PMMA for the gap construction provided a suitable and electrically inert material, while the inclusion of liquid nitrogen ensured a controlled and stable measurement environment. When a linearly polarized laser beam travels through the sample area, the inclusion of the PMMA plates affects the electric field strength within the cryogenic liquid and therefore has an effect on the induced Kerr ellipticity. The induced ellipticity measurement technique was employed to extract the dielectric constant of PMMA, κ_{PMMA}, at low temperatures. The two distinct dielectrics alter the size of the electric field at the electrodes' center in the following ways:

$$E_{LN2} = \frac{V_{eff}}{d + 2t(\frac{\kappa_{LN2}}{\kappa_{PMMA}})}, \tag{7.3}$$

where $V_{eff} = \sqrt{V_{AC}V_{DC}}$ is the effective voltage used for the signal extraction, d is the gap width between the PMMA plates ($d = 2.84$ mm at room temperature), and t is the thickness of the PMMA plate ($t = 0.64$ mm at room temperature). An ultrasonic probe (Model TI-PVX, 3/16" pencil) was used to measure the PMMA plates' thicknesses with an accuracy of 10 μm. The PMMA did somewhat contract once the system was cooled to around 70 K, and the electrodes may now move in unison. Using a linear coefficient of expansion of $9.28 \times 10^{-5} K^{-1}$ for PMMA and $16.7 \times 10^{-5} K^{-1}$ for copper, the size decrease was calculated taking this impact into consideration. This meant, in our situation, that the PMMA thickness was decreased to $t = 0.63$ mm and the center gap was decreased to $d = 2.79$ mm. The tables 7.1 and 7.2 show the dimensions of the electrodes and PMMA at room temperature (293 K) and the cool-down temperature (70 K).

The geometry was modeled with COMSOL modeling software to properly take into consideration fringe-field effects. For various potential values of the PMMA dielectric constant, the integral of the squared electric field across the length of the sample region, $\int_0^L E^2 dl$, was calculated. Figure 7.6 shows the distribution of the electric field within the experimental setup. The central gap region is of particular interest, as a uniform electric field is required for accurate measurement of the dielectric properties of PMMA. As expected, the electric field distribution is found to be uniform in this region, confirming the suitability of the experimental setup for the in-

Table 7.1: Dimensions of electrodes at room temperature and cool-down temperature.

Electrode	Temperature (293 K)	Temperature (70 K)
Width (mm)	6.33	6.31
Length (mm)	30	29.89
Height (mm)	30	29.89

Table 7.2: Dimensions of PMMA at room temperature and cool-down temperature.

PMMA	Temperature (293K)	Temperature (70K)
Width (mm)	4.12	4.03
Length (mm)	36	35.26
Height (mm)	36	35.26

tended measurements. The measured electric field values are in good agreement with the calculated values obtained from Equation 7.3, further validating the accuracy of the experimental setup. The integral was evaluated over a variety of values of PMMA
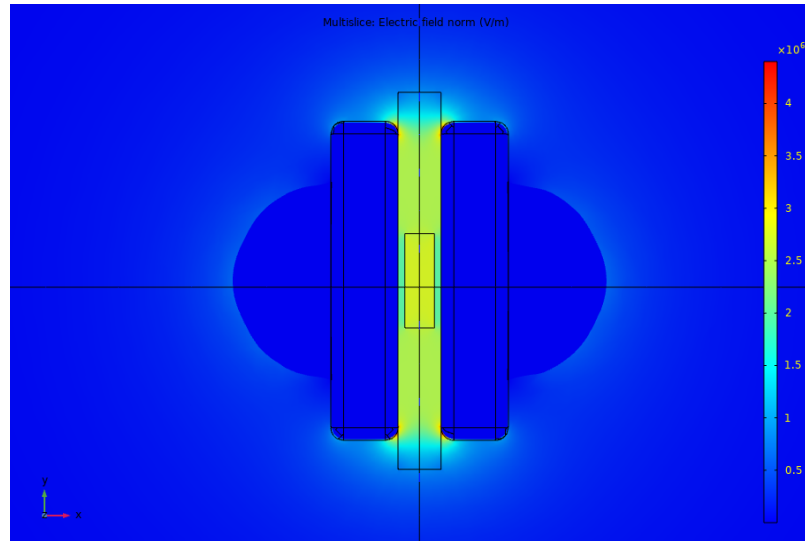
Figure 7.6: E-field distribution plot, in (V/m), from a COMSOL simulation.

since the dielectric constant for PMMA can vary from roughly 2 to 5, with a value most likely between 3 and 4, at low frequencies [73]. Figure 7.7 displays the outcomes of two distinct simulations as blue and green curves. In one instance (blue), as the system is cooled, the copper electrodes and PMMA plates are permitted to come closer together. In another instance, the copper electrodes' spacing was expected to be the same as at room temperature, despite the PMMA insert shrinking (green). With the voltages of $V_{AC} = 6.833$ kV and $V_{DC} = 14.817$ kV, an ellipticity of $\epsilon_1 =$
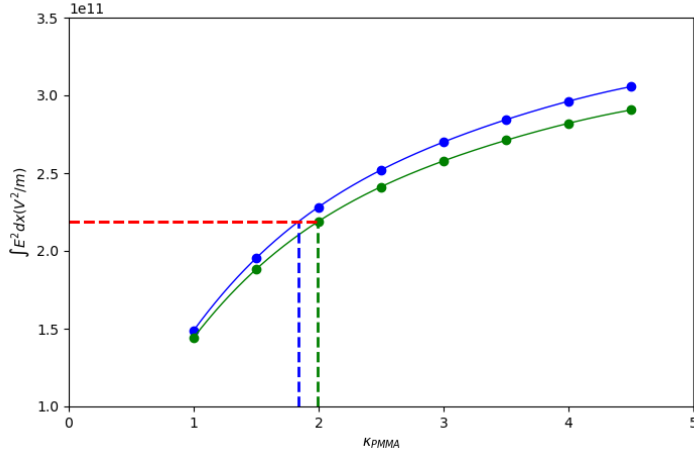
Figure 7.7: Numeric integration of $E^2 dl$ vs. κ_{PMMA} with liquid nitrogen filling the gap between the PMMA plates. The blue circles are the results of a COMSOL simulation where the separation of the electrodes was consistent with the thickness of the shrunk PMMA; the green circles are the same COMSOL simulation without moving the electrodes, i.e., they were kept at room temperature positions. The green and blue lines are 4th-order polynomial that fits the data points.

959.5 ± 0.8 (stat) μrad was observed. With this Kerr ellipticity measurement, the blue and green curves of Figure 7.7 may be restricted. The numerical value of the integral extracted with the account of fringe-field effects (from 0 to L) at a voltage of $V_{eff} = 10.062$ kV is $(2.188 \pm 0.05) \times 10^{11}$ V^2/m, which is obtained from Equation 7.4.

$$\int_0^{L_{eff}} E(z)^2 \, dz = \lambda \frac{\epsilon_1}{2\pi K}. \tag{7.4}$$

This value is represented by the red dotted line in Figure 7.7. The corresponding values of κ_{PMMA} for the blue and green curves based on the dotted red horizontal line are 1.84 and 1.99, respectively. The statistical and systematic errors were added in quadrature, assuming that the position of the electrodes is constrained by the thickness of the shrunk PMMA insert. In one instance (blue), where both PMMA and electrodes shrank together, the value of the dielectric constant is $\kappa_{PMMA} = 1.84^{+0.11}_{-0.11}$. In a second scenario in which the electrodes are immobile (green curve), the value of the dielectric of κ_{PMMA} is $1.99^{+0.12}_{-0.13}$. since the actual spacing between the electrodes was not measured when the system was cooled, the most acceptable determination of PMMA is the average of the two readings, resulting in a value of $\kappa_{PMMA} = 1.91^{+0.20}_{-0.18}$ at T = 70 K.

7.3 Cell-Charging Measurement in Liquid Nitrogen

The cell charging effect was evaluated in liquid nitrogen after the laser beam was properly aligned and the system's performance was verified using olive oil. When

the liquid nitrogen is slowly put into the cryostat, the temperature starts to drop from room temperature to 70 K. Due to thermal contraction, the system dimensions change after a cool-down process from room temperature to 70 K. To collect data on cell charging, a baseline measurement was taken by establishing the Kerr effect with a "cell" inserted before opening the shutter of the cesium source. The shutter was then opened for a specific duration to enable charge accumulation on the cell walls. Following this, the shutter was closed, and a steady lower ellipticity was measured, indicating that the charges were separated and adsorbed on the PMMA surface, producing an opposing electric field to the applied electric field. To evaluate the impact of the absence of an electric field on the adsorbed charges, the electric field was turned off for a while after measuring the charging cycle and turned back on. Furthermore, the stored charges' response to a high voltage reversal was examined by reversing the electric field polarity and performing another ellipticity measurement.

The findings of a liquid nitrogen cell charging operation are shown in Figure 7.8. The horizontal axis indicates data collection time, while the vertical axis indicates measured ellipticity. The charging signal was fitted using a first-order polynomial, and the other regions (excluding charging) were each fitted independently using a zeroth-order polynomial. The blue lines depict the fit for each section of the cell charging run. The Mod1 and DC lock-in amplifier integration times were set to 20 s per point at a modulation frequency of 400 mHz. The data were collected at a DC voltage of V_{DC}= 14.806 kV $\pm$ 0.010 kV, and an AC modulation voltage of V_{AC}= 6.871 kV $\pm$ 0.010 kV. The baseline signal was 962.2 $\pm$ 0.6 (stat) μrad with the greatest
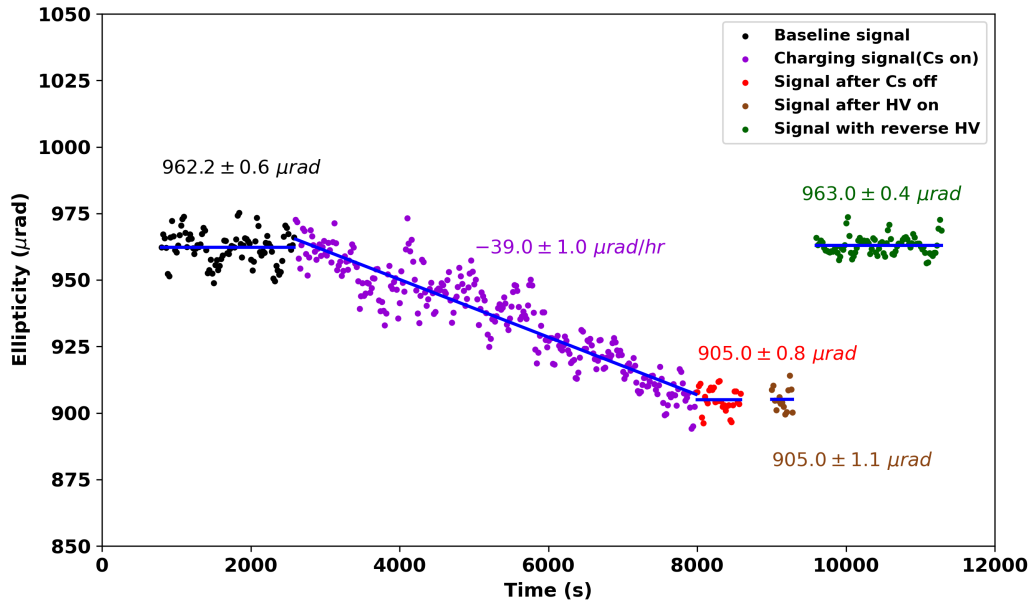
Figure 7.8: Cell charging results in liquid nitrogen.

net electric field ($\sim$27.5 kV/cm) in our system. Beyond this high voltage, sparking was observed. Each data point within this range had a statistical error per data

point between 4 and 6 μrad, although, for the purposes of improved visualization, error bars were removed from the figure. The shutter on the cesium source was then opened. The cesium-137 isotope decays with 662 keV γ rays and 514 keV (1.176 MeV) β particles. Only the gamma radiation reached the target region [61]. This γ radiation ionized the liquid nitrogen and generated charged particles, which can drift and be adsorbed on the surfaces of the measurement cell. This can result in a reduction of the net electric field, causing an exponential drop in the signal with a linear lope slope of 39.0 ± 1.0 (stat) μrad/hr. This is called the cell charging effect. After almost an hour, the cesium source shutter was closed, and the signal stabilized at a lower value of 905.0 ± 0.8 (stat) μrad. The net DC offset of the electric field over an hour is seen to have decreased by around 6% in this instance. The first section of the blank data region ($\sim$8700 s to $\sim$9000 s) corresponds to the interval when the electric field was turned off. The ellipticity measurement remained unchanged when the HV was turned back on, showing that all of the adsorbed charges were still present on the PMMA surfaces. However, the signal returned to 963.0 ± 0.4 (stat) μrad upon field reversal (which came after the second blank segment $\sim$9400 s to $\sim$9600 s). All the ions did recombine during the process. For this cell charging study, the statistical uncertainty in the measurements was found to be significantly larger than any systematic uncertainties that were present. As a result, only the statistical uncertainty was taken into account in the data analysis.

A previous study by Broering [7] had conducted similar measurements of cell charging, using the same experimental setup and methodology. Our results demonstrate a significant improvement in the statistical uncertainty of the measurement, with a reduction of approximately 30% compared to the previous study. This improvement can be attributed to the sensitivity and accuracy of our measurements. The improvement is made by minimizing the external ambient noise sources, which were identified using the olive oil Kerr effect measurement.

7.4 Signal Measurements with Red and Blue Laser Beams

The optical Kerr signal is a change in the material's refractive index caused by a strong electric field. The magnitude of this change is dependent on the wavelength of the light being used. Typically, the effect is stronger for shorter wavelengths of light, such as ultraviolet or blue light, and weaker for longer wavelengths, such as infrared or red light. Thus, the Kerr signal or ellipticity is inversely proportional to the wavelength, which was described by Equation 4.30.

The ellipticity was measured at two different wavelengths, one with a red laser beam (with a wavelength of 633 nm) and the other with a blue laser beam (with a wavelength of 404 nm). Given the same medium, device, and applied electric field, the relationship between two wavelength signals based on Equation 4.30 is given by

$$\frac{\epsilon_{blue}}{\epsilon_{red}} = \frac{\lambda_{red}}{\lambda_{blue}}. \tag{7.5}$$

Theoretically, for the specified λ_{red} and λ_{blue} values, the blue laser beam's ellipticity

signal is 1.57 times stronger than the red laser beam's signal, which is given by,

$$\frac{\epsilon_{blue}}{\epsilon_{red}} = 1.57. \tag{7.6}$$

The experiment was performed under identical conditions using a red laser beam and
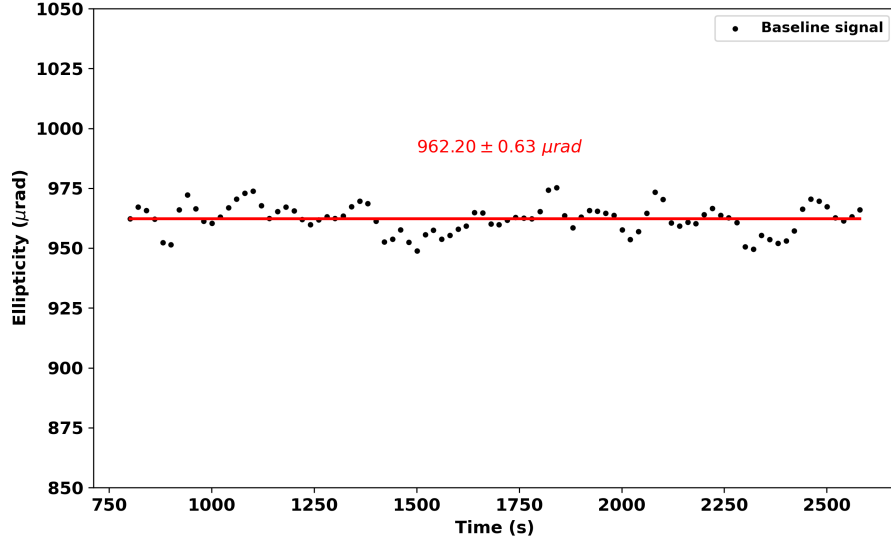
Figure 7.9: Measurement of the baseline ellipticity signal when the red laser beam of wavelength λ= 633 nm travels through liquid nitrogen at V_{AC}= (6871 $\pm$ 10) V and V_{DC}= (14806 $\pm$ 10) V voltages.

a blue laser beam. Figure 7.9 shows the ellipticity signal that was acquired from the experiment where a red laser beam was passed through liquid nitrogen with electrode voltages of V_{AC}= (6871 $\pm$ 10) V and V_{DC}= (14806 $\pm$ 10) V. The measured ellipticity signal value is ϵ_{red}= (962.20 $\pm$ 1.7) μrad with statistical and systematic errors added in quadrature.

The ellipticity signal was tested with the blue laser beam in the same way that the red laser beam was used. The measured value of the ellipticity for the blue laser beam was $\epsilon_{blue} = 1525.27 \pm 2.90$ μrad with with systematic and statistical errors applied to the quadrature (see Figure 7.10). The uncertainty in this measurement was around 3.5 times greater than that of the red laser beam measurement, which may be due to more intrinsic noise from the blue laser. As there are no calculations involved, only statistical uncertainty has been taken into account. When the ratio of these two ellipticity signals, which were received from the blue and red laser beams, is taken into account, the value obtained is

$$\frac{\epsilon_{blue}}{\epsilon_{red}} = 1.585 \pm 0.004. \tag{7.7}$$

The fact that the observed value can be compared to the theoretical value shows that our methodical study of the Kerr effect gives a good picture of the phenomenon.

66
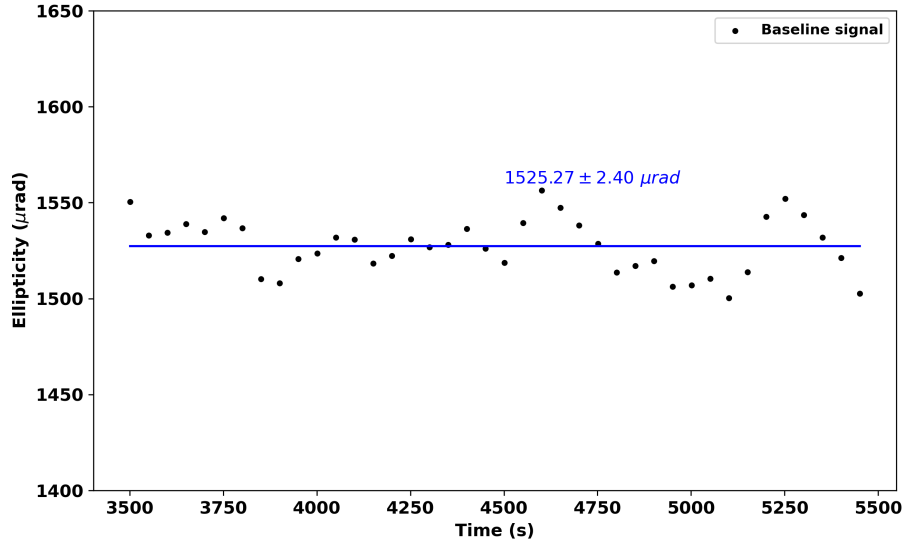
Figure 7.10: Measurement of the baseline ellipticity signal when the blue laser beam of wavelength $\lambda = 404$ nm travels through liquid nitrogen at $V_{AC} = (6871 \pm 10)$ V and $V_{DC} = (14806 \pm 10)$ V voltages.

From both measurements, which took into account red and blue laser beams, it was concluded that the signal-to-noise measurement with a red beam is better than that with a blue beam. Therefore, we used a red beam for the measurement of the binding energy.

7.5 Binding Energy Measurement on Plastic Surface

The binding energy measurement of ions on plastic surfaces in cryogenic liquids is an interesting new approach that has the potential to give insight on the behavior of ions and electrons and the bonding nature of ions in cryogenic systems. Here, the binding energy of ions and electrons on dTPB-coated and uncoated PMMA surfaces was evaluated in liquid nitrogen. As described in section 7.3, the ions are generated by opening the shutter of the cesium source.

7.5.1 Experimental Method

Detailed experimental procedures for measuring ions on plastic surfaces are outlined below, as shown in Figure 7.11.

1. The initial stage involves determining the baseline ellipticity using lower voltages ($V_{eff} \sim 1$ kV - 2 kV), and the resulting lower ellipticity is identified as the "baseline signal" indicated by the first blue line (1) in the ϵ vs. t curve of Figure 7.11.

67

2. In the next step, the ellipticity is measured using a higher HV ($V_{eff} \sim 11$ kV), resulting in an increase in ellipticity. The red horizontal line in Figure 7.11's ϵ vs. t curve (2) represents this maximum voltage signal that can be tuned into the system. However, it should be noted that, beyond this voltage, sparking was observed.

3. In the subsequent stage, to charge the cell, the shutter of the cesium source is kept open for approximately one hour with the same high HV. This initiates the ionization of liquid nitrogen (LN2), resulting in the generation of nitrogen ions and electrons. This step is taken because an increase in the electric field results in an increase in the ionization current, which measures the probability of charges escaping from recombination [56]. In the model of Onsager [74], the ionization current is the probability of charges breaking apart and moving away from each other rather than recombining and canceling each other out. This process helps to improve the cell charging efficiency in our system and increase collection efficiency. The positive nitrogen ions migrate to the negative electrode and adhere to the PMMA cell wall, while the electrons move to the positive side of the electrode. As the ions adsorb on the PMMA surfaces, the signal gradually weakens due to the opposing electric field, as evidenced by the linearly decreasing black line (3) in Figure 7.11's ϵ vs. t curve.

4. The next step is to close the shutter on the cesium source and apply the same low HV as in the first step. Because of the presence of charge particles, when the cesium source is shut off and the same low HV is applied, the obtained signal is lower than the baseline signal. This is represented by the blue line (4) after charging, which is below the dotted baseline signal as shown in Figure 7.11.

5. The final step involves reversing the low HV, which can result in two possible scenarios.

   a) The low HV reversal is insufficient to recombine the ions and electrons. At this condition, the ions were still present, adsorbed on the PMMA surface. When the low HV reversal is insufficient to remove ions from the PMMA surface, the ellipticity signal will be above the baseline signal, which is denoted by the purple line (5a) in Figure 7.11.

   b) If the reversing low HV is strong enough to recombine ions and electrons, they will combine and neutralize each other, resulting in a signal that is aligned with the baseline ellipticity signal. This signal is represented by the cyan-colored line (5b) in Figure 7.11's ϵ vs. t curve.

To find the binding energy electric field, we first found the electric field at which ions or electrons are not removed from the PMMA surface. Then, by measuring the ellipticity signal, we slowly increased the electric field in separate runs until the signal was on the same line as the baseline ellipticity signal.
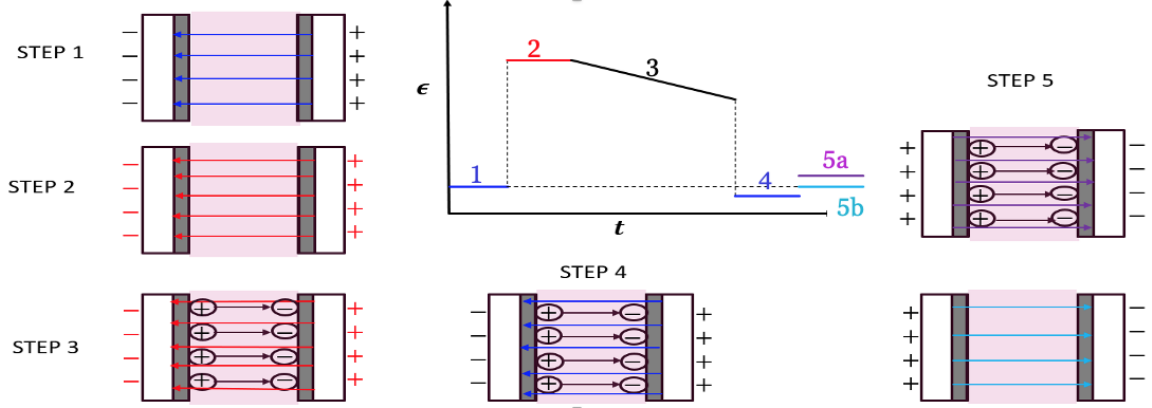
Figure 7.11: Experimental steps for the measurement of the binding energy of ions from PMMA surface.

7.5.2 Binding Energy Measurement of Ions or electrons on a dTPB Coated PMMA Cell

The experimental method explained in Section 7.5.1 was employed to measure the binding energy of ions or electrons on dTPB-coated PMMA in liquid nitrogen. This coated configuration was chosen because it is the one that nEDM@SNS plans to utilize. Prior to the measurement, a selection of low voltages was made to ensure that the measured ellipticity was above 10 μrad. When the signal or ellipticity fall below this threshold, longer integration times were necessary, which could result in a decrease in the number of data points. Based on this consideration, the voltage values of $V_{AC} = (967 \pm 10)$ V and $V_{DC} = (1601 \pm 10)$ V were chosen for the first measurement. An integration time constant of 50 s was selected for this measurement using the lock-in amplifiers.

Considering the geometry (d= 2.79 mm, t= 0.63 mm), media (κ_{PMMA}= 1.91, κ_{LN2}= 1.45), and the applied voltages, the effective electric field at the center of the PMMA electrode system was calculated to be 3.32 kV/cm using Equation 7.3. Figure 7.12 display the ellipticity signal measurement at different steps. At this effective electric field, the baseline ellipticity signal was measured to 14.6 $\pm$ 0.5 μrad (denoted by the first blue horizontal line). The signal increases to 957.6$\pm$0.3 μrad (first red line) with the increase in the voltages to $V_{AC} = (6871 \pm 10)$ V and $V_{DC} = (14801 \pm 10)$ V. Following that, the cell was charged for an hour by opening the shutter of the cesium source (linearly decreasing black line). After the cell was charged, the voltages were lowered to their previous values while establishing the baseline ellipticity. However, the ellipticity signal appeared to be lower than the baseline signal, indicating that the charged particles had separated and adsorbed onto the PMMA cell wall. The ellipticity measured was 9.0 $\pm$ 0.7 μrad (second blue line). Reversing the low HV resulted in a measured ellipticity signal of 19.4 $\pm$ 0.5 μrad (purple line), which was higher than the baseline signal. This suggests that the reversing electric field was not strong enough to remove the ions from the PMMA surface. This sample was taken for an effective electric field of 3.32 kV/cm, and a zoomed-in version of the lower
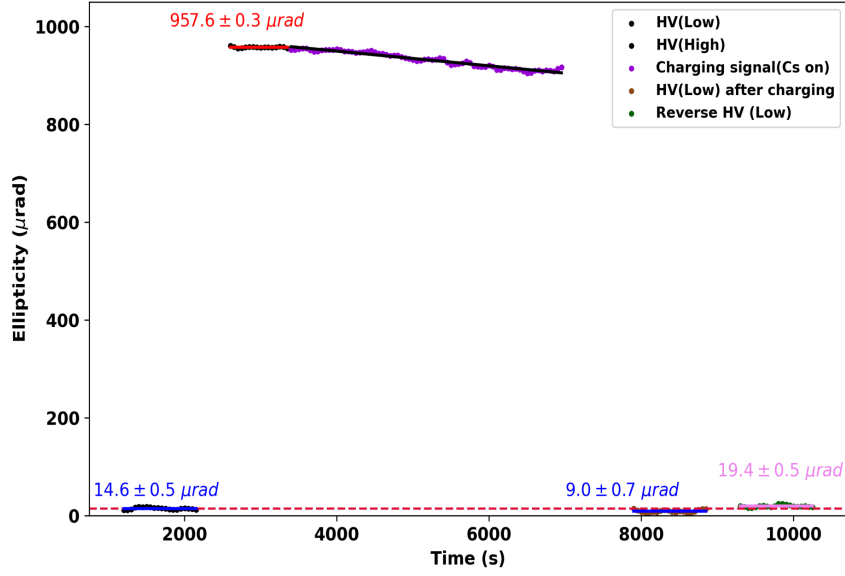
Figure 7.12: Experimental measurement of the binding energy of ions from a dTPB coated PMMA surface for an effective electric field of 3.32 kV/cm.

signals is shown in Figure 7.13.

This is one of several measurements. Multiple measurements were taken in a similar manner to the one previously described. Specifically, the baseline and reverse ellipticity were measured for different effective electric fields. The results of these measurements are presented in Table 7.3. This table presents the values of measured baseline and reverse ellipticity at various effective electric fields. The table also includes the differences between reverse and baseline signals ($\Delta\epsilon = \epsilon_{reverse} - \epsilon_{baseline}$), as well as statistical ($\delta\epsilon_{stat}$), systematic ($\delta\epsilon_{sys}$), and total ($\delta\epsilon_{tot}$) uncertainties

Table 7.3: Measured baseline and reverse ellipticity values at different effective electric fields of dTPB coated PMMA cell.

Ellipticity Measurement with uncertainties						
$E_{eff}(kV/cm)$	$\epsilon_{baseline}$ (μrad)	$\epsilon_{reverse}$ (μrad)	$\Delta\epsilon$ (μrad)	$\delta\epsilon_{stat}$	$\delta\epsilon_{sys}$	$\delta\epsilon_{tot}$
3.32	14.6 ± 0.5	19.4 ± 0.5	4.8	0.7	0.4	0.8
3.55	17.3 ± 1.0	20.7 ± 0.9	3.5	1.3	0.4	1.4
3.80	20.6 ± 0.6	25.0 ± 0.3	4.4	0.7	0.5	0.8
4.05	22.3 ± 0.9	24.5 ± 1.2	2.2	1.5	0.6	1.6
4.31	24.8 ± 0.7	25.5 ± 1.0	0.7	1.2	0.6	1.4
4.74	30.6 ± 1.2	30.9 ± 0.4	0.3	1.3	0.8	1.5
5.22	36.0 ± 0.9	36.9 ± 0.6	0.9	1.1	0.9	1.4

Figure 7.14 depicts the results of the experiment conducted to study the variation

70
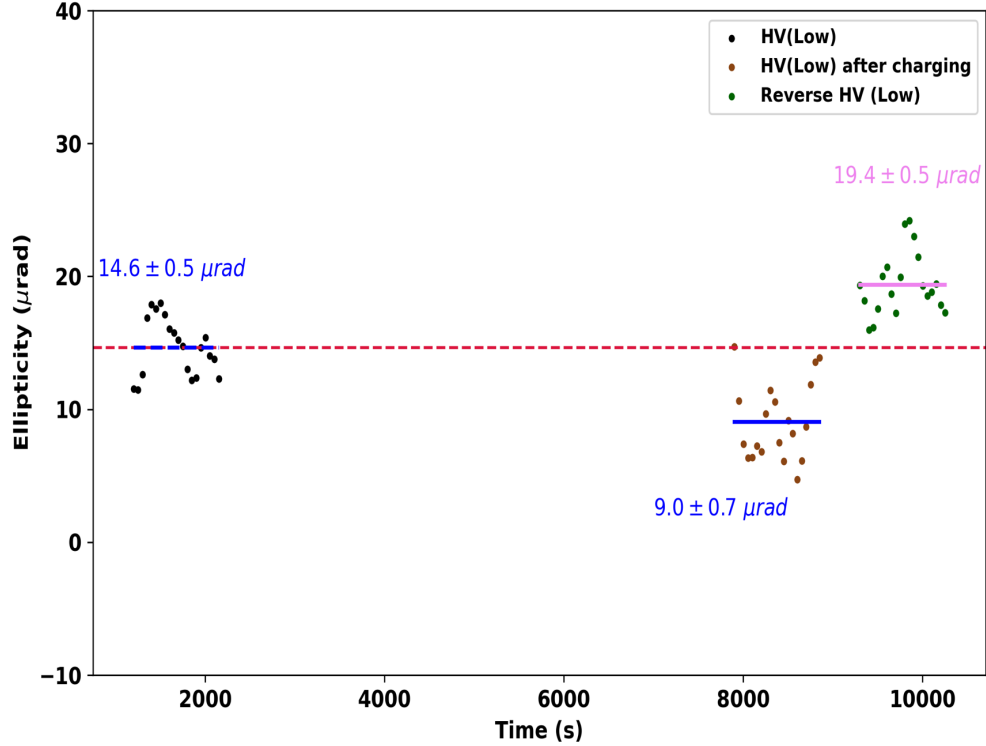
Figure 7.13: Zoomed-in version of the low signal measurement of the signal at an effective electric field of 3.32 kV/cm.

of the difference in reverse and baseline ellipticity measurements with the effective electric field. The horizontal axis of the plot represents the effective electric field in kV/cm, while the vertical axis shows the difference between the reverse and baseline ellipticity measurements in μrad. The measurements were carried out on a dTPB coated PMMA cell in liquid nitrogen, using the experimental method described in Section 7.5. The data consists of multiple measurements at different electric field values, as shown in Table 7.3. The red error bars in the plot represent the measured data points, including both statistical and systematic errors added in quadrature. The statistical error dominates in this measurement and is represented by the black bars. The data points (red) were fitted with a Woods-Saxon function using a non-linear least squares algorithm, and the fitted function is shown as the red curve in the plot. The Woods-Saxon function used was

$$\Delta\epsilon_{fit} = \frac{\Delta\epsilon_0}{1 + e^{\frac{(E_{eff}-E)}{\Delta E}}}. \tag{7.8}$$

The fitted parameters for the variation of the difference in reverse and baseline ellipticity measurements shown in Figure 7.14 are $\Delta\epsilon_0$, E, and ΔE, which represent

Figure 7.14: Electric field dependence of the difference in reverse and baseline ellipticity measurements for a dTPB coated PMMA cell: Statistical and systematic errors added in quadrature (red bars) with Woods-Saxon function fit. Statistical errors are only represented by black bars.

the width of the $\Delta\epsilon$ curve, the electric field at half-width, and the diffuseness, respectively. The values obtained from the plot are 4.58 μrad, 4.07 kV/cm, and 0.11 kV/cm for $\Delta\epsilon_0$, E, and ΔE, respectively. If the data is fitted considering only statistical uncertainty, the corresponding values are 4.62 μrad, 4.07 kV/cm, and 0.11 kV/cm, indicating that the fitting parameters remain almost the same. The effective field at which a transition occurs from a higher ($\Delta\epsilon = \epsilon_{reverse} - \epsilon_{baseline}$) level to the lower level approaching a value of approximately 0 can be used to measure the binding energy of ions or electrons on a PMMA surface in liquid nitrogen. Using the value of E_{eff} at half-width (i.e., 4.07 kV/cm), we can estimate the strength of the interaction between the ions or electrons and the surface. This value is assumed to be a standard value for the removal of ions or electrons from the PMMA surface. This corresponds to a force of 0.04 meV/Å acting on ions or electrons for coated PMMA cells. Based on the Figure 4.4, complete removal of ions from the surface requires a separation distance of 3 Å. If a separation distance of 3 Å is assumed for charged particles, the corresponding binding energy is estimated to be 0.12 meV.

7.5.3 Binding Energy Measurement of Ions or electrons on a Uncoated PMMA Cell

When the dTPB coated PMMA cell is replaced with an identical uncoated PMMA cell, the binding energy measurement can still be performed using the same methodology. Table 7.4 displays the measured values of baseline and reverse ellipticity at different effective electric fields. Additionally, it presents the discrepancies between reverse and baseline signals ($\Delta\epsilon = \epsilon_{reverse} - \epsilon_{baseline}$), and the corresponding statistical ($\delta\epsilon_{stat}$), systematic ($\delta\epsilon_{sys}$), and overall ($\delta\epsilon_{tot}$) uncertainties.
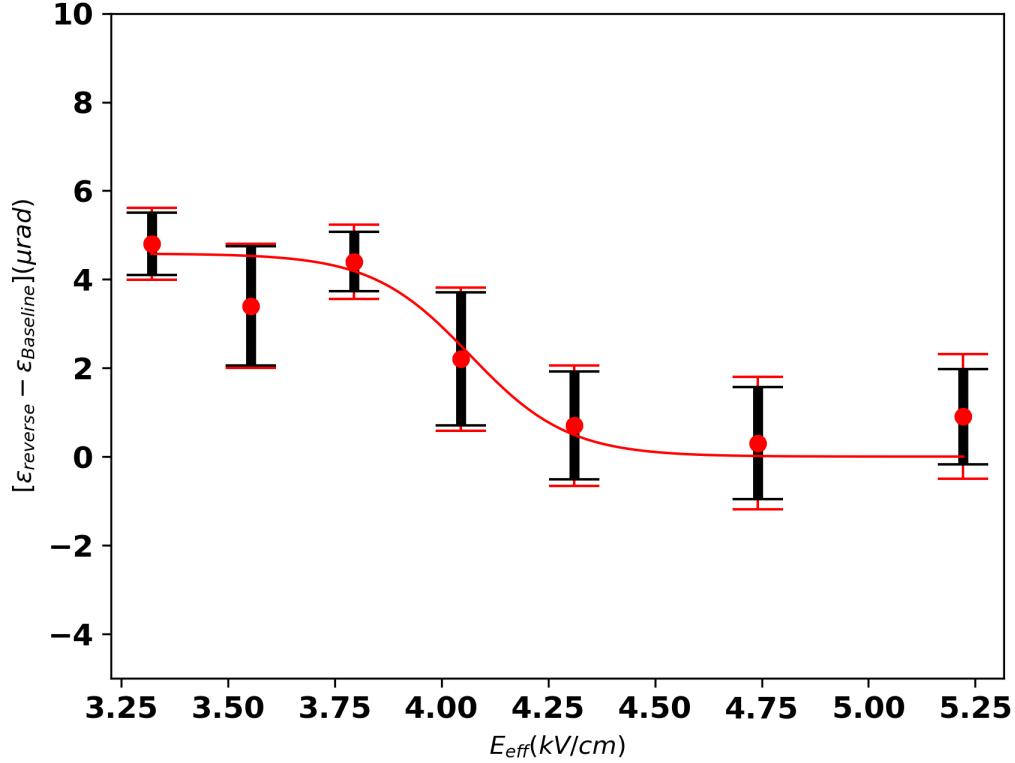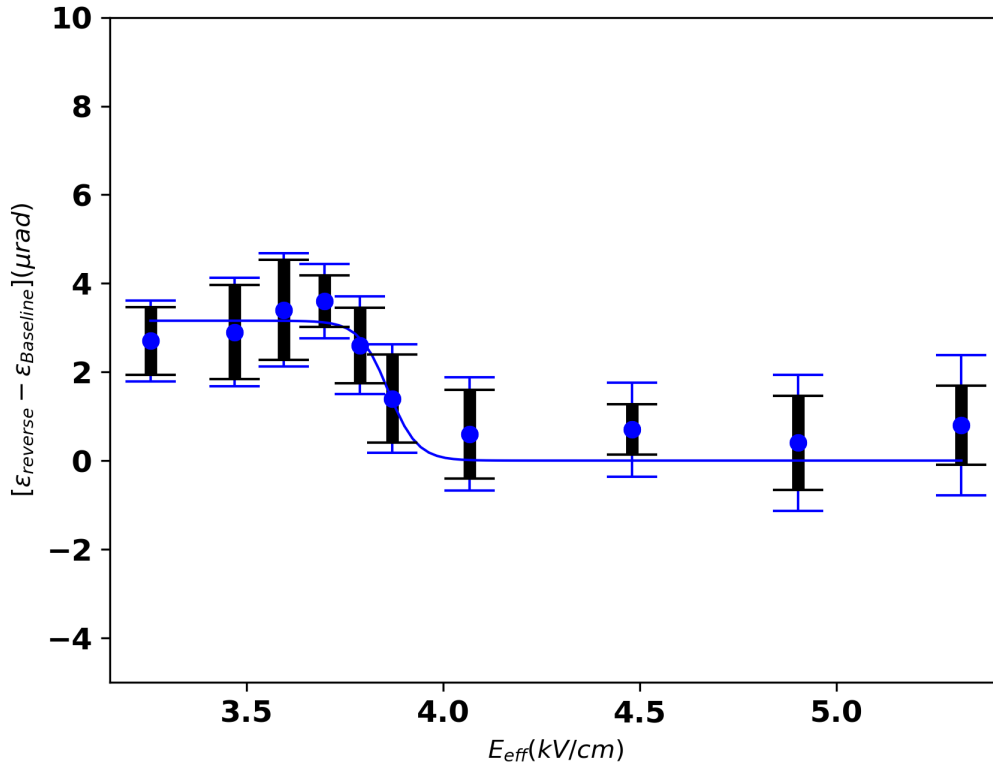

Figure 7.15: Electric field dependence of the difference in reverse and baseline ellipticity measurements for a uncoated PMMA cell: Statistical and systematic errors added in quadrature (blue bars) with Woods-Saxon function fit. Statistical errors are only represented by black bars.

Similarly, the analysis of the change in the difference between the reverse and baseline ellipticity measurements with the effective electric field for uncoated PMMA in liquid nitrogen was conducted, and the results are presented in Figure 7.15. The graph displays the measured data points as blue bars, which include statistical and systematic errors in quadrature, and the fitted curve represented by the blue curve, obtained using the Woods-Saxon function. The black bars represent the statistical

Table 7.4: The values of measured baseline ellipticity and reverse ellipticity with uncertainties for uncoated PMMA at different effective electric fields.

Ellipticity Measurement with uncertainties						
$E_{eff}(kV/cm)$	$\epsilon_{baseline}$ (μrad)	$\epsilon_{reverse}$ (μrad)	$\Delta\epsilon$ (μrad)	$\delta\epsilon_{stat}$	$\delta\epsilon_{sys}$	$\delta\epsilon_{tot}$
3.26	14.6 ± 0.3	17.3 ± 0.7	2.7	0.8	0.5	0.9
3.47	16.3 ± 0.8	19.2 ± 0.7	2.9	1.1	0.6	1.2
3.60	18.6 ± 0.8	22.0 ± 0.8	3.4	1.1	0.6	1.3
3.70	18.2 ± 0.5	21.8 ± 0.3	3.6	0.6	0.6	0.8
3.79	19.7 ± 0.6	22.3 ± 0.6	2.6	0.8	0.7	1.1
3.87	23.6 ± 0.6	25.0 ± 0.8	1.4	1.0	0.7	1.2
4.07	20.9 ± 0.6	21.5 ± 0.8	0.6	1.0	0.8	1.3
4.48	26.6 ± 0.4	27.3 ± 0.4	0.7	0.6	0.9	1.1
4.90	34.7 ± 0.8	35.1 ± 0.7	0.4	1.1	1.1	1.5
5.32	43.0 ± 0.4	43.8 ± 0.8	0.8	0.9	1.3	1.6

uncertainties in the data. The fitted values of $\Delta\epsilon_0$, E, and ΔE from Equation 7.8 are 3.16 μrad, 3.86 kV/cm, and 0.04 kV/cm, respectively. The binding energy of ions or electrons on an uncoated PMMA surface in liquid nitrogen may be calculated using the effective field (E_{eff}) at which the shift from a higher to a lower level takes place. This provide the information about the strength of the interaction between the surface and ions or electrons. Assuming that the electric field at half the width is a standard value for the removal of ions or electrons from the uncoated PMMA surface, the force was found to be 0.039 meV/Å. This value, along with a separation distance of 3 Å for charged particles, led to the estimation of a corresponding binding energy of 0.12 meV. This value is comparable to the binding energy per unit length measured from the dTPB coated PMMA cell.

Figure 7.16 compares the measurements of the dTPB coated and the uncoated PMMA cell walls. Ten measurements were taken for the uncoated sample and seven for the coated sample, both showing similar results. However, differences were observed in the width or height of the ($\Delta\epsilon = \epsilon_{reverse} - \epsilon_{baseline}$) due to small changes in the gap between PMMA plates and electrodes. Careful insertion of PMMA is necessary to account for small changes in gap impact measurements. The drop of the curve from the upper to lower level gives the binding energy measurement, starting at almost the same effective electric field for both coated and uncoated PMMA walls.
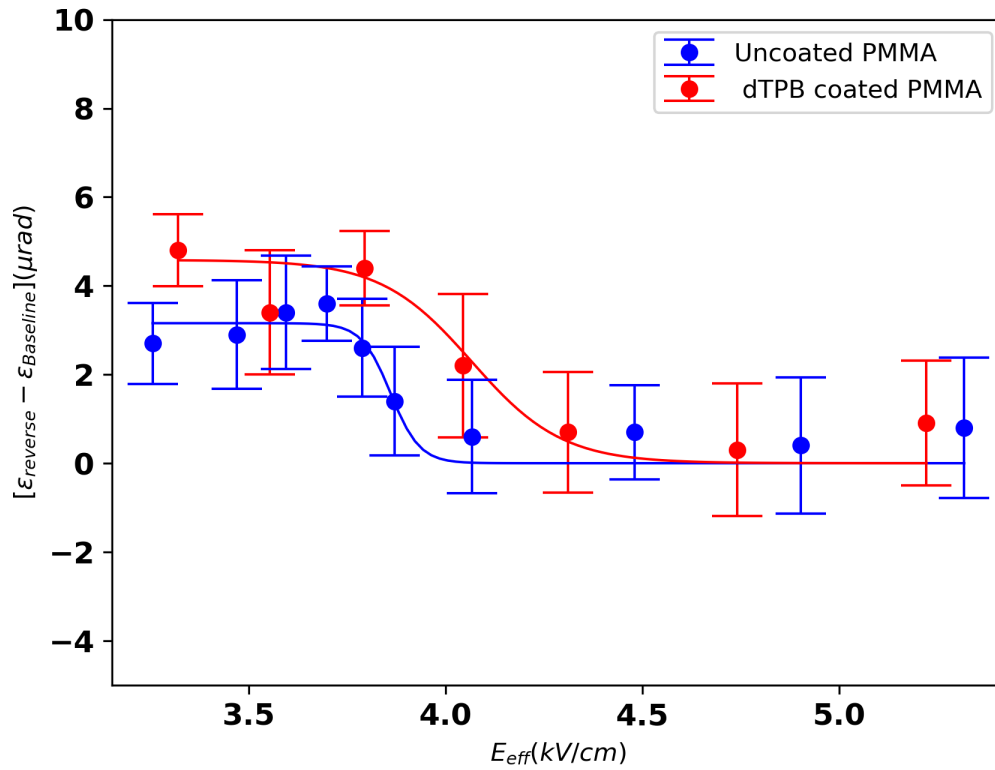
Figure 7.16: Variation of difference in reverse and baseline ellipticity measurements with electric field for dTPB coated and uncoated PMMA cells. The blue curve represents the fitted data for the uncoated PMMA cell, while the red curve represents the fitted data for the coated PMMA cell. Statistical and systematic errors are taken into account with quadrature for both curves.

Chapter 8 Summary and Future Outlook

Possible sources of cell charging in the nEDM@SNS experiment can lead to the separation of charged particles within the cell, resulting in a decrease in the net electric field in the area and the accumulation of charged particles on the PMMA cell walls. These effects may compromise the experiment's predicted sensitivity to a neutron EDM if they cannot be reversed or mitigated. To effectively neutralize the collected charge in the nEDM@SNS experiment, it is important to understand the rate of charge collection, establish a mechanism for neutralization, and determine the frequency at which the charge must be neutralized.

Mark Broering's previous study [7] established a method for removing the generated ions from the measurement regions in the nEDM@SNS experiment. By completely reversing the polarity of the high voltage electrodes, positive ions and electrons recombine and neutralize the ions generated inside the measuring cells. However, the process of reversing the high voltage to 75 kV/cm in the nEDM@SNS experiment using the Cavallo multiplier is time-consuming. In order to reduce the time required for reversing the high voltage in the nEDM@SNS experiment, it is important to understand the binding energy of ions on the PMMA surface (cell wall). This knowledge will allow for the determination of the minimum reversal electric field necessary to recombine all the ions and electrons generated inside the cell. Knowing the binding energy of ions or electrons, it may not be necessary to completely reverse the high voltage to 75 kV/cm. Instead, the ions can be neutralized using lower electric fields.

The primary objective of this study was to investigate the binding energies of ions or electrons on plastic surfaces in liquid nitrogen using the electro-optic Kerr effect. To accomplish this, a novel method was introduced for measuring the binding energy of charges on PMMA surfaces. The method was utilized to measure the binding energy of charged particles on both dTPB coated and uncoated PMMA cells. The minimum value of the reverse effective electric field required for the recombination of nitrogen ions and electrons was found to be approximately 4 kV/cm in a liquid nitrogen. The corresponding force acting on ions or electrons is 0.04 meV/Å, and this value is consistent for both coated and uncoated PMMA cells. If the separation distance between the surface and charged particles is 3 Å (theoretical estimation from the van der Waals plot 4.4), this corresponds to a binding energy of 0.12 meV for the charged particles on the PMMA surface. This experimentally measured value is less than the estimated value assuming van der Waals interactions of ions with the PMMA surface. Although the experiment was successful in determining the minimum reverse electric field required for the recombination of nitrogen ions and electrons in liquid nitrogen, it remains unclear which of the charged particles, either the ions or electrons, were detached first from the surface and where they were subsequently recombined. In order to address these questions, additional experiments and further analysis would be necessary. Additionally, the behavior of ions inside liquid nitrogen is not completely understood, particularly in terms of whether they form snowballs similar to those observed in superfluid helium [75]. The potential impact of snow-

balls on the binding energy of charged particles is also uncertain. If we can obtain a better understanding of these phenomena, it may help to reconcile the discrepancies between our experimental measurements of binding energy and the theoretical predicted values.

Furthermore, the maximum electric field in our system that can be applied is limited to 26.7 kV/cm based on the system discussed earlier. To neutralize ions from the PMMA surface, a reverse electric field is applied, which has a magnitude approximately 6.7 times smaller than the maximum applicable electric field.

The results of the measurement indicate that it might not be essential to fully reverse the electric field to eliminate ions from the PMMA surface. This implies that partial reversal of the electric field could be sufficient to achieve effective ion removal. Although the experiments were conducted in liquid nitrogen, it is likely that the findings could be relevant to liquid helium as well. Thus, we propose repeating the experiment in liquid helium to assess its impact on the nEDM@SNS experiment. However, this would require additional funding. The results of such an experiment would be valuable in understanding the potential applications of ion removal techniques in experimental settings.

At the same time, we also utilized the electro-optic Kerr method and a COMSOL simulation to measure the dielectric constant of PMMA at 70 K. This factor is crucial in determining the magnitude of the electric field within the measuring cell. By utilizing the same method in liquid helium, we may obtain the dielectric constant of the PMMA cell at superfluid helium temperature. By measuring the dielectric constant of the PMMA cell at superfluid liquid helium temperature, the researchers can obtain a more accurate estimate of the electric field in the nEDM@SNS experiment and reduce potential sources of error.

Appendices

Appendix A: How can One Tell Whether a Device is Leaking?

Before filling the LN_2, the vacuum pressures of the inner and outer vacuum chambers (IVC and OVC) are typically around 10^{-3} and 10^{-5} torr, respectively.

The primary fill line should be inserted when N_2 gas has passed through the tank pipe and reached an ambient pressure of 760 torr. Without affecting the OVC pressure, the IVC pressure rises from approximately 10^{-3} torr to 4.2 torr over this time. The IVC pressure stays the same when the primary fill line is inserted, but the OVC pressure starts to drop from around 10^{-5} to about 10^{-6} torr. The OVC pressure stays within the range of $\sim 10^{-6}$ torr if there is no leakage between the IVC and OVC. If there is a leak, the OVC pressure will increase rather than decrease, which is not good. In order to determine the leakage between the OVC and IVC, we must closely monitor the OVC pressure.

Appendix A1: Sealing Techniques for Leakage

Considering that our system constantly cools and warms, as a result, there occasionally appears to be a leak between the inner and outer vacuum chambers. We must carefully disassemble the internal vacuum system and use leak-detecting equipment to test for leaks. Sometimes the leakage is invisible at room temperature. Cold leakage is the term for this kind of leakage. Our system is meant to be submerged in liquid nitrogen while being checked for leaks in order to locate the cold leakage site.

Three areas in our system have the potential to leak:
1) The bottom, where the brass and copper pieces are connected.
2) The window regions (which might seep indium wire or epoxy).
3) The soldering areas.

Indium Wire-based Cryogenic Seals

Using a thin indium wire, a mechanical seal known as a cryogenic seal may be created between two surfaces at very low temperatures. The indium is put between the surfaces, and then they are pressed together to melt the indium and make a seal. When the indium solidifies and cools, it forms a strong bond between the two surfaces, closing the gap.

This kind of seal is often employed in cryogenic applications where a tight barrier is required to stop the escape of cold gases or liquids, such as in refrigeration systems or cryogenic storage containers. Indium is a perfect material for use in these kinds of applications because:
- Cryogenic temperatures don't affect its malleability.

Figure 1: Inner vacuum system.

- It is supple and malleable, it covers blemishes on mating metal surfaces and forms a hermetic seal.

The process of creating a cryogenic seal using indium wire involves cleaning and preparing the surfaces, measuring and cutting the indium wire, placing the wire between the surfaces, pressing the surfaces together, allowing the indium to cool and solidify, and inspecting the seal. It's important to handle the wire with care and to make the seal in a clean environment. The process should be done using a technique to ensure a proper seal.

How can one tell whether a device is leaking?

This type of seal is also used in vacuum applications, such as in vacuum pumps and vacuum vessels, as it can provide a hermetic seal at the molecular level. For sealing, a seal often needs to be built inside a canal or another non-flat, smooth area. Without requiring reflow, Indium will make up for these flaws.

The Window's Epoxy Sealing

Figure 2 depicts the application of epoxy on the window. Leaks may be effectively sealed in low temperature situations with epoxy sealing. Usually a two-part system, the epoxy resin utilized in this procedure is mixed before to application. The epoxy will cure after being applied to a surface and create a solid, long-lasting seal that is impervious to water and other liquids. Even at freezing temperatures, certain epoxy resins that are designed expressly for use in low temperature settings may cure and create a seal.

It is crucial to remember that the surface must be clear of impurities, dry, and clean before applying the epoxy. To establish a tight seal, the leaking region should

Figure 2: Epoxy application on the window.

be located before applying the epoxy over it, covering a little more area than the leak itself. The area should be examined for any leaking indicators once the epoxy has dried, and if required, the procedure may be repeated.

Additionally, it's crucial to utilize the correct product since not all epoxy resins are appropriate for low-temperature settings. To utilize a product with a low enough curing temperature for the desired use, it is advisable to refer to the manufacturer's instructions.

Before applying new epoxy, the old epoxy must be removed. A heat gun is used to warm the epoxy in this process. The window will be slowly pushed out by softened epoxy. Before using new epoxy, all windows with leftover epoxy are supposed to be cleaned up.

To prepare epoxy, Versamid 140 hardener and D.E.R. 383 resin are available. Mix two parts of resin by volume with one component of hardener.

How to put epoxy in the window?

Once the glass and the epoxy-needed area have been cleaned, the glass is gently put over the window with stable and smooth support, and a little wooden spatula is used to spread the epoxy along the glass' edge. Avoiding epoxy's spread is preferable.

Appendix B: Calibration of Photoelastic Modulator (PEM): Bessel Function Zero Methods

One way in which a photoelastic modulator may be calibrated is by using a zero approach for the Bessel function (PEM). This technique finds the PEM's maximum birefringence and zero birefringence point by using the mathematical features of Bessel functions.

For the Bessel function zero approach, one sends a beam of light through a PEM and measures the intensity of the emitted light as a function of the PEM's rotational angle. The period of the sinusoidal intensity pattern in the output light is determined by the birefringence of the PEM. A Bessel function analysis of the intensity distribution reveals the zero-birefringence and maximum-birefringence states of the PEM.

After finding where zero and maximum birefringence occur, the PEM may be fine-tuned to operate within the desired range and with the desired degree of accuracy. In order to ensure that the PEM's output is linear and proportionate to the input, calibration may include monitoring the output at varying degrees of birefringence.

Although the Bessel function zero approach for PEM calibration is a very exact and precise procedure, it does require a high degree of mathematical ability and specific equipment. For reliable results, calibration must be performed by a trained professional, and the equipment must be frequently calibrated and checked for accuracy. At some A_0 value, and therefore, the DC term is constant and unaffected by the birefringence. The value of A_0 must be found here. VDC vs. controller setting graphs were created for several different angular positions of the second polarizer to precisely determine the controller setting for which $J_0 = 0$. When the Bessel function disappears $J_0 = 0$ for a certain controller setting, the graphs should intersect. In our case, we took three angular orientations (30°, 75°, 120°) of PEM for a controller setting from 2 to 3 and measured the first harmonic signal (VDC) through a lock-in amplifier. A typical set of graphs is shown in Figure 3. The measured three lines (blue, green, and purple) at three orientations (30°, 75° , 120°) do not intersect at a single point, but they triangulate in three places at the coordinates (2.77, 85.98), (2.35, 78.94), and (2.45, 75.89). So, the calibration of PEM should be taken into account. To achieve this, the centroid coordinate should be considered, which is (2.52, 80.27). This value of the x-axis, i.e., the retardation angle of 2.52 radians, is set in the controller before performing the experiment.

In conclusion, the Bessel function zero method is a technique that uses the mathematical properties of Bessel functions to find the zero-birefringence position and the maximum birefringence position of a PEM and then calibrate the device so that it operates within the correct range and with the correct degree of precision.

81
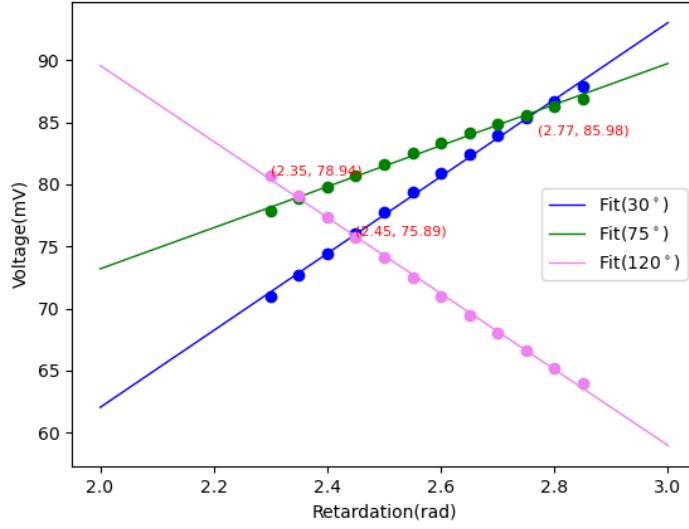
Figure 3: Determining the controller settings for which $J_0 = 0$.

Appendix C: Settings of Lock-In Amplifiers

In this study, four Lock-in amplifiers, each featuring distinct models, have been employed. The specific configuration of each Lock-in amplifier is presented below for clarity and reproducibility.

1. DC Lock-in (Model: 7270 DSP Lock-in amplifier)
   Time constant (TC): 50 s
   Sensitivity (sens): 50 mV
   Input Coupling: DC
   Input shell: float
   Input Connector: A
   Ref Harmonic: 1st
   Output filter slope: 12 dB/OCT
   Ref Source: Ext-fp
   Time constant mode: Fast

2. 1F or PEM Lock-in (Model: 7280 DSP Lock-in amplifier)
   Time constant (TC): 20 μs
   Sensitivity (sens): 50 mV
   Input Coupling: FLT, Fast
   Input Connector: A-B
   Ref Harmonic: 1st
   Output filter slope: 12 dB/OCT

Ref Source: Ext-F

3. MOD1 Lock-in (Model: 7260 DSP Lock-in amplifier)
   Time constant (TC): 50 s
   Sensitivity (sens): 2 mV
   Input coupling: AC
   Input Connector: A-B
   Input shell: float (Bipolar)
   Ref Harmonic: 1st
   Ref source: Ext-Rp
   Output filter slope: 12 dB/OCT

4. MOD2 Lock-in (Model: 7265 DSP Lock-in amplifier)
   Time constant (TC): 50 s
   Sensitivity (sens): 1 mV
   Input coupling: AC
   Input Connector: A-B
   Input shell: float (Bipolar)
   Ref Harmonic: 2nd
   Ref source: Ext-Rp
   Output filter slope: 12 dB/OCT

Setting of Function Generator of HV system

For maximum voltages setup:

For the negative electrode circuit layout (HV$_-$)

- Frequency: 400 mHz

- Offset: 1.7 V$_{dc}$

- Amplitude: 3 V$_{pp}$

For the positive electrode circuit layout (HV$_+$)

- Spellman front panel setup: 7 kV

Bibliography

[1] T. Ito, "Estimated rate of charge accumulation in the nedm measurement cells," *nEDM@SNS collaboration document*, 2011.

[2] S. Chesnevskaya, "Investigation of electric fields, losses and depolarization of ultra-cold neutrons for the new nEDM experiment at FRM II," Ph.D. dissertation, Technische Universität München, 2015.

[3] V. Martin, "Symmetries in particle physics - school of physics and astronomy," https://www2.ph.ed.ac.uk/~vjm/Lectures/SHParticlePhysics2012_files/PPNotes4.pdf, 2012.

[4] C.-S. Wu, E. Ambler, R. W. Hayward, D. D. Hoppes, and R. P. Hudson, "Experimental test of parity conservation in beta decay," *Physical Review*, vol. 105, no. 4, p. 1413, 1957.

[5] W. Korsch, "Searches for the electric dipole moment of the neutron: An experimental overview," https://indico.desy.de/event/8648/contributions/87087/attachments/58305/70804/PANIC14_korsch.pdf, 2014.

[6] S. Lamoreaux and R. Golub, "Experimental searches for the neutron electric dipole moment," *Journal of Physics G: Nuclear and Particle Physics*, vol. 36, no. 10, p. 104002, 2009.

[7] M. Broering, "Study of cell charging effects for the neutron electric dipole moment experiment at oak ridge national laboratory," Ph.D. dissertation, University of Kentucky, 2020.

[8] R. W. Boyd, *Nonlinear optics*, 3rd ed. Academic Press, 2020.

[9] R. Reifenberger, "Simple models for molecule–molecule interactions," https://nanohub.org/groups/u/File:AFM_Chapter_336.pdf, 2016.

[10] G. Krnjaic, "Can the Baryon Asymmetry Arise From Initial Conditions?" *Phys. Rev. D*, vol. 96, no. 3, p. 035041, 2017.

[11] A. Friedman, "On the Curvature of space," *Z. Phys.*, vol. 10, pp. 377–386, 1922.

[12] G. Lemaitre, "A Homogeneous Universe of Constant Mass and Growing Radius Accounting for the Radial Velocity of Extragalactic Nebulae," *Annales Soc. Sci. Bruxelles A*, vol. 47, pp. 49–59, 1927.

[13] E. Hubble, "A relation between distance and radial velocity among extra-galactic nebulae," *Proceedings of the national academy of sciences*, vol. 15, no. 3, pp. 168–173, 1929.

[14] A. A. Penzias and R. W. Wilson, "A measurement of excess antenna temperature at 4080 mc/s." *The Astrophysical Journal*, vol. 142, pp. 419–421, 1965.

[15] R. H. Dicke, P. J. E. Peebles, P. G. Roll, and D. T. Wilkinson, "Cosmic black-body radiation." *The Astrophysical Journal*, vol. 142, pp. 414–419, 1965.

[16] G. Steigman and R. J. Scherrer, "Is the universal matter-antimatter asymmetry fine-tuned?" *Fine-Tuning in the Physical Universe*, p. 174, 2020.

[17] U. Seljak, A. Makarov, P. McDonald, S. F. Anderson, N. A. Bahcall, J. Brinkmann, S. Burles, R. Cen, M. Doi, J. E. Gunn *et al.*, "Cosmological parameter analysis including sdss ly α forest and galaxy bias: constraints on the primordial spectrum of fluctuations, neutrino mass, and dark energy," *Physical Review D*, vol. 71, no. 10, p. 103515, 2005.

[18] E. Komatsu, J. Dunkley, M. Nolta, C. Bennett, B. Gold, G. Hinshaw, N. Jarosik, D. Larson, M. Limon, L. Page *et al.*, "Five-year wilkinson microwave anisotropy probe* observations: cosmological interpretation," *The Astrophysical Journal Supplement Series*, vol. 180, no. 2, p. 330, 2009.

[19] K. Abe, R. Abe, I. Adachi, B. S. Ahn, H. Aihara, M. Akatsu, G. Alimonti, K. Asai, M. Asai, Y. Asano *et al.*, "Observation of large CP violation in the neutral B meson system," *Physical review letters*, vol. 87, no. 9, p. 091802, 2001.

[20] A. Sakharov, Y. Zeldovich, O. LB, and M. Markov, "Sakharov 1967," *Pisma Zh. Eksp. Teor. Fiz*, vol. 5, p. 32, 1967.

[21] G. Servant, "Electroweak baryogenesis," https://cerncourier.com/wp-content/uploads/2022/07/CERNCourier2022JulAug-digitaledition.pdf, pp. 51–52, 2022.

[22] A. Shindler, "Flavor-diagonal CP violation: the electric dipole moment," *The European Physical Journal A*, vol. 57, no. 4, p. 128, 2021.

[23] W. Chao, "First order electroweak phase transition triggered by the higgs portal vector dark matter," *Physical Review D*, vol. 92, no. 1, p. 015025, 2015.

[24] G. R. Farrar and M. Shaposhnikov, "Baryon asymmetry of the universe in the standard model," *Physical Review D*, vol. 50, no. 2, p. 774, 1994.

[25] C. Abel, S. Afach, N. J. Ayres, C. A. Baker, G. Ban, G. Bison, K. Bodek, V. Bondar, M. Burghoff, E. Chanel *et al.*, "Measurement of the permanent electric dipole moment of the neutron," *Physical Review Letters*, vol. 124, no. 8, p. 081803, 2020.

[26] J. Pendlebury and E. Hinds, "Particle electric dipole moments," *Nuclear Instruments and Methods in Physics Research Section A: Accelerators, Spectrometers, Detectors and Associated Equipment*, vol. 440, no. 3, pp. 471–478, 2000.

[27] S. Balashov, K. Green, M. van der Grinten, P. Harris, H. Kraus, J. Pendlebury, D. Shiers, M. Tucker, and D. Wark, "A proposal for a cryogenic experiment to measure the neutron electric dipole moment (nedm)," *arXiv preprint arXiv:0709.2428*, 2007.

[28] M. Ahmed, R. Alarcon, A. Aleksandrova, S. Baeßler, L. Barron-Palos, L. Bartoszek, D. Beck, M. Behzadipour, I. Berkutov, J. Bessuille *et al.*, "A new cryogenic apparatus to search for the neutron electric dipole moment," *Journal of Instrumentation*, vol. 14, no. 11, p. P11017, 2019.

[29] R. Golub and S. K. Lamoreaux, "Neutron electric-dipole moment, ultracold neutrons and polarized 3he," *Physics Reports*, vol. 237, no. 1, pp. 1–62, 1994.

[30] E. Purcell and N. Ramsey, "On the possibility of electric dipole moments for elementary particles and nuclei," *Physical Review*, vol. 78, no. 6, p. 807, 1950.

[31] T.-D. Lee and C.-N. Yang, "Question of parity conservation in weak interactions," *Physical Review*, vol. 104, no. 1, p. 254, 1956.

[32] C. S. Wu, E. Ambler, R. W. Hayward, D. D. Hoppes, and R. P. Hudson, "Experimental test of parity conservation in beta decay," *Physical Review*, vol. 105, pp. 1413–1415, Feb 1957.

[33] J. W. Cronin, "CP Symmetry Violation: The Search for Its Origin," *Rev. Mod. Phys.*, vol. 53, p. 373, 1981.

[34] R. Aaij *et al.*, "Observation of CP Violation in Charm Decays," *Phys. Rev. Lett.*, vol. 122, no. 21, p. 211803, 2019.

[35] J. H. Christenson, J. W. Cronin, V. L. Fitch, and R. Turlay, "Evidence for the 2π Decay of the K_2^0 Meson," *Phys. Rev. Lett.*, vol. 13, pp. 138–140, 1964.

[36] W.-M. Yao *et al.*, "Review of particle physics," *Journal of Physics G: Nuclear and Particle Physics*, vol. 33, no. 1, p. 1, 2006.

[37] M. Kobayashi and T. Maskawa, "CP Violation in the Renormalizable Theory of Weak Interaction," *Prog. Theor. Phys.*, vol. 49, pp. 652–657, 1973.

[38] V. Baluni, "CP-nonconserving effects in quantum chromodynamics," *Physical Review D*, vol. 19, no. 7, p. 2227, 1979.

[39] H.-Y. Cheng, "The strong CP problem revisited," *Physics Reports*, vol. 158, no. 1, pp. 1–89, 1988.

[40] R. Crewther, P. Di Vecchia, G. Veneziano, and E. Witten, "Chiral estimate of the electric dipole moment of the neutron in quantum chromodynamics," *Physics Letters B*, vol. 88, no. 1-2, pp. 123–127, 1979.

[41] M. Pospelov and A. Ritz, "Theta-induced electric dipole moment of the neutron via qcd sum rules," *Physical review letters*, vol. 83, no. 13, p. 2526, 1999.

[42] nEDM Collaboration, "Conceptual design report for the neutron electric dipole moment project (nedm)," *Prepared for the US Dept. of Energy Office of Nuclear Physics*, 2007.

[43] R. Golub, D. Richardson, and S. K. Lamoreaux, *Ultra-cold neutrons.* CRC Press, 2017.

[44] R. Golub and J. Pendlebury, "The interaction of Ultra-Cold Neutrons (UCN) with liquid helium and a superthermal UCN source," *Physics Letters A*, vol. 62, no. 5, pp. 337–339, 1977.

[45] R. Golub, D. Richardson, and S. Lamoreaux, "Ultracold neutrons," *Adam Hilger, Bristol*, 1991.

[46] J. Gerhold, "Dielectric breakdown of helium at low temperatures," *Cryogenics*, vol. 12, no. 5, pp. 370–376, 1972.

[47] W. Burton and B. Powell, "Fluorescence of tetraphenyl-butadiene in the vacuum ultraviolet," *Applied Optics*, vol. 12, no. 1, pp. 87–89, 1973.

[48] nEDM Collaboration, "A new search for the neutron electric dipole moment: Funding pre-proposal," *The Department of Energy*, 2002.

[49] Q. Ye, "Helium-3 relaxation time measurements at low temperatures for the neutron electric dipole moment (nEDM) experiment," Ph.D. dissertation, Duke University, 2008.

[50] L. Schiff, "Measurability of nuclear electric dipole moments," *Physical Review*, vol. 132, no. 5, p. 2194, 1963.

[51] C. Baker, D. Doyle, P. Geltenbort, K. Green, M. Van der Grinten, P. Harris, P. Iaydjiev, S. Ivanov, D. May, J. Pendlebury *et al.*, "Improved experimental limit on the electric dipole moment of the neutron," *Physical Review Letters*, vol. 97, no. 13, p. 131801, 2006.

[52] P. Harris, C. Baker, K. Green, P. Iaydjiev, S. Ivanov, D. May, J. Pendlebury, D. Shiers, K. Smith, M. Van der Grinten *et al.*, "New experimental limit on the electric dipole moment of the neutron," *Physical review letters*, vol. 82, no. 5, p. 904, 1999.

[53] S. K. Imam and nEDM@SNS Collaboration, "Measurement of neutron polarization and transmission for the nEDM@SNS experiment," in *18th International Workshop on Polarized Sources*, 2019.

[54] K. Leung, M. Ahmed, R. Alarcon, A. Aleksandrova, S. Baeßler, L. Barrón-Palos, L. Bartoszek, D. Beck, M. Behzadipour, J. Bessuille *et al.*, "The neutron electric dipole moment experiment at the spallation neutron source," in *EPJ Web of Conferences*, vol. 219. EDP Sciences, 2019, p. 02005.

[55] M. Behzadipour, "Studies of time variations of the magnetic field in the nedm@ sns experiment," Ph.D. dissertation, University of Kentucky, 2022.

[56] G. Seidel, T. Ito, A. Ghosh, and B. Sethumadhavan, "Charge distribution about an ionizing electron track in liquid helium," *Physical Review C*, vol. 89, no. 2, p. 025808, 2014.

[57] S. M. Clayton, T. M. Ito, J. C. Ramsey, W. Wei, M. A. Blatnik, B. W. Filippone, and G. M. Seidel, "Cavallo's multiplier for in situ generation of high voltage," *Journal of Instrumentation*, vol. 13, no. 05, p. P05017, 2018.

[58] S. Clayton, "Hvgeneration,squid applications in sns nedm," https://meetings.triumf.ca/event/10/contributions/140/attachments/96/102/clayton_cavallo_and_squids_final.pdf, 2017.

[59] D. H. Goldstein, *Polarized light.* CRC press, 2017.

[60] M. Born and E. Wolf, *Principles of optics: electromagnetic theory of propagation, interference and diffraction of light.* Elsevier, 2013.

[61] W. Korsch, M. Broering, A. Timsina *et al.*, "Electric charging effects on insulating surfaces in cryogenic liquids," *In preparation*, 2023.

[62] J. N. Israelachvili, *Intermolecular and surface forces.* Academic press, 2011.

[63] K. Najafian, Z. Meir, M. Sinhal, and S. Willitsch, "Identification of molecular quantum states using phase-sensitive forces," *Nature communications*, vol. 11, no. 1, p. 4470, 2020.

[64] A. Hazim, H. M. Abduljalil, and A. Hashim, "Analysis of Structural and Electronic Properties of Novel (PMMA/Al_2O_3, PMMA/Al_2O_3-Ag, PMMA/ZrO_2, PMMA/ZrO_2-Ag, PMMA-Ag) Nanocomposites for Low Cost Electronics and Optics Applications," *Transactions on Electrical and Electronic Materials*, vol. 21, pp. 48 – 67, 2019.

[65] O. Dutuit, N. Carrasco, R. Thissen, V. Vuitton, C. Alcaraz, P. Pernot, N. Balucani, P. Casavecchia, A. Canosa, S. Le Picard *et al.*, "Critical review of N, N^+, N_2^+, N^{++}, and N_2^{++} main production processes and reactions of relevance to Titan's atmosphere," *The Astrophysical Journal Supplement Series*, vol. 204, no. 2, p. 20, 2013.

[66] G. Phelps, "Magneto-optical effects and precision measurement physics: accessing the magnetic Faraday effect of polarized ^{3}He with a triple modulation technique," Ph.D. dissertation, University of Kentucky, 2014.

[67] G. Phelps, J. Abney, M. Broering, and W. Korsch, "A sensitive Faraday rotation setup using triple modulation," *Review of Scientific Instruments*, vol. 86, no. 7, p. 073107, 2015.

[68] X. Zhang, "Kerr electro-optic measurements in liquid dielectrics," Ph.D. dissertation, Massachusetts Institute of Technology, 2014.

[69] LTspice, "Analog Devices, LTspiceIV," https://www.analog.com/en/design-center/design-tools-and-calculators/ltspice-simulator.html.

[70] A. Sushkov, E. Williams, V. Yashchuk, D. Budker, and S. Lamoreaux, "Kerr effect in liquid helium at temperatures below the superfluid transition," *Physical review letters*, vol. 93, no. 15, p. 153003, 2004.

[71] Z. Mousavi, M. M. Ara, and B. Ghafary, "Effect of time and frequency on the electro-optical Kerr constant of olive oil blended with natural turmeric dye," *Optical Materials*, vol. 100, p. 109609, 2020.

[72] S. Stanislaus, "Temperature Dependence of the Dielectric Constant of PMMA," *nEDM@SNS collaboration document*, 2018.

[73] Passive-Components, "Dielectric constant values of several plastics," https://passive-components.eu/what-is-dielectric-constant-of-plastic-materials/.

[74] L. Onsager, "Initial recombination of ions," *Physical Review*, vol. 54, no. 8, p. 554, 1938.

[75] K. Atkins, "Ions in liquid helium," *Physical Review*, vol. 116, no. 6, p. 1339, 1959.

Vita

<div align="center">

Ashok Timsina

</div>

Place of Birth:

- Morang, Nepal

Education:

- University of Kentucky, Lexington, KY
  M.S. in Physics, May. 2020

- The University of Alabama, Tuscaloosa, AL
  M.S. in Physics, Jul. 2018

- Tribhuvan University, Kirtipur, Nepal
  M.Sc. in Physics, Jan. 2012

- Tribhuvan University, Kathmandu, Nepal
  B.Sc. in Physics (Minor: Statistics, Mathematics) Jul. 2008

Professional Positions:

- Graduate Research Assistant, University of Kentucky Spring 2020–Present

- Graduate Teaching Assistant, University of Kentucky Fall 2018–Spring 2020

- Graduate Teaching Assistant, University of Kentucky Spring 2016–Fall 2018

Honors

- Graduate Student Congress (GSC) Research Award, University of Kentucky (Nov. 2022)

- Huffaker Travel Scholarship, Department of Physics and Astronomy, University of Kentucky (Jul. 2022)

- Huffaker Travel Scholarship, Department of Physics and Astronomy, University of Kentucky (Apr. 2022)

- Max Steckler Fellowship, Graduate School Fellowship, University of Kentucky (Aug. 2019)

- Merit-based Scholarship, Central Department of Physics, Tribhuvan University (Aug. 2009)

Publications & Preprints:

- Wolfgang Korsch, Mark Broering, Ashok Timsina, et al., Electric Charging Effects on Insulating Surfaces in Cryogenic Liquids (In preparation).

- Ashok Timsina, Wolfgang Korsch, et al., Measurements of the Binding Energies of Ions on Plastic Surfaces in Liquid Nitrogen (In preparation).